030601-13-T

Simulation of Conformal Spiral Slot Antennas on Composite Platforms

Grant No. NAG 1-1478
Final Report

January 1998

30601-13-T = RL-2432

Grant Title:	Simulation of Conformal Spiral Slot Antennas on Composite Platforms
Primary University Collaborator:	John L. Volakis
Primary NASA-Langley Collaborator:	Fred Beck NASA-Langley Research Center M/S 490 Hampton, VA 23681 (804) 864-1829
Grant Number:	NAG 1-1478
Start Date:	January 1993
End Date:	December 31, 1997
University Address:	Radiation Laboratory Department of Electrical Engineering and Computer Science Ann Arbor, MI 48109-2122 (313) 764-0500
Date:	January 1998
Report Contributors:	J.L. Volakis, M.W. Nurnberger, T. Ozdemir

TABLE OF CONTENTS

Forward

This grant began in January 1993 and ended December 31, 1997. The goals of the grant were to develop analysis and design techniques for conformal broadband slot or printed antennas mounted on doubly curved surfaces.

The uniqueness of the project can be summarized as follows:

- a first implementation of conformal antennas on doubly curved platforms (cylindrical, spherical or any other non-planar configuration).
- development of suitable finite element formulation which combined various elements and domain decompositions for treating the fine details of printed broadband antennas such as spirals and log periodics.
- investigation of efficient mesh truncation schemes for enclosing the finite element domain. New absorbers and boundary integral enclosures with fast integral algorithms were examined
- the ultimate design, fabrication and testing of a broadband conformal antenna which covers all mobile communication needs from 800 MHz up to 3 GHz.

Summary of accomplishments

During the course of the grant, we wrote and distributed about 12 reports and an equal number of journal papers supported fully or in part by this grant. The list of reports (title & abstract) and papers are given in Appendices A and B.

This grant has indeed been instrumental in developing a robust hybrid finite element method for the analysis of complex broadband antennas on doubly curved platforms. Previous to the grant, our capability was limited to simple printed patch antennas on mostly planar platforms. More specifically,

- mixed element formulations were developed and new edge-based prisms were introduced.
- these elements were important in permitting flexibility in geometry gridding for most antennas of interest.
- new perfectly matched absorbers were introduced for mesh truncations associated with highly curved surfaces.
- fast integral algorithms were introduced for boundary integral truncations reducing CPU time from $O(N^2)$ down to $O(N^{1.5})$ or less
- frequency extrapolation schemes were developed for efficient broadband performance evaluations. This activity has been successfully continued by NASA researchers
- computer codes were developed and extensively tested for several broadband configurations. These include FEMA-CYL, FEMA-PRISM and FEMA-TETRA written by L. Kempel, T. Ozdemir and J. Gong, respectively.
- a new infinite balun feed was designed nearly constant impedance over the 800-3000 MHz operational band.
- a complete slot spiral antenna was developed, fabricated and tested at NASA Langley. This new design is a culmination of the projects goals and integrates the computational and experimental efforts. this antenna design resulted in a U.S. patent and was revised three times to achieve the desired bandwidth and gain requirements from 800-3000 MHz.

In the following we include;

1. Appendix A: Reports Generated Under this Grant
2. Appendix B: Refereed Journal Papers Supported Under this Grant
3. Apprndix C: Abstracts of Reports Generated Under this Grant
4. Summary viewgraphs on the computational capabilities of the developed hybrid FEM incorporating fast algorithms
5. An update on the latest analysis, measurement and performance of the patented slot spiral
6. A review of the hybrid finite element method, much of which was developed under this grant

APPENDIX A
Reports Generated Under This Grant

Report #	Title	Authors
030601-1-T (July 1993)	Radiation and scattering by cavity-backed antennas on a circular cylinder	Leo C. Kempel, John L. Volakis
030601-2-T (September 1993)	Scattering by a groove in an impedance plane	Sunil Bindiganavale, John L. Volakis
030601-3-T (January 1994)	Scattering by cavity-backed antennas on a circular cylinder	Leo C. Kempel, John L. Volakis
030601-4-T (January 1995)	Simulation of thin slot spirals and dual circular patch antennas using the finite element method with mixed elements	J. Gong, J. L. Volakis, M.W. Nurnberger
030601-5-T (July 1995)	Triangular prisms for edge-based vector finite element analysis of conformal antennas	J. Gong, T. Ozdemir, J. L. Volakis
030601-6-T (August 1995)	An new planar feed for slot spiral antennas	M.W. Nurnberger, J. L. Volakis
030601-7-T (January 1996)	Efficient finite element simulation of slot antennas using prismatic elements	J. Gong, J. L. Volakis
030601-8-T (July 1996)	An AWE implementation for electromagnetic FEM analysis	J. Gong, J. L. Volakis
030601-9-T (August 1996)	A planar slot spiral for conformal vehicle applications	M.W. Nurnberger, J. L. Volakis, D. T. Fralick, F. B. Beck
030601-10-T (October 1996)	Robust hybrid finite element methods for antennas and microwave circuits	J. Gong, J. L. Volakis
030601-11-T (August 1997)	Fast memory-saving hybrid algorithms for electromagnetic scattering and radiation	S. S. Bindiganavale, J. L. Volakis
030601-12-T (Janaury 1998)	AWE method in frequency domain electromagnetics	E. Erdemli, C. Reddy, J. Volakis

APPENDIX B
Refereed Journal Papers Supported Under this Grant

1. L.C. Kempel and J.L. Volakis, "Scattering by cavity-backed antennas on a circular cylinder," *IEEE Trans. Antennas Propagat.*, Vol. 42, No. 9, pp. 1268-1279,1994.

2. J.L. Volakis and L. C. Kempel, "Electromagnetics: Computational methods and considerations," *IEEE Computational Science and Engineering Mag.*, Vol. 2, No.1, pp. 42-57, Spring 1995.

3. L.C. Kempel, J.L. Volakis and R. Sliva, "Radiation by cavity-backed antennas on a circular cylinder," *IEE Proceedings-H*, pp. 233-239, 1995.

4. J.L. Volakis and A. Chatterjee, " A selective review of the finite element-ABC and the finite element-boundary integral methods for electromagnetic scattering," (invited paper) *Annales de Telecom.*, Vol. 50, No. 5-6, pp. 499-509, May-June 1995.

5. J. Gong and J.L. Volakis, "An efficient and accurate model of the coax cable feeding structure for FEM simulations," *IEEE Trans. Antennas and Propagat.*, Vol. 43, pp. 1474-1478, Dec. 1995.

6. J.Gong, J.L. Volakis and H.T.G. Wang, "Efficient finite element simulation of slot antennas using prismatic elements," *Radio Sci.* , Vol. 31, No. 6, pp. 1837-1844, Nov-Dec. 1996

7. J.Gong and J.L. Volakis, "An AWE Implementation for Electromagnetic FEM Analysis," *IEE Electronics Letters*, Vol. 32, No.24, pp.2216-2217, 21st November 1996.

8. M. Nurnberger and J.L. Volakis, "A new planar feed for slot spiral antennas," *IEEE Trans. Antennas and Propagat.*, Vol. 44, pp. 130-131, Jan. 1996.

9. S. Bindiganavale and J. L. Volakis, "Scattering by narrow gaps in an impedance plane,"*Radio Sci.*., pp. 401-408, March-April 1996.

10. J.L. Volakis, J. Gong and T. Ozdemir, "Applications of the FEM to Conformal Antennas," Ch. 13 in the book *Finite Element Software for Microwave Engineering* ed. by Itoh, Silvester and Pelosi (Wiley, 1996), pp. 313-345

11. T. Ozdemir, M.W. Nurnberger, J.L. Volakis, R. Kipp and J. Berrie, "A hybridization of finite element and high frequency methods for pattern prediction of antennas on aircraft structures," *IEEE Antennas and Propagat. Soc. Mag, Vol. 38, No.3* pp. 28-38, June 1996.

12. J.L. Volakis, T. Ozdemir and J. Gong "Hybrid Finite Element methodologies for antennas and scattering," *IEEE Trans. Antenna Propagat.*, pp. 493-507, March 1997

13. T. Ozdemir and J. L. Volakis, "Triangular Prisms for Edge-Based vector finite elements analysis," *IEEE Trans.Antennas Propagat.*, pp. 788-797, May 1997

14. Z. Li, P. Papalambros, J.L. Volakis, "Designing broadband patch antennas using the sequential quadratic programming method," *IEEE Trans. Antennas and Propagat.*, pp. 1689-1692, Nov. 1997.

15. S. Bindiganavali, J. L. Volakis and H. Anastassiu, "Scattering from plates containing small features using the adaptive integral method(AIM)," submitted to *IEEE Trans. Antennas and Propagat.*

16. S. Bindiganavale and J.L. Volakis,"Radiation and Scattering from Cavity-Backed Slot Antennas Using the Finite Element-Adaptive Integral Method," submitted to *IEEE Trans. Antenna Propagat*

AMTA Papers

1. M. Nurnberger, J. Volakis, D. Fralick and F.B. Beck, " A planar slot spiral for conformal vehicle applications," 1997 American Measurement techniques Assoc.(AMTA) Symposium, Seattle, Digest pp. 121-126.

2. M.W. Nurnberger and J.L. Volakis, "A planar slot spiral for mobile communications," 19th *American Measurement Techniques Assoc.* (AMTA), Symposium Digest pp. , Boston, MA, 1998.

SEVERAL papers were also presented at the following Meetings:

1. Antennas and Propagation Symposia (held annually in North America)
2. Applied Computational Electromagnetics Society
3. International URSI Meetings

APPENDIX C

Abstracts of Reports Generated Under this Grant

Radiation and Scattering by Cavity-backed Antennas on a Circular Cylinder

Leo C. Kempel and John L. Volakis

July 21, 1993

Abstract

Conformal arrays are popular antennas for aircraft and missile platforms due to their inherent low weight and drag properties. However, to date there has been a dearth of rigorous analytical or numerical solutions to aid the designer. In fact, it has been common practice to use limited measurements and planar approximations in designing such non-planar antennas. In this report, we extend the finite element-boundary integral method to scattering and radiation by cavity-backed structures in an infinite,metallic cylinder. In particular, we discuss the formulation specifics such as weight functions, dyadic Green's function, implementation details and particular difficulties inherent to cylindrical structures. Special care is taken to ensure that the resulting computer program has low memory demand and minimal computational requirements. In this report, both scattering and radiation parameters are computed and validated as much as possible.

Scattering by a Groove in an Impedance Plane

Sunil S.Bindiganavale and John L.Volakis

Radiation Laboratory
Department of Electrical Engineering
and Computer Science
The University of Michigan
Ann Arbor, Michigan 48109-2122.

September 24, 1993

Abstract

An analysis of two-dimensional scattering from a narrow groove in an impedance plane is presented. The groove is represented by a impedance surface and hence the problem reduces to that of scattering from an impedance strip in an otherwise uniform impedance plane. On the basis of this model, appropriate integral equations are constructed using a form of the impedance plane Green's functions involving rapidly convergent integrals. The integral equations are solved by introducing a single basis representation of the equivalent current on the narrow impedance insert. Both transverse electric (TE) and transverse magnetic (TM) polarizations are treated. The resulting solution is validated by comparison with results from the standard boundary integral method (BIM) and a high frequency solution. It is found that the presented solution for narrow impedance inserts can be used in conjunction with the high frequency solution for the characterization of impedance inserts of any given width.

Scattering by Cavity-backed Antennas on a Circular Cylinder

Leo C. Kempel and John L. Volakis
Radiation Laboratory
1301 Beal Ave.
Ann Arbor, MI 48109-2122

November 15, 1993

Abstract

Conformal arrays are popular antennas for aircraft, spacecraft and land vehicle platforms due to their inherent low weight and drag properties. However, to date there has been a dearth of rigorous analytical or numerical solutions to aid the designer. In fact, it has been common practice to use limited measurements and planar approximations in designing such non-planar antennas. In this paper, we extend the finite element-boundary integral method to scattering by cavity-backed structures in an infinite, metallic cylinder. In particular, we discuss the formulation specifics such as weight functions, dyadic Green's function, implementation details and particular difficulties inherent to cylindrical structures. Special care is taken to ensure that the resulting computer program has low memory demand and minimal computational requirements. Scattering results are presented and validated as much as possible.

Preface

This semi-annual report describes our progress up to mid-January 1995. The report contains five sections all dealing with the modeling of spiral and patch antennas recessed in metallic platforms. Of significance is the development of decomposition schemes which separate the different regions of the antenna volume. These schemes are used in modeling the spiral and the dual circular patch antennas. In the case of the spiral, a mixed (edge and node) element formulation is developed to avoid use of small elements in modeling the slot. This also allows for use of the simpler wire green's function in modeling the radiated fields. Overall, the resulting modeling approach leads to substantial simplifications and is perhaps the most efficient within the context of hybrid FEM formulations. The implementation of this formulation is nearly complete but we already fabricated and tested an archimedean slot spiral operating at a center frequency of 1.1 GHz (see Section 2 of the report). The main goal of the experiment was to examine the feasibility of a new feed design for the slot spiral antenna. This feed design consisted of a microstrip line below the metallic section of the slot spiral but, unfortunately, our first design trial required improvements to bring the axial ratio close to unity. A new design is currently under fabrication and with the help of the new software, it is our hope that the feed design issue will be resolved over the next two months.

Substantial effort was devoted over the past six months in improving the feed model in the context of the FEM. This is addressed in Sections 3 and 4 where we describe simple, but very successful implementations of the coax probe and slot-coupled microstrip line feed. In the latter case, the feed network is modeled using brick elements whereas the antenna volume is modeled using tetrahedrals. The two computational regions were then coupled by enforcing potential continuity (a new approach) across the slot joining the two regions. A design of a dual stacked circular patch configuration is included which demonstrates the validity of the potential continuity condition. Also, as noted in Section 3, the proposed coax cable model yields input impedance results which overlay the measured data.

Finally, Section 5 of the report presents an innovative scheme for truncating finite element meshes. This is an alternative to the absorbing boundary conditions and employs a perfectly matched anisotropic absorber. It was already tested for terminating transmission lines in microwave circuits and we are in the process of implementing it in our FEM antenna codes.

In the next few months our goal is to complete the spiral antenna code and employ it to examine several spiral antenna configurations operating at different bands, including that from 944-1256 MHz as discussed in the proposal. The code will be also enhanced with several features relating to feed modeling and mesh truncation. Finally, additional fabrications and antenna measurements will be made.

Triangular prisms for edge-based vector finite element analysis of conformal antennas

T. Özdemir and J. L. Volakis

Radiation Laboratory
Department of Electrical Engineering and Computer Science
University of Michigan
Ann Arbor, Michigan 48109-2122

June 5, 1995

Abstract

This paper deals with the derivation and validation of edge-based shape functions for the distorted triangular prism. Although the tetrahedron is often the element of choice for volume tessellation, mesh generation using tetrahedra is cumbersome and CPU intensive. On the other hand, the distorted triangular prism allows for meshes which are unstructured in two dimensions and structured in the third dimension. This leads to substantial simplifications in the meshing algorithm and many printed antenna and microwave circuit geometries can be easily tessellated using such a mesh. The new edge-based shape functions presented in this paper are validated by eigenvalue, radiation and scattering, and input impedance computations involving conformal antennas on planar and cylindrical platforms. Also presented are results showing the effect of platform curvature on resonance behavior of such antennas.

A New Planar Feed for Slot Spiral Antennas

M. W. Nurnberger and J. L. Volakis

Radiation Laboratory
Department of Electrical Engineering
and Computer Science
The University of Michigan
Ann Arbor, MI 48109-2122

Abstract

This report presents a new planar, wideband feed network for a slot spiral antenna, and the subsequent design and performance of a VHF antenna utilizing this feed design. Both input impedance and radiation pattern measurements are presented to demonstrate the performance and usefulness of this feed. Almost all previous designs have utilized wire spirals, requiring bulky, non-planar feeds with separate baluns, and large absorbing cavities. The presented slot spiral antenna feed integrates the balun into the structure of the slot spiral antenna, making the antenna and feed planar. This greatly simplifies the design and construction of the antenna, in addition to providing repeatable accuracy. It also allows the use of a very shallow reflecting cavity for conformal applications. Finally, this feeding approach now makes many of the known miniaturization techniques viable options.

Efficient Finite Element Simulation of Slot Antennas Using Prismatic Elements

Jian Gong and John L. Volakis
radiation laboratory
University of Michigan
Ann Arbor, MI 48109-2122
jxgum@umich.edu volakis@umich.edu

Abstract

A hybrid finite element - boundary integral (FE-BI) simulation technique is discussed to treat narrow slot antennas etched on a planar platform. Specifically, the prismatic elements are used to reduce the redundant sampling rates and ease the mesh generation process. Numerical results for an antenna slot and frequency selective surfaces are presented to demonstrate the validity and capability of the technique.

1 Introduction

It has been reported that a hybrid finite element-boundary integral technique [Jin, et. al. 1991, Silvester and Pelosi (1994)] can be employed for characterizing conformal antennas of arbitrary shape [Gong, et. al. (1994)]. Indeed, planar/non-planar, rectangular/non-rectangular designs, ring slot or spiral slot antennas with probe, coax cable or microstrip line feeds can be simulated with this formulation. This is because of the geometrical adaptability of tetrahedral elements used for the implementation. However, in practice, certain configurations require extremely high sampling rates due to the presence of fine geometrical details. Among them are a variety of slot antennas (spirals, rings, slot spirals, cross slots, log-periodic slots, etc.), where the slot width is much smaller than the other dimensions (cavity diameter or inter-distance of slots). In these cases, the mesh is extremely dense (with over 50, 100 or even higher samples per wavelength), whereas typical discretizations involve only 10-20 elements per wavelength. This

An AWE Implementation for Electromagnetic FEM Analysis

Jian Gong and John L. Volakis
Radiation Laboratory
University of Michigan
Ann Arbor, MI 481098-2122
jxgum@umich.edu volakis@umich.edu

Abstract

Although full wave electromagnetic systems are large and cumbersome to solve, typically only a few parameters, such as input impedance, S parameters, and far field pattern, are needed by the designer or analyst. A reduced order modeling of these parameters is therefore an important consideration in minimizing the CPU requirements. The Asymptotic Waveform Evaluation(AWE) method is one approach to construct a reduced order model of the input impedance or other useful electromagnetic parameters. We demonstrate its application and validity when used in conjunction with the finite element method to simulate full wave electromagnetic problems.

1 Introduction

The method of Asymptotic Waveform Evaluation (AWE) provides a reduced-order model of a linear system and has already been successfully used in VLSI and circuit analysis to approximate the transfer function associated with a given set of ports/variables in circuit networks [1, 2, 3]. The basic idea of the method is to develop an approximate transfer function of a given linear system from a limited set of spectral solutions. Typically, a Padè expansion of the transfer function is postulated whose coefficients are then determined

A PLANAR SLOT SPIRAL FOR CONFORMAL VEHICLE APPLICATIONS

M.W. Nurnberger*, J.L. Volakis*, D.T. Fralick†, F.B. Beck†

* Radiation Laboratory
Dept. of Elect. Engin. & Comp. Sci.
University of Michigan, Ann Arbor, MI 48109-2122
† NASA-Langley Research Center
Hampton, VA 23681

ABSTRACT

A slot spiral antenna and its associated feed are presented for conformal mounting on a variety of land, air, and sea vehicles. The inherent broadband behavior and good pattern coverage of the spiral antenna is exploited for the integration of multiple frequencies, and thus multiple transmitting and receiving apertures, into one compact, planar antenna. The feasibility of the broadband slot spiral antenna relies on the use of an equally broadband, balanced, planar, and non-intrusive feed structure. The design of the slot spiral, its feeding structure, and the reflecting cavity are discussed with emphasis on the experimental validation and construction of the antenna.

Keywords: Spiral Antennas, Planar, Conformal, Automotive,-Antenna Measurements

1.0 INTRODUCTION

Spiral antennas are particularly known for their ability to produce very wide-band, almost perfect circularly-polarized radiation over their full coverage region. Because of this polarization diveristy and broad spatial and frequency coverage, many applications exist, ranging from military surveilance, ECM, and ECCM to numerous commercial and private uses, including the consolidation of multiple low gain communications antennas on moving vehicles.

For the typical wire spiral antenna, the performance advantages mentioned above come at the price of size and complexity. While the radiating elements of a wire spiral may be planar, the feed network and balun structures generally are not, and combine to add weight, depth, and significant

Robust Hybrid Finite Element Methods for Antennas and Microwave Circuits

Introduction

One of the primary goals in this dissertation is concerned with the development of robust hybrid finite element–boundary integral (FE–BI) techniques for modeling and design of conformal antennas of arbitrary shape. Both the finite element and integral equation methods will be first overviewed in this chapter with an emphasis on recently developed hybrid FE–BI methodologies for antennas, microwave and millimeter wave applications. The structure of the dissertation is then outlined. We conclude the chapter with discussions of certain fundamental concepts and methods in electromagnetics, which are important to this study.

ABSTRACT

FAST MEMORY-SAVING HYBRID ALGORITHMS FOR ELECTROMAGNETIC SCATTERING AND RADIATION

The main theme in this dissertation is examination of techniques for alleviating the excessive memory requirement and execution time associated with implementations of popular frequency domain numerical techniques for electromagnetic scattering and radiation. Of particular interest is the reduction of computational complexity associated with integral equation techniques such as the moment method.

In this dissertation, we develop an algorithm for directly generating sparse matrices from the original fully populated moment method interaction matrix and subsequently refining the solution iteratively. However, this technique is still $O(N^2)$ and yields more accurate results for relatively smooth scatterers. We were the first to perform an error analysis of the Fast Multipole Method (FMM) and based on given error criteria, we set guidelines for choosing the various parameters affecting the speed and solution accuracy. Scattering from a realistic size aircraft nose radome and the interactions between a radome and the antenna at its base was computed with a version of the FMM. For the first time, fast integral methods are considered for efficient solution of hybrid finite element boundary integral methods, thus enhancing the attractiveness of these techniques to model large, composite bodies.

The Adaptive Integral Method (AIM) is ideal for modeling bodies with intricate construction and high discretization rates since it translates the original problem grid to a new coarser regular grid, enabling use of Toeplitz matrix techniques for fast matrix-vector product computation. We demonstrate special features that make this technique eminently suitable for planar scatterers and cavity backed-antennas.

AWE Technique in Frequency Domain Electromagnetics

Yunus E. Erdemli*, C.J.Reddy# and John L. Volakis*

Abstract:

This paper presents fast radar cross section (RCS) computations using the Asymptotic Waveform Evaluation (AWE) technique in conjunction with Method of Moments (MoM) and hybrid Finite Element (FEM/MoM) implementations. In its traditional form, AWE constructs a reduced-order model of a given linear system by Taylor series expansion with respect to specific values of the system parameters (frequency, angle, etc.). Thus, AWE permits the prediction of the frequency response from a few frequency calculations. In this paper we modify AWE to instead employ a rational function (Padè approximation) representation for the system parameters. Using a Padè rational function instead of a Taylor series, the accuracy of the analysis is increased to a wider frequency range. AWE is also extended to allow monostatic RCS pattern prediction using again a few pattern values, thus eliminating a need to resolve the system when an iterative solver is employed. To demonstrate these extensions of AWE, numerical examples of three-dimensional metallic bodies and cavity-backed apertures are considered.

* Y. E. Erdemli and J.L. Volakis are with Radiation Laboratory, University of Michigan, Ann Arbor MI, USA.

C. J. Reddy is with Department of Electrical Engineering, Hampton University, Hampton VA 23668, USA.

Hybrid Finite Element Methods for Conformal Antenna Simulations

John L. Volakis
Radiation Laboratory,
Dept. of Electrical Engin. and Computer Science
University of Michigan
1301 Beal Ave.
Ann Arbor, MI. 48109-2122

Phone: 734-764-0500 Fax:-734-647-2106
Email: volakis@umich.edu
HomePage: http://www-personal.engin.umich.edu/~volakis/

Finite Element Method--History

- FEM is a mature method
  - Dates back to Courant (1940)
  - Argyris (1950s) put together essential math for practical implemention in Structural Mechanics
    - Assembly Boundary conditions,
    - Domain Partitioning
  - Dayton Conferences in 1965, 1968, 1970
- Silvester (1969), first applied FEM to waveguide problems
- Alett, Bahrani and Zienkiewicz (1968), applied FEM to solving Helmholtz's Equ.
- Silvester(1971), McDonald & Wexler(1972) introduced FEM-Boundary integral method

FEM Attributes

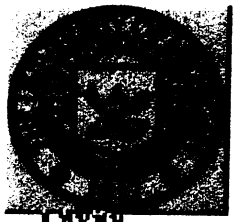

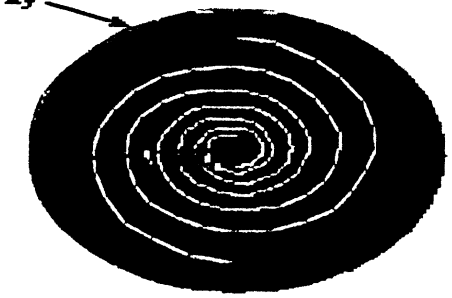

Two-arm slot spiral antenna

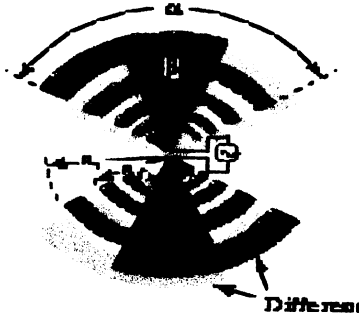

Stacked microstrip log periodic antenna

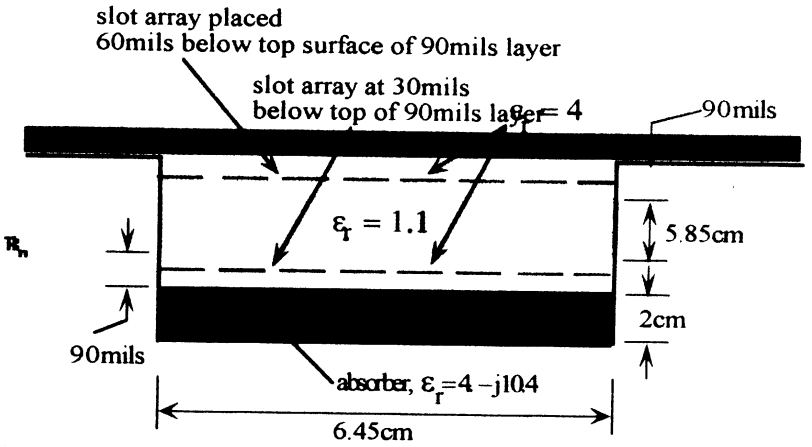

- Established Approach for EM Modeling --O(N) resources
- Geometrical Adaptability (for design and frequency control)
- Material Generality, New Physics Readily Added
- Can Learn from Other Engineering Disciplines and Math literature.
- Many FEM success for Antennas and Circuits
- Accurate Feed Modeling
- Can Avoid Green's Functions

FEM Attributes-Continued

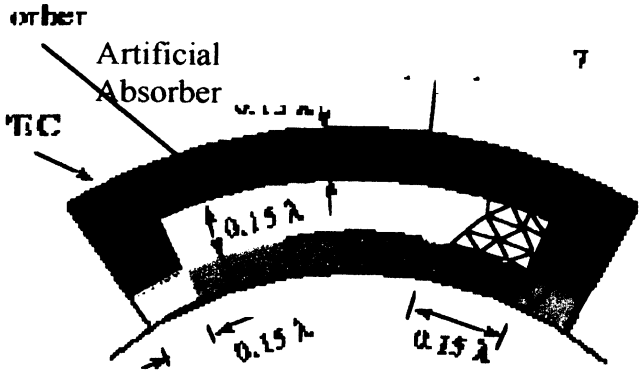

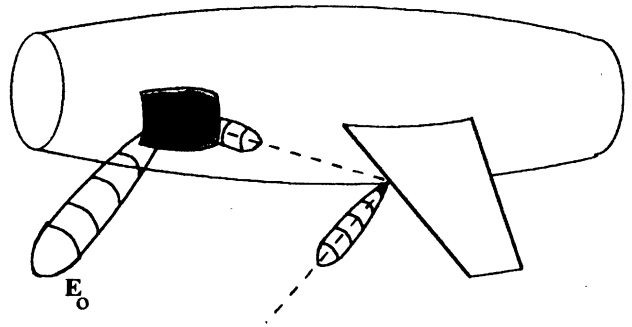

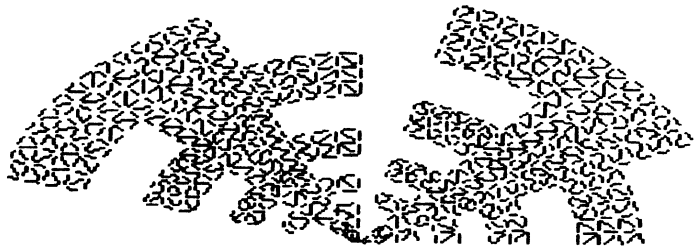

- New Mesh Truncation Schemes Provide Accuracy Control
- Near Field Visualization
- Hybridization with High Frequency Methods for Modeling Far Zone Interactions
- Hybridization with Fast Integral Methods Offers Opportunity for Fast and Rigorous Codes
- Frequency Extrapolation Techniques (AWE, CFH) Promise Even More Speed and Design Agility

Antenna Applications

- Hybrid FEM-BI and FEM-ABC for conformal printed antenna modeling
- Complex Broadband Antenna Elements using FE-BI with fast integral methods
- Antennas on Ferrites
- Design Optimization
- Frequency Selective Surfaces
- Structurally Embedded Conformal Arrays

Artificial Absorber Truncation

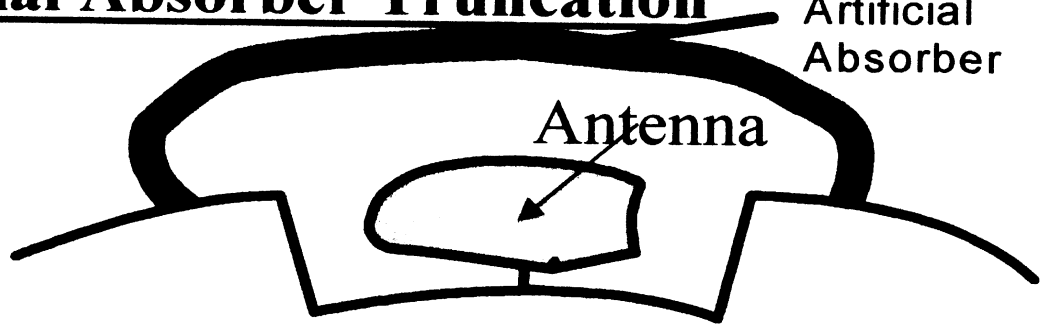

Sparse Matrix

$$[A]\{E\}=\{f^{inc}\}$$

Boundary Integral Truncation

PML Deteriorate
Covergence

Dense

$$\begin{bmatrix} A^{int} & A^{cross} \\ A^{Tcross} & A^{bound} \end{bmatrix}\begin{Bmatrix} E^{int} \\ E^{bound} \end{Bmatrix}+\begin{bmatrix} 0 & 0 \\ 0 & G \end{bmatrix}\begin{Bmatrix} E^{int} \\ E^{bound} \end{Bmatrix}=\begin{Bmatrix} f^{int} \\ f^{ext} \end{Bmatrix}$$

- Number of Unknowns is reduced by a factor of 5 or more
- For Narrow slots BI matrix is small
- FFT can be used to speed-up computation of matrix vector products

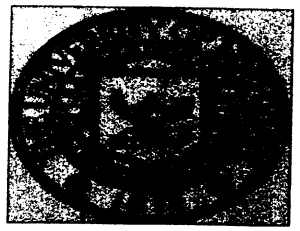

PRISM FOR ANTENNA ON CURVED PLATFORM

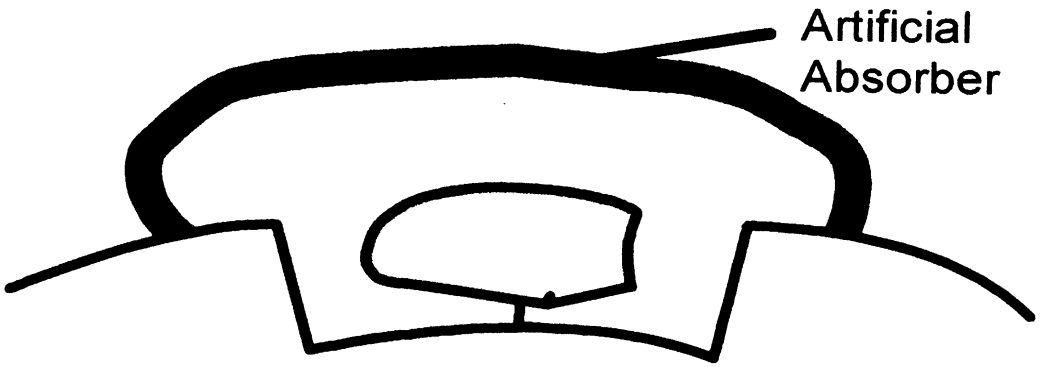

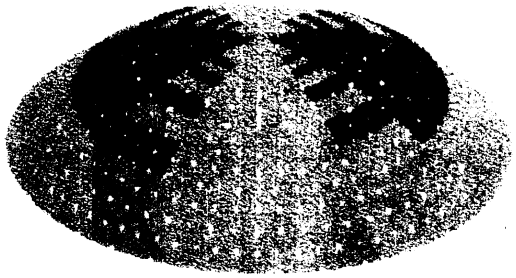

FEAURES/CAPABILITIES

- Finite Element Antenna Analysis Code
- Prismatic element for mesh generation (retains geometrical generality in one dimension)
- Boundary Integral or Artificial absorber for mesh truncation

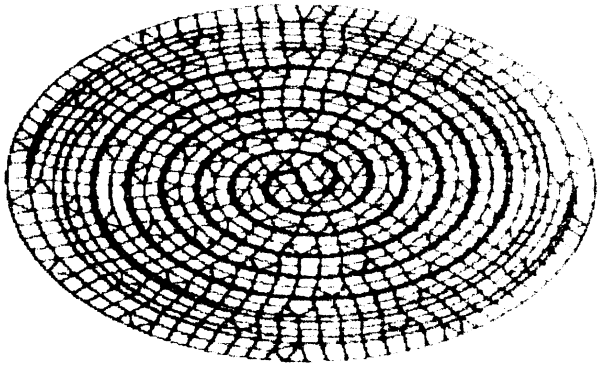

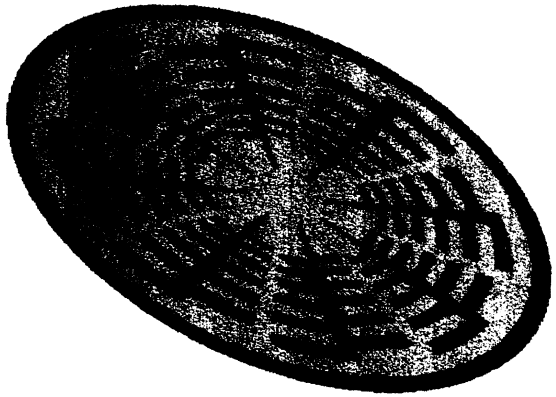

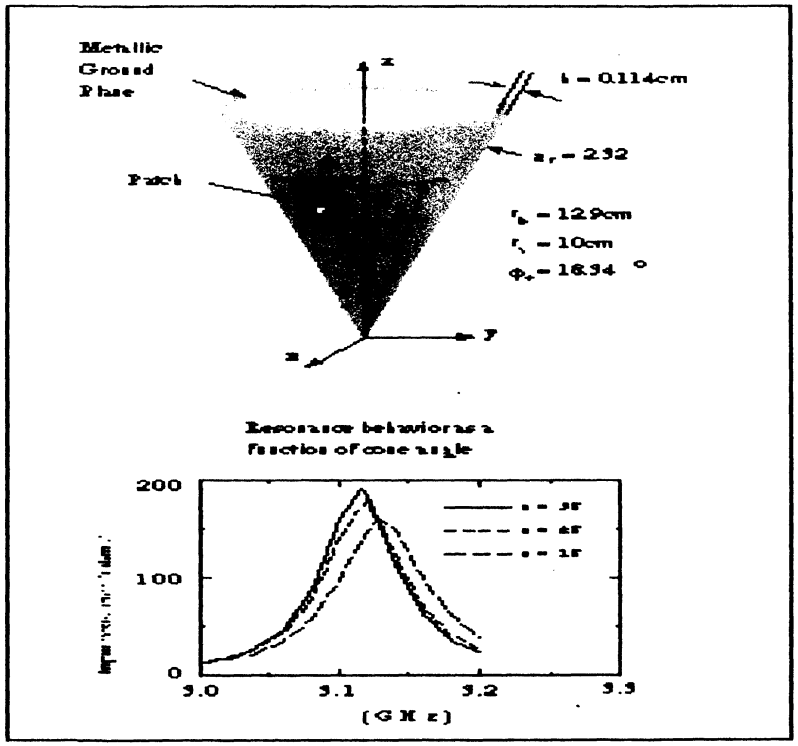
Metallic
Ground
Plane
Patch
t = 0.114cm
z, = 2.32
r, = 12.9cm
r, = 10cm
Φ, = 16.34 °
Resonance behaviors a
function of cone angle
200
100
0
3.0
3.1
3.2
3.3
(GHz)

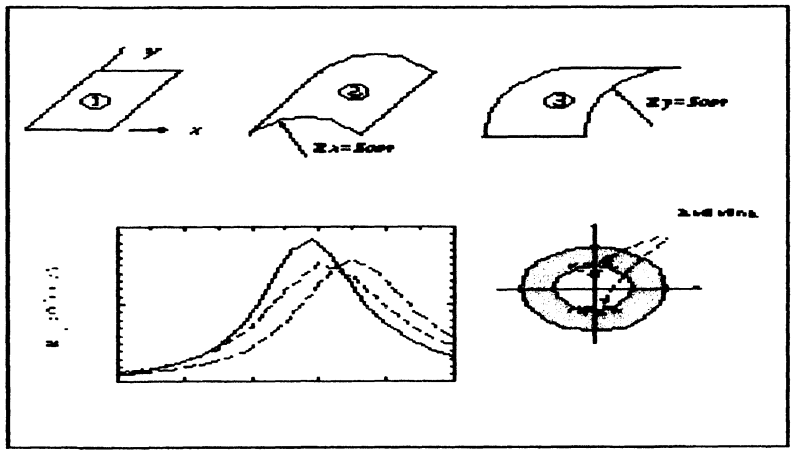
y
x
①
②
③
Zy=Sour
Zx=Sour

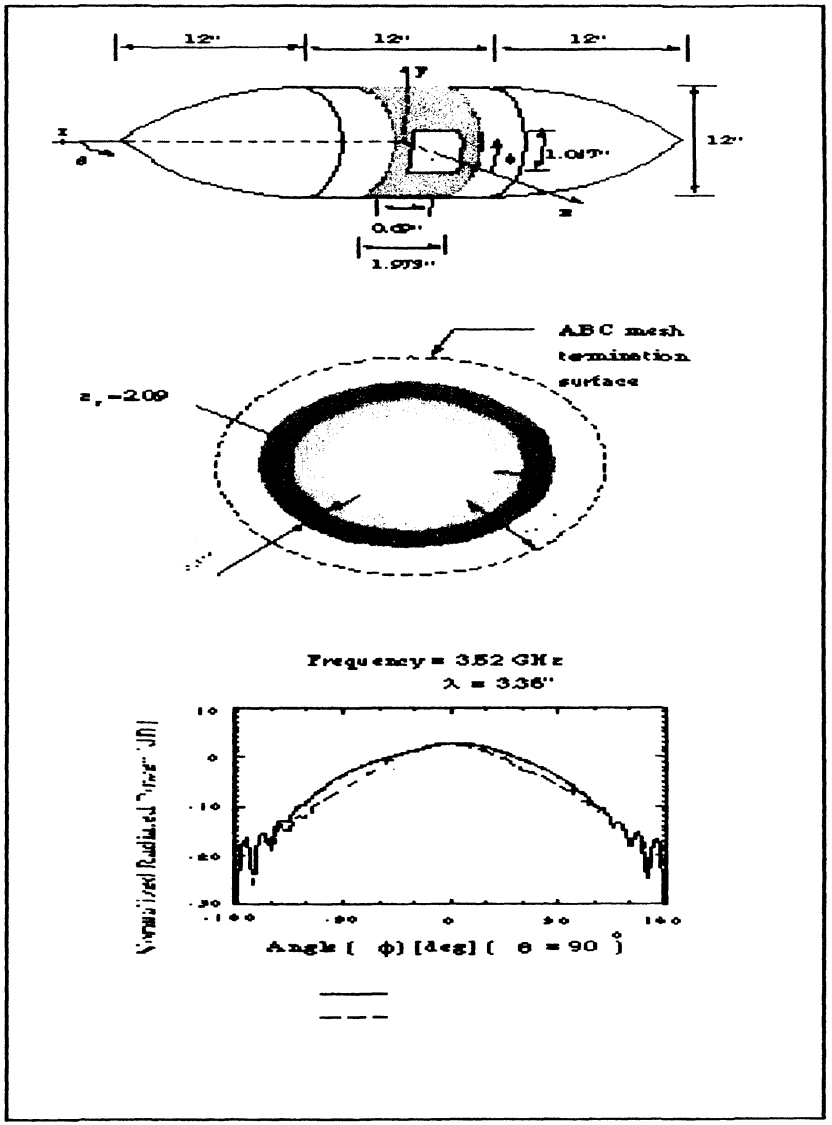
12"
12"
12"
12"
1.047"
0.052"
1.979"
ABC mesh
termination
surface
z, =2.09
Frequency = 3.52 GHz
λ = 3.36"
Angle (ϕ) [deg] (θ = 90 °)

Univ. of Mich
FEMA-PRISM

ARRAY: 1 Ref. Element
6 Auxiliary Elements
Center on a 3.5" Radius

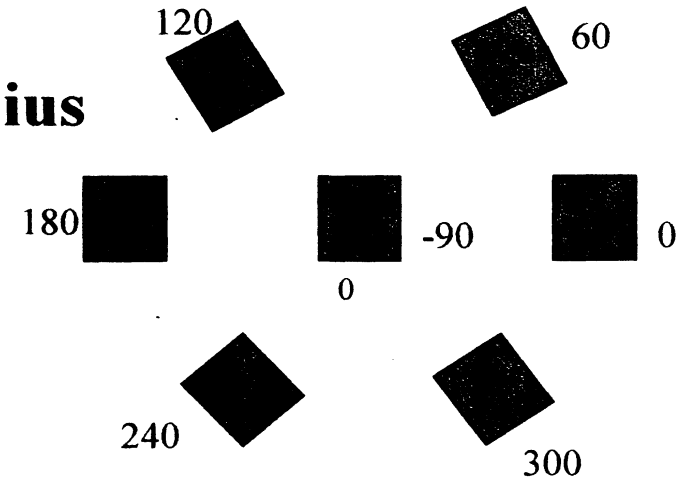

ε_r=3.468

Square Patch 1.94"

Cavity: 16.46"x11.96" Depth=0.2"

Frequency L1=1575.42 MHz

```
Title:  MATLAB graph
Creator:  MATLAB, The Mathwork
CreationDate:  08/08/96  12:04
```

```
Title:  nulcut.eps
Creator:  XMgr v3.01pl7
CreationDate:
```

TRIANGULAR CAVITY SLOT

NEAR FIELDS

E_x

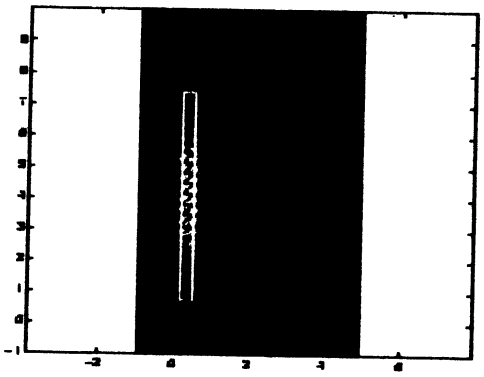

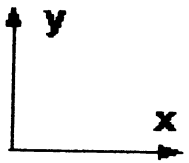

E_y

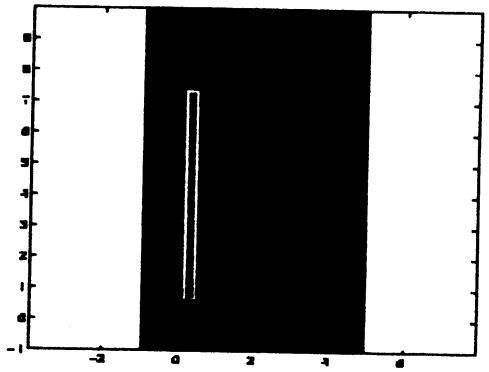

NORMALIZED RADIATION PATTERN

E_θ

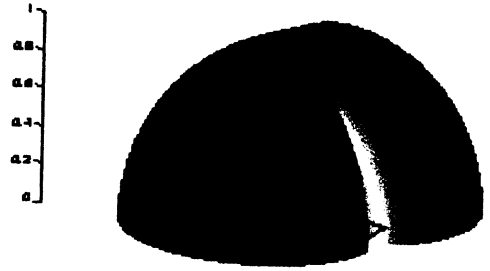

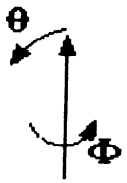

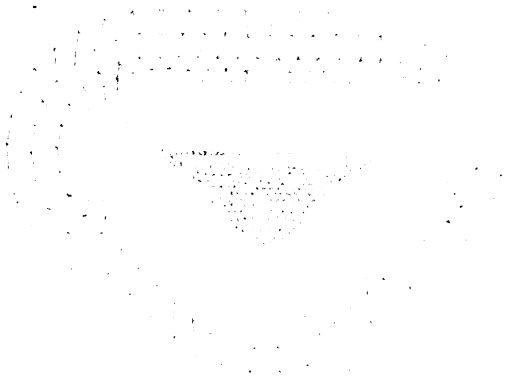

Other Antennas Analyzed With Hybrid Finite Element Techniques

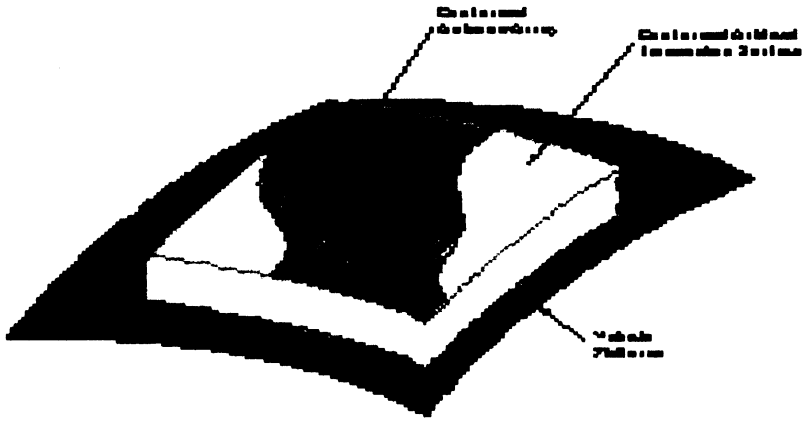

Patch Array on Curved Platform

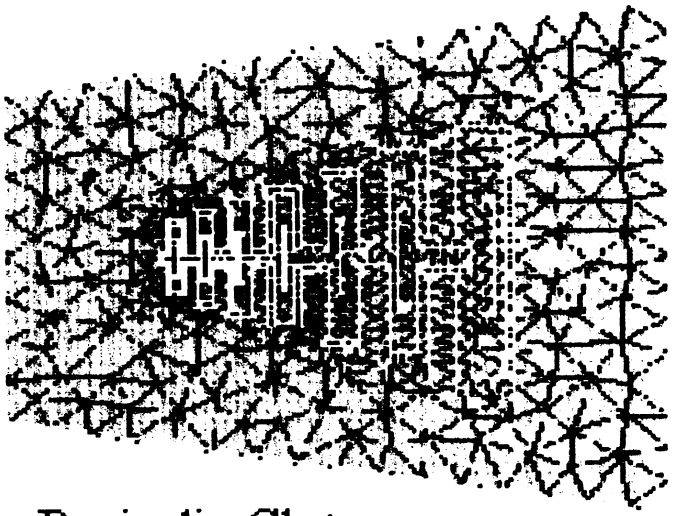

Log-Periodic Slot

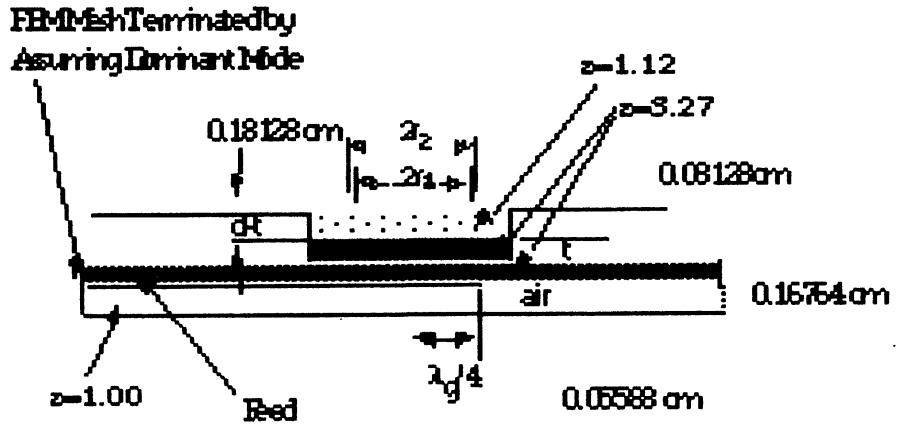

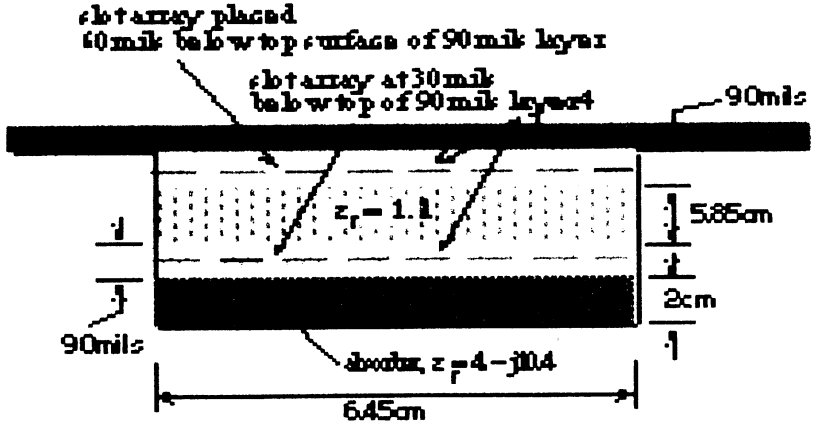

Array Below Frequency Selective Surface

Broadband Antennas On Doubly Curved Surfaces

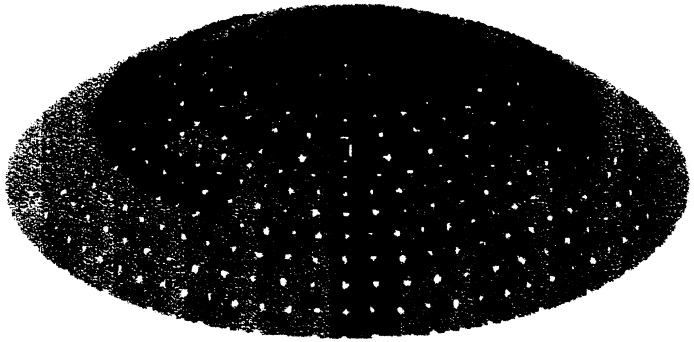

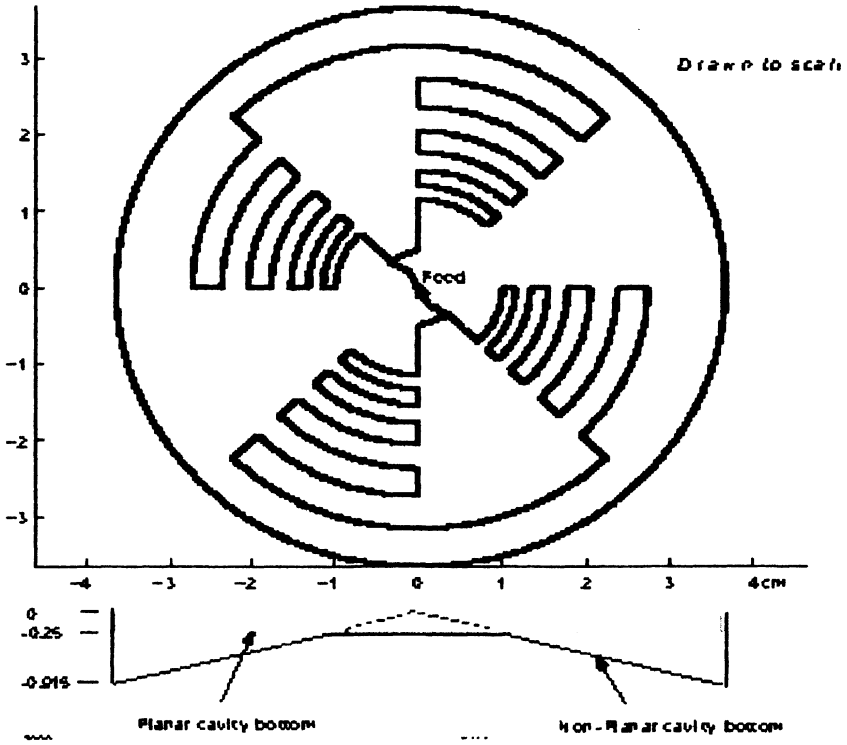

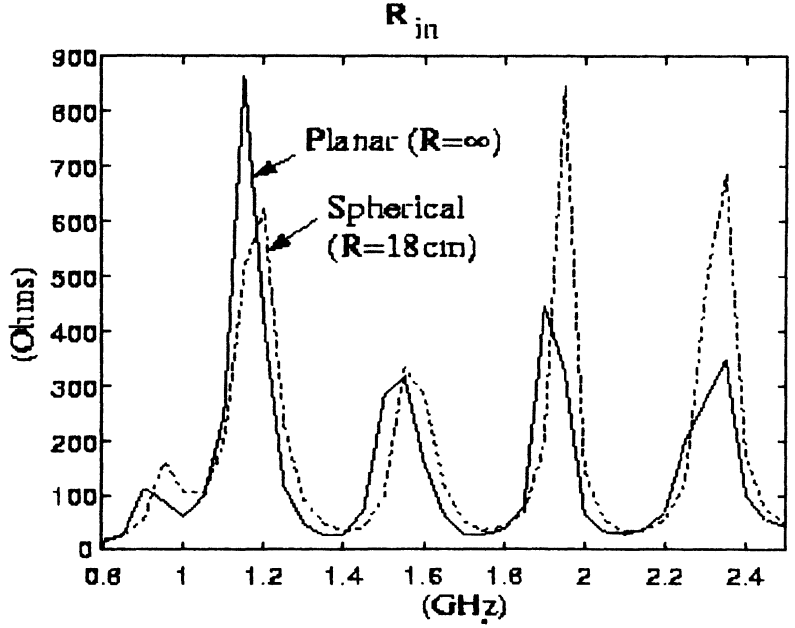

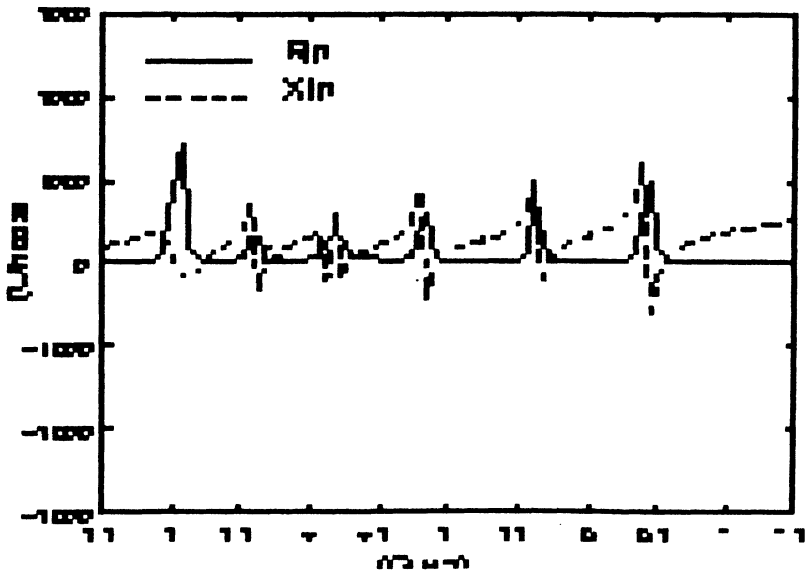

Slot Spiral Performance and Design for Personal Communications

GEOMETRY

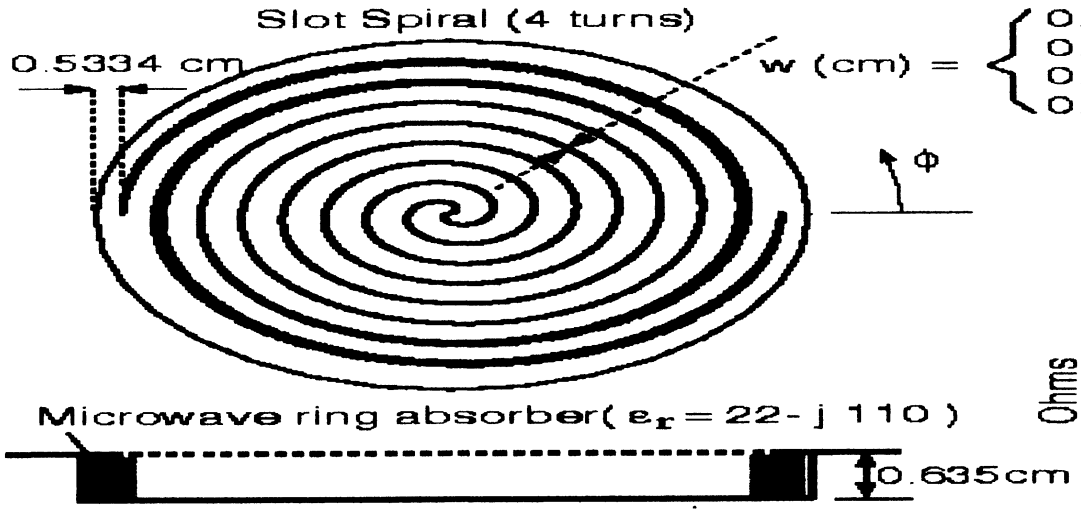

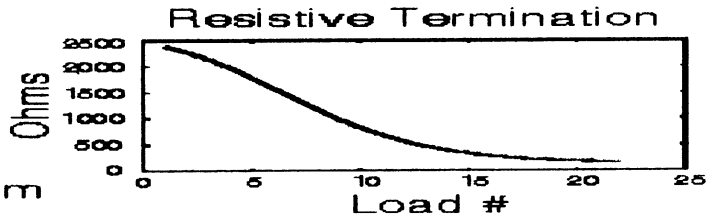

SURFACE MESH

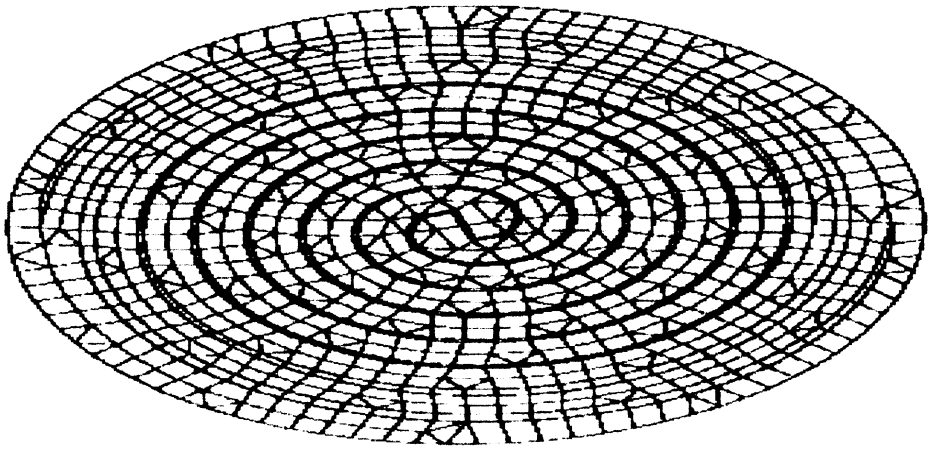

Sampling cell size = 0.53cm

Frequency band:
0.8 ≤ f ≤ 3 GHz

Sampling rate:
(71 → 19) / λ

MIX of PRISMs and distorted BRICKs

FIELD BEHAVIOR INSIDE THE SLOT

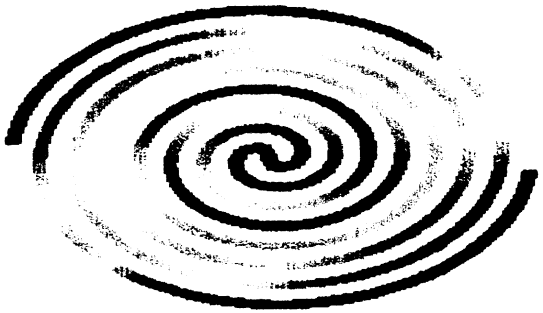

0.8 GHz

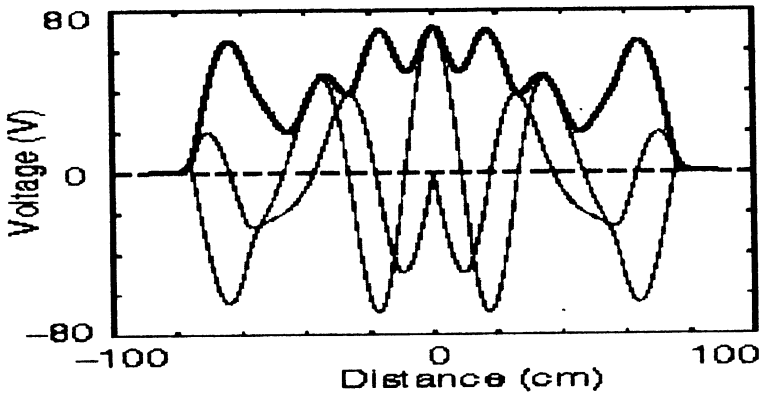

Z_{in} = 71+j0 Ω

G = - 9 dB

AR = 4 dB

1.9 GHz

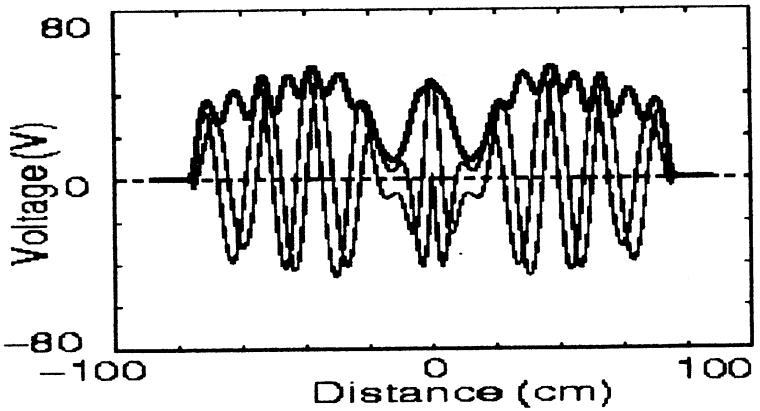

Z_{in} = 46+j2 Ω

G = 5 dB

AR = 2 dB

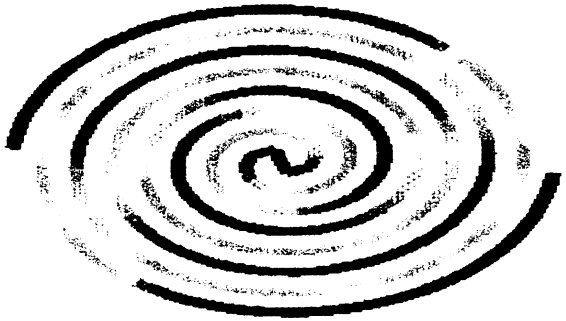

3.0 GHz

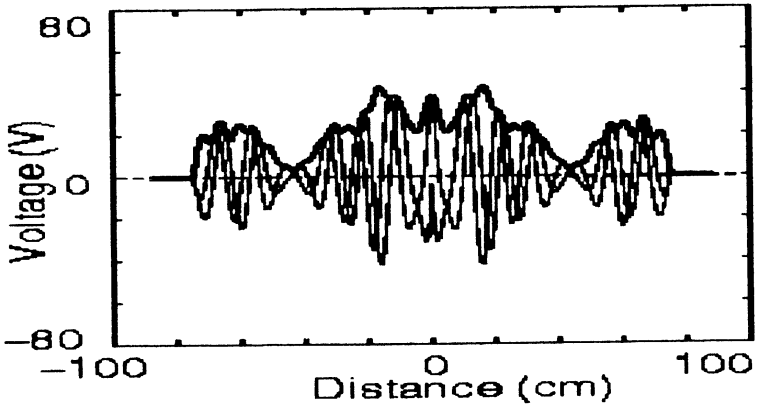

Z_{in} = 37-j4 Ω

G = 8 dB

AR = 1 dB

ORIGINAL AND IMPROVED DESIGNS

FROM FEMA-PRISM COMPUTATION

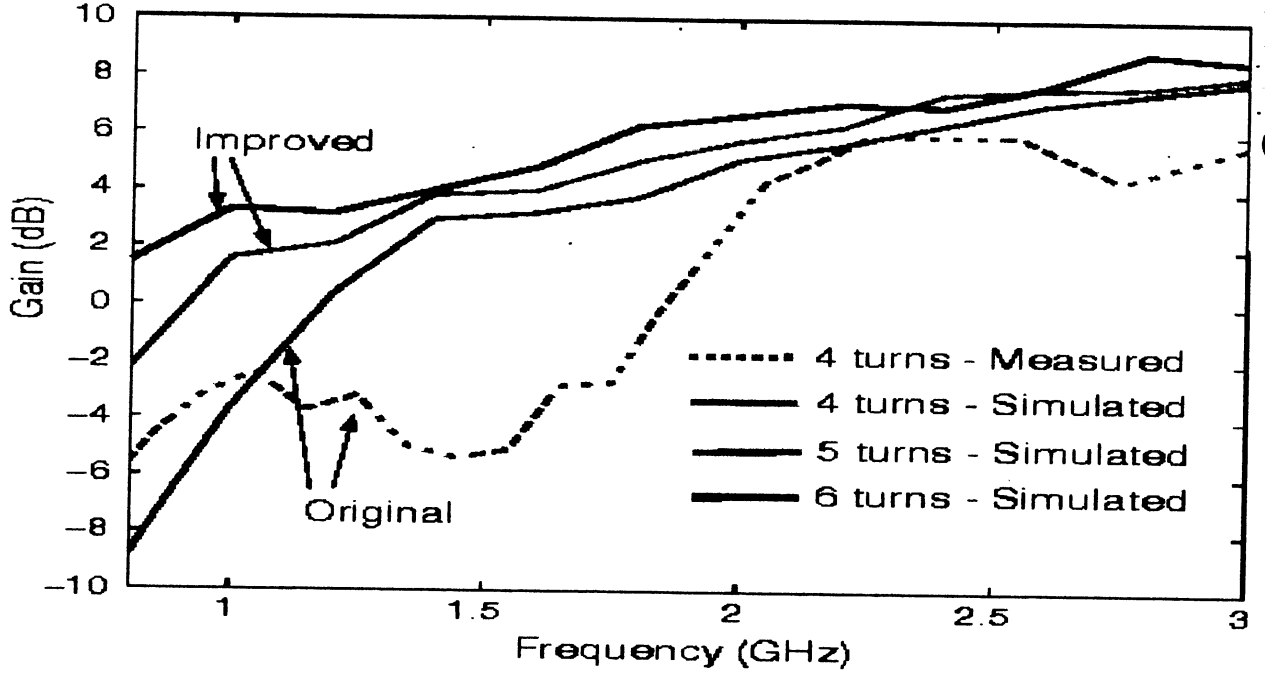

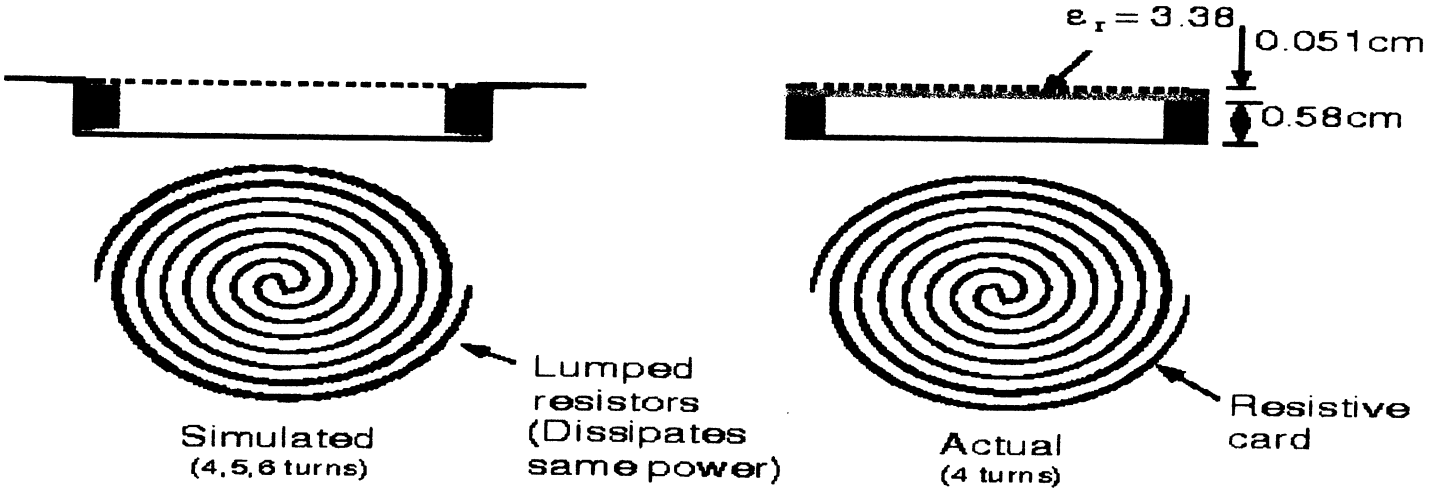

PERIODIC PRISM CURRENT FEATURES

- **Flexible (Materials and Geometry), Rigorous and Fast.**
- **Incorporates fast algorithms for the fastest O($N^{1.3}$) simulation**
- **Models arbitrary shape element (planar and non-planar)**
- **Periodic and non-periodic broadband element**
- **Curved and Planar**
- **FSS, planar and non-planar inhomogeneities**

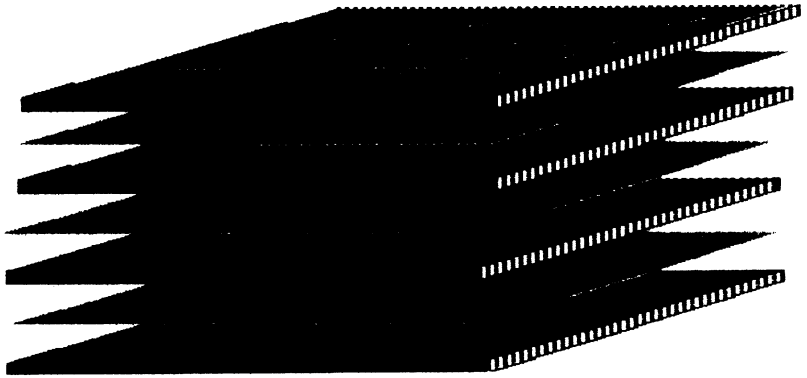

Multilayered power-combining networks

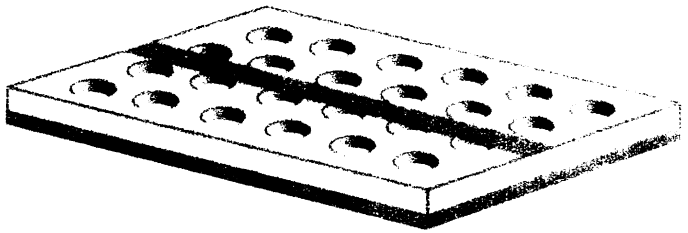

Bandgap can be easily modeled using periodic array features

Sctructurally Embedded Arrays

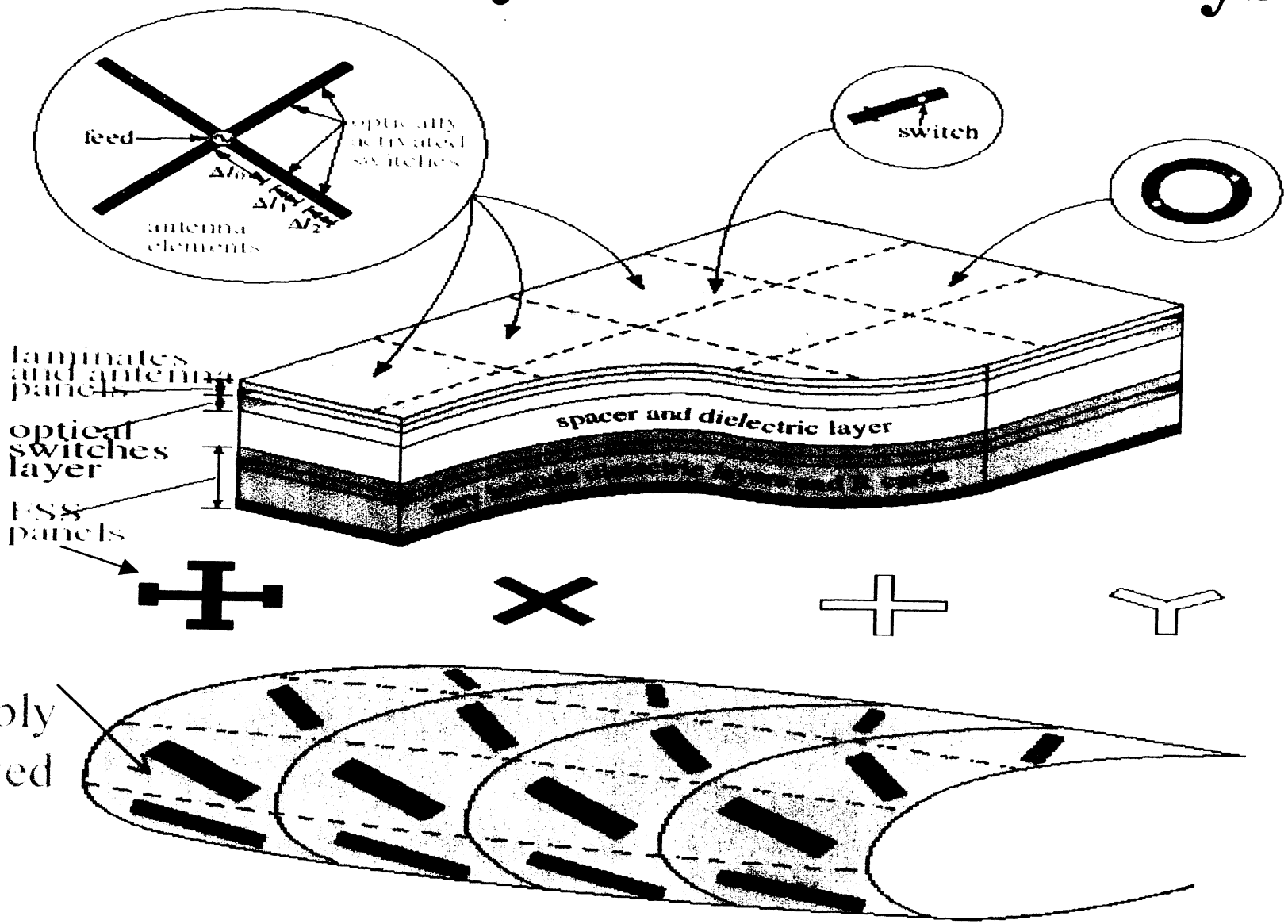

Hybrid FEM-BI Formulation for Arrays

- Periodic Boundary Condition (PBC) for FE-part

- Periodic Green's Function (PGF) for BI-part

- Metallic patches in all layers possible (Antenna, FSS)

- Probe current feeds and plane wave excitation

- Lumped impedances / resistive sheets

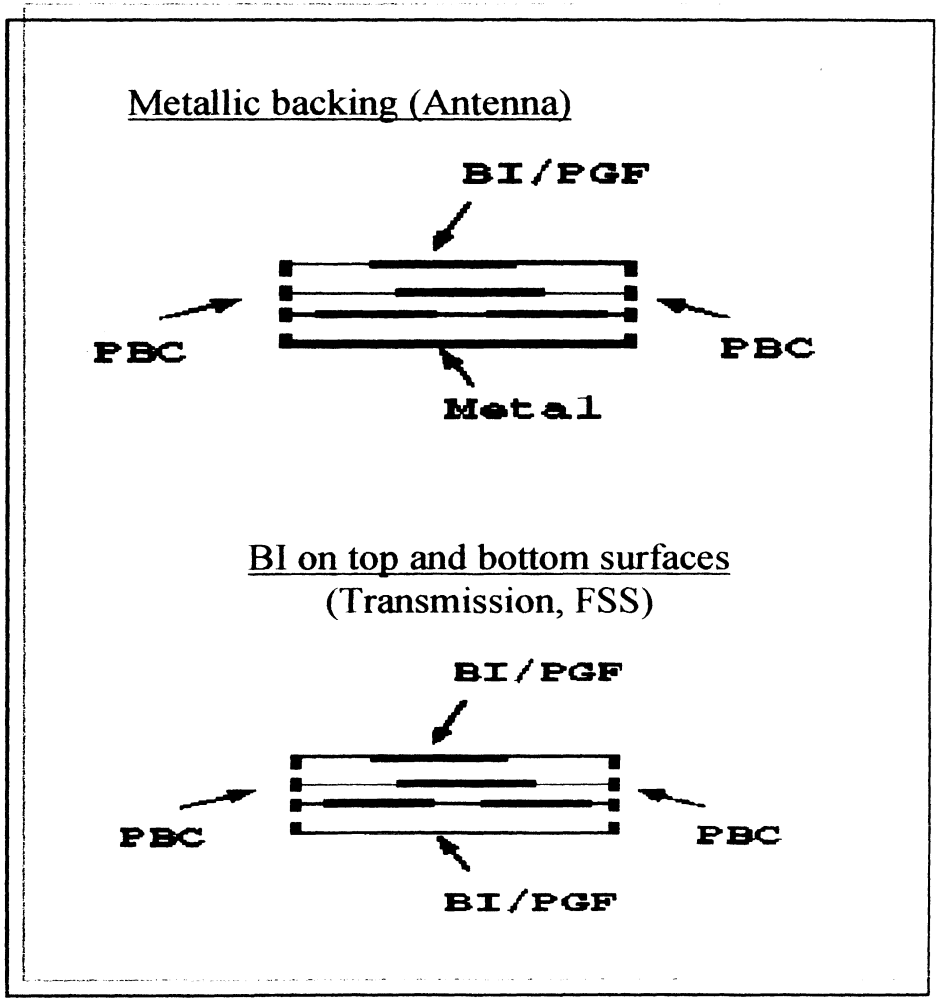

Double Layer FSS with Antenna

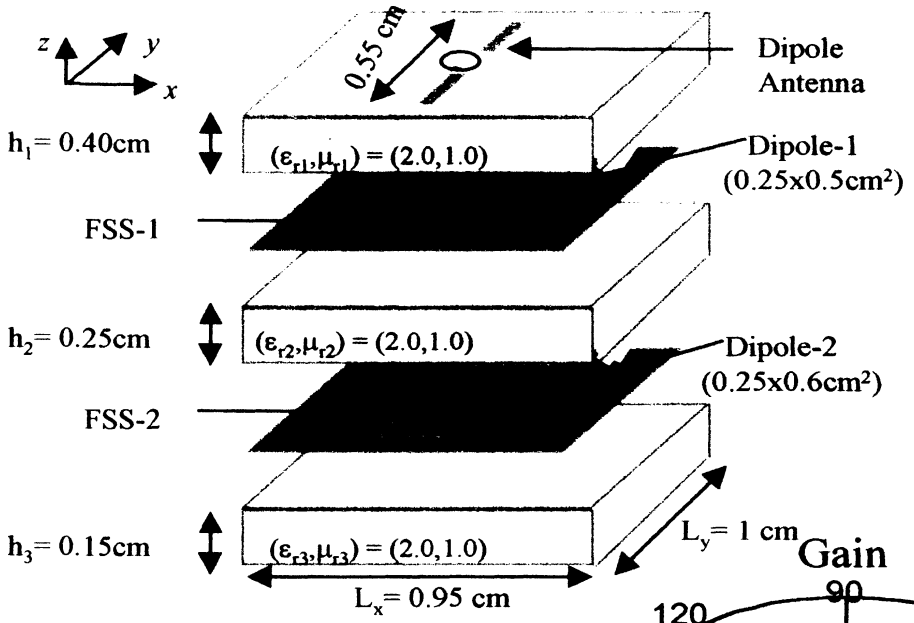

θ = 0-90°, ϕ = 0°
f_o = 17.25 GHz
FEM sample size = 0.05 cm
FSS with 1-cell :
No. of unknowns = 16702
FFT pad size = 64x64
No. of iterations = 323
CPU time = 333.25 sec

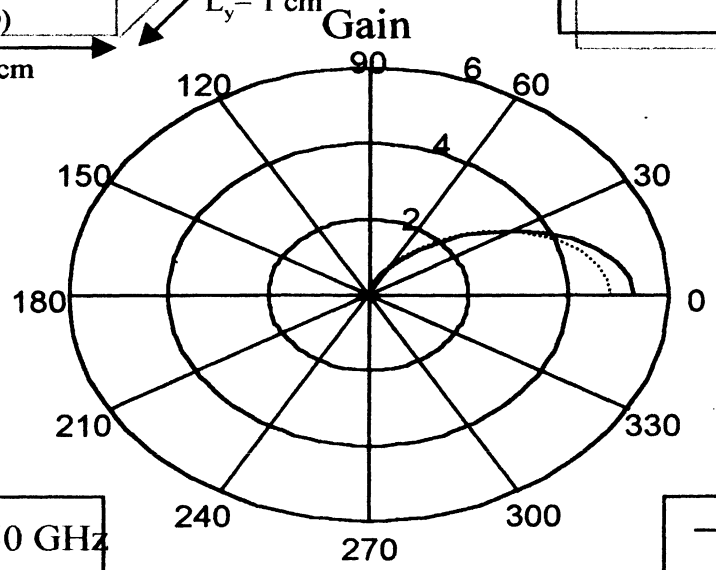

f_o= 13.50 GHz
Z_{in}= 22.6-j26.3 ohm

f_o= 17.25 GHz
Z_{in}= 118.8+j23.2 ohm

Periodic -PRISM
Non-Commensurate Array Validation

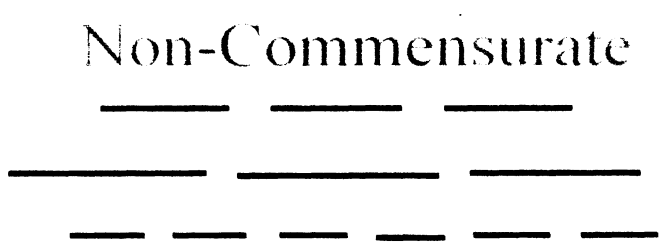

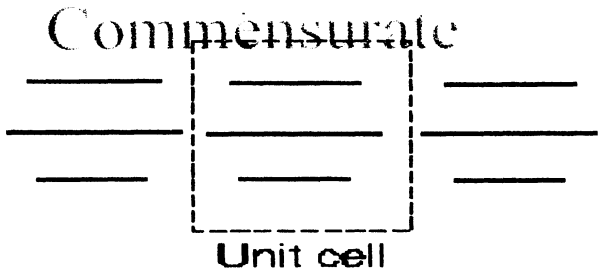

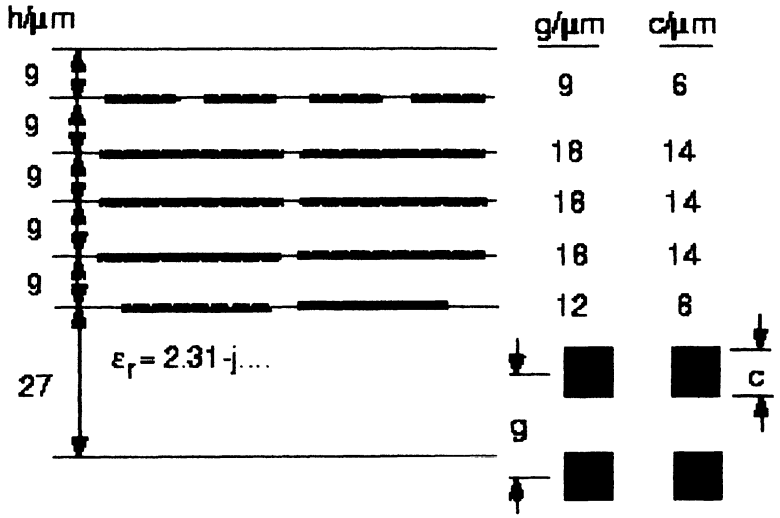

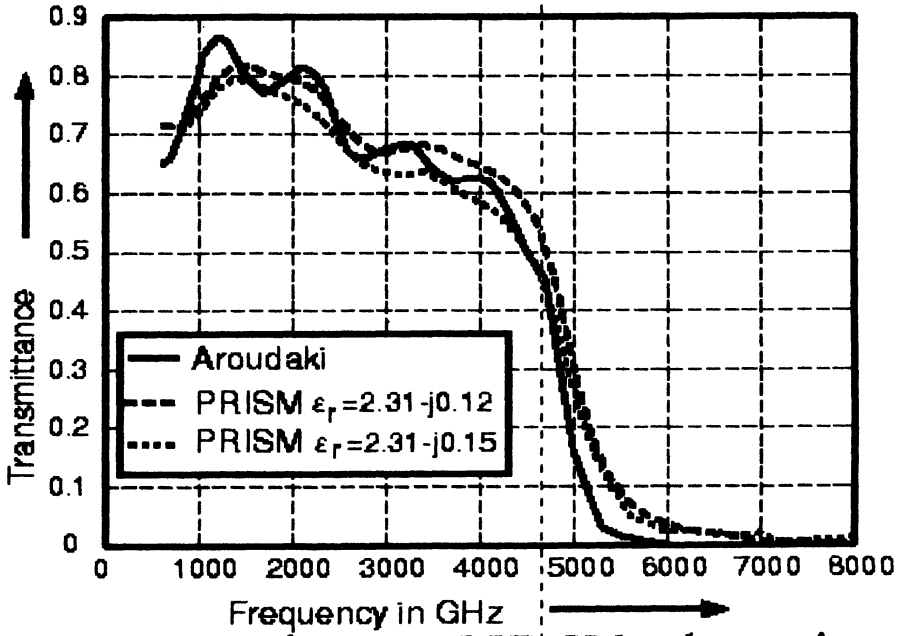

CPU: about 1/2 hour per frequency point on HP Workstation

Dipole Array Embedded in Dielectric Layer Analyzed with Periodic PRISM

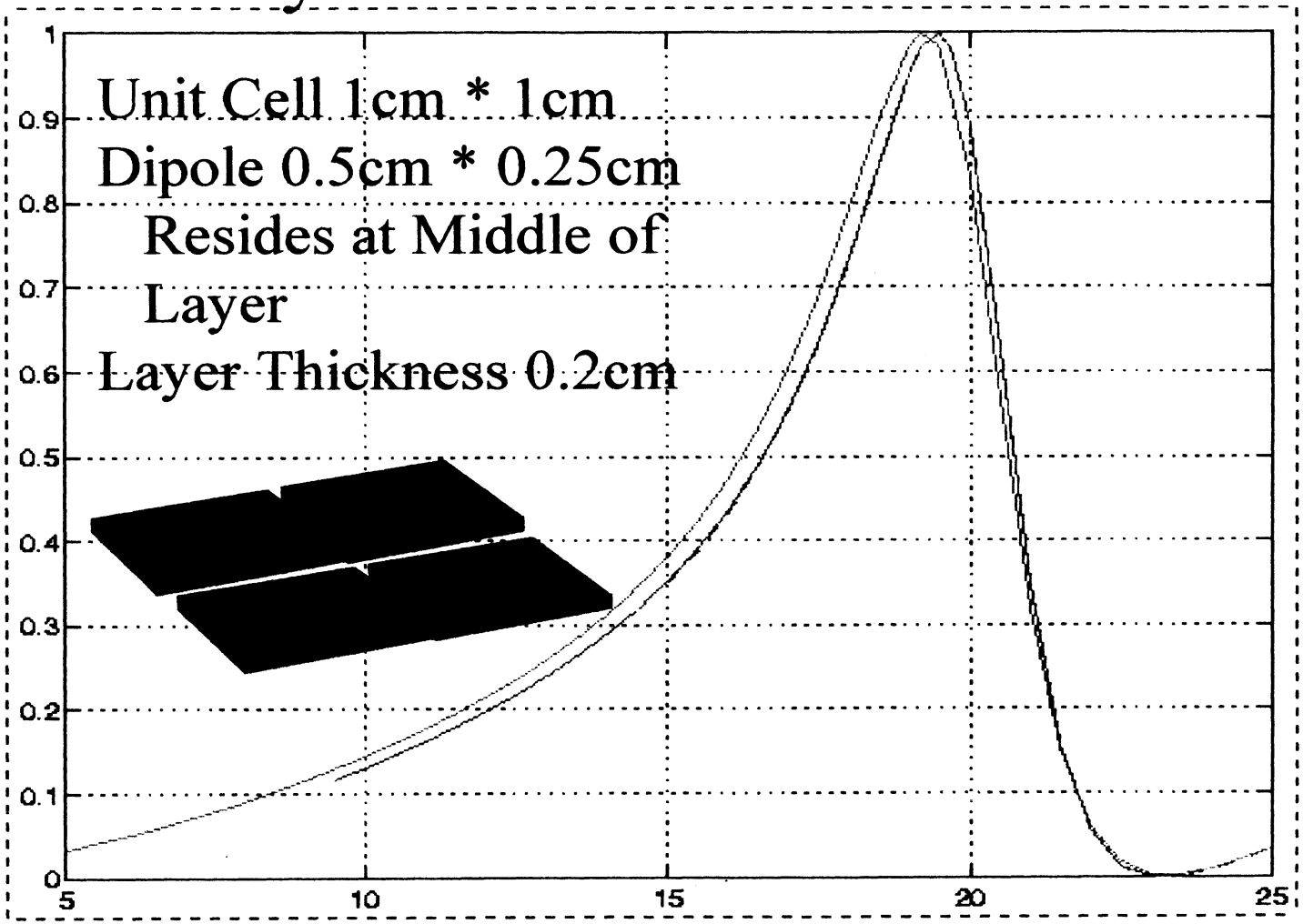

CPU Times 32x32 Grid Run Data Conentional vs. AIM

DOFs = 35,432(vol) + 2x3136(Surface)

Memory: with AIM: 2183k elements (26MB)
w/o AIM: 20,000k elements (240MB)

CPU(IBM RS6000):

AIM
FILL= 38sec(FEM)+1930sec(BI)+95sec(BI)
BCG Solver= 415 Iterations (1081sec)
Total CPU=3049sec (~50min)

Conventional
FILL=38sec(FEM)+7330sec(BI)
BCG Solver=364 Iter. (1446sec)
Total CPU=8814sec(~2.5 hours)

AIM reduced

memory by a factor of 9

CPU by a factor of 3

Fast Algorithms

- FMM, Windowed FMM, FAFFA,Multi-Level FMM,AIM
- CPU and Memory Requirement Reductions for FMM

  $O(n^{1.5})$ FLOPS

  $O(n^{1.5})$ Memory/Storage
- FMM/AIM vs. Conventional Method

  $O(n^2)$ vs. $O(n^{1.5})$ FLOPS

  $O(n^2)$ vs. $O(n^{1.5})$ Memory Locations

FMM's Idea for

Matrix-Vector Product

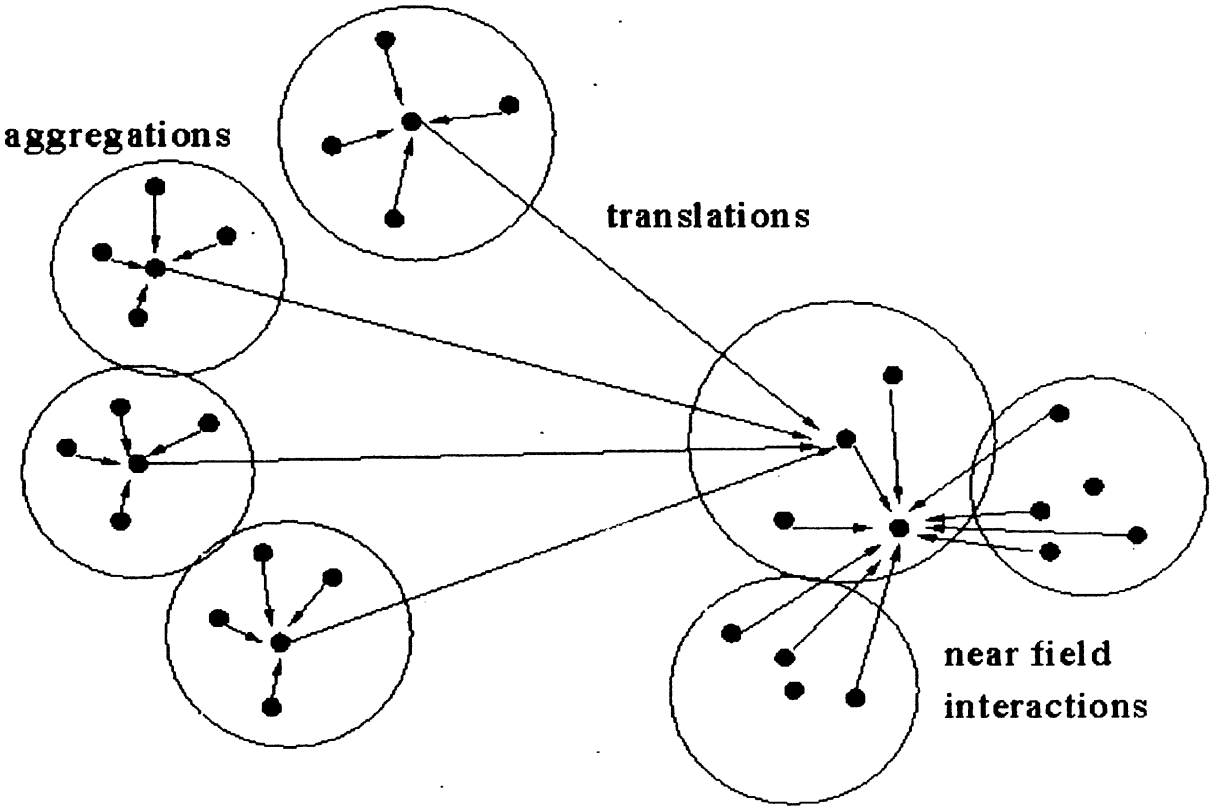

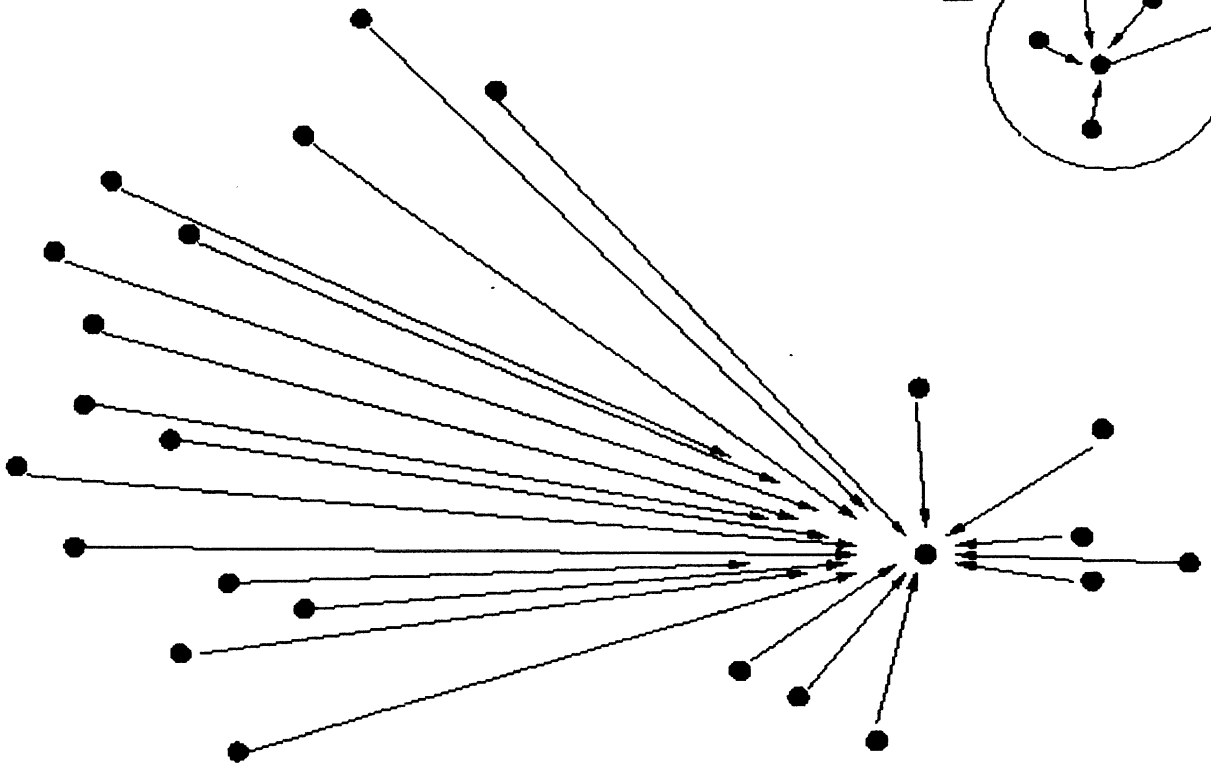

Plain FE-BI Strategy

Curved Array Analysis With FMM Speed-UP

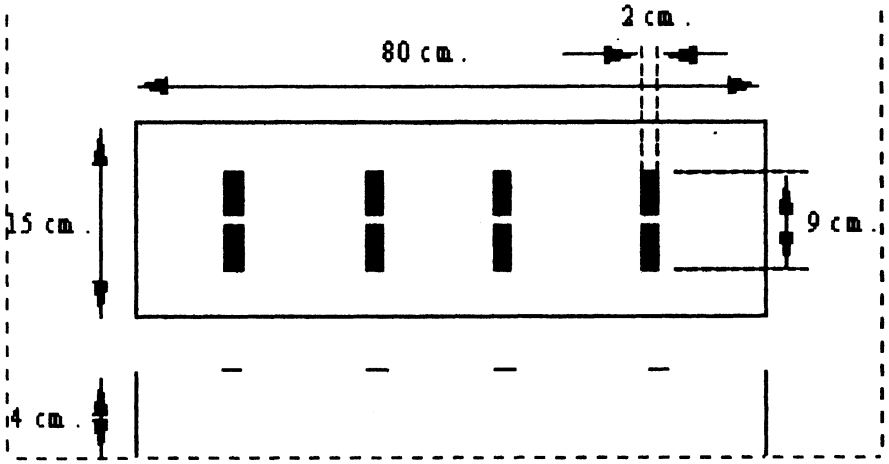

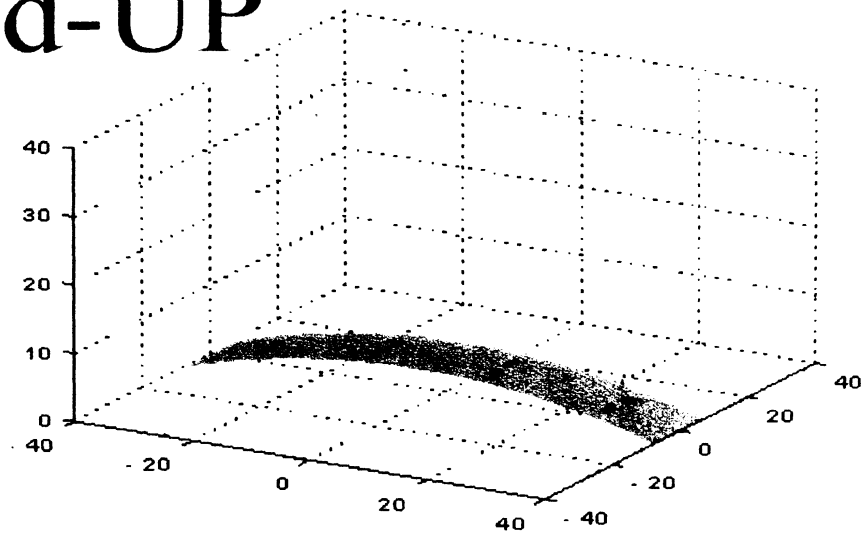

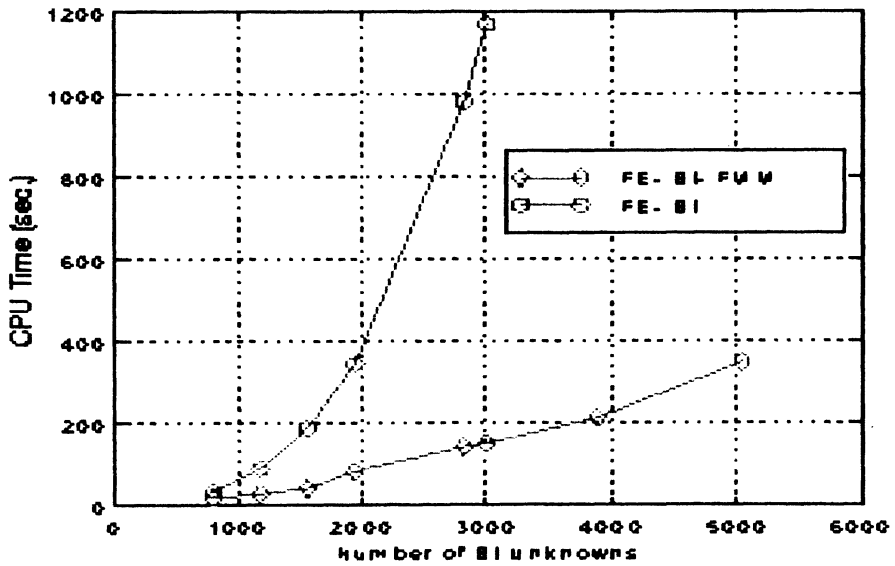

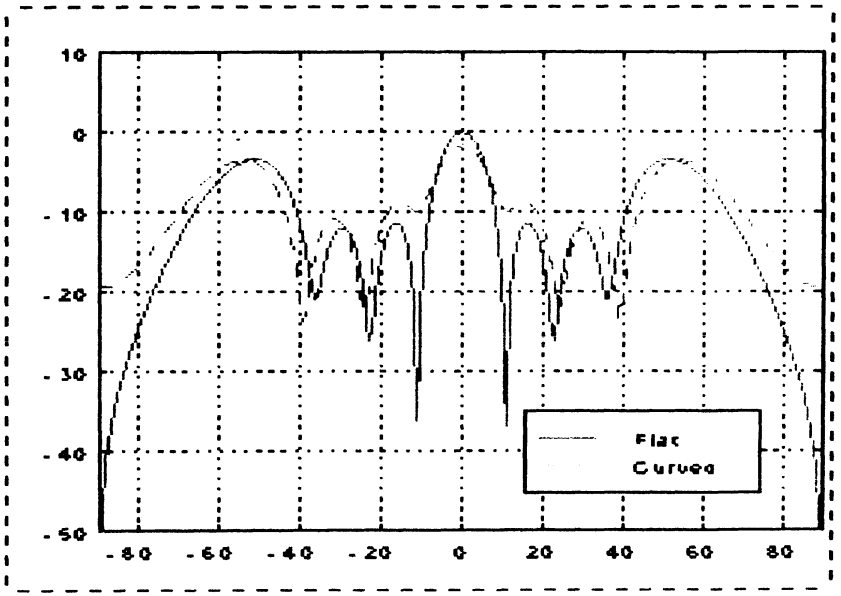

Design Optimization Approach in Conjunction with FEM

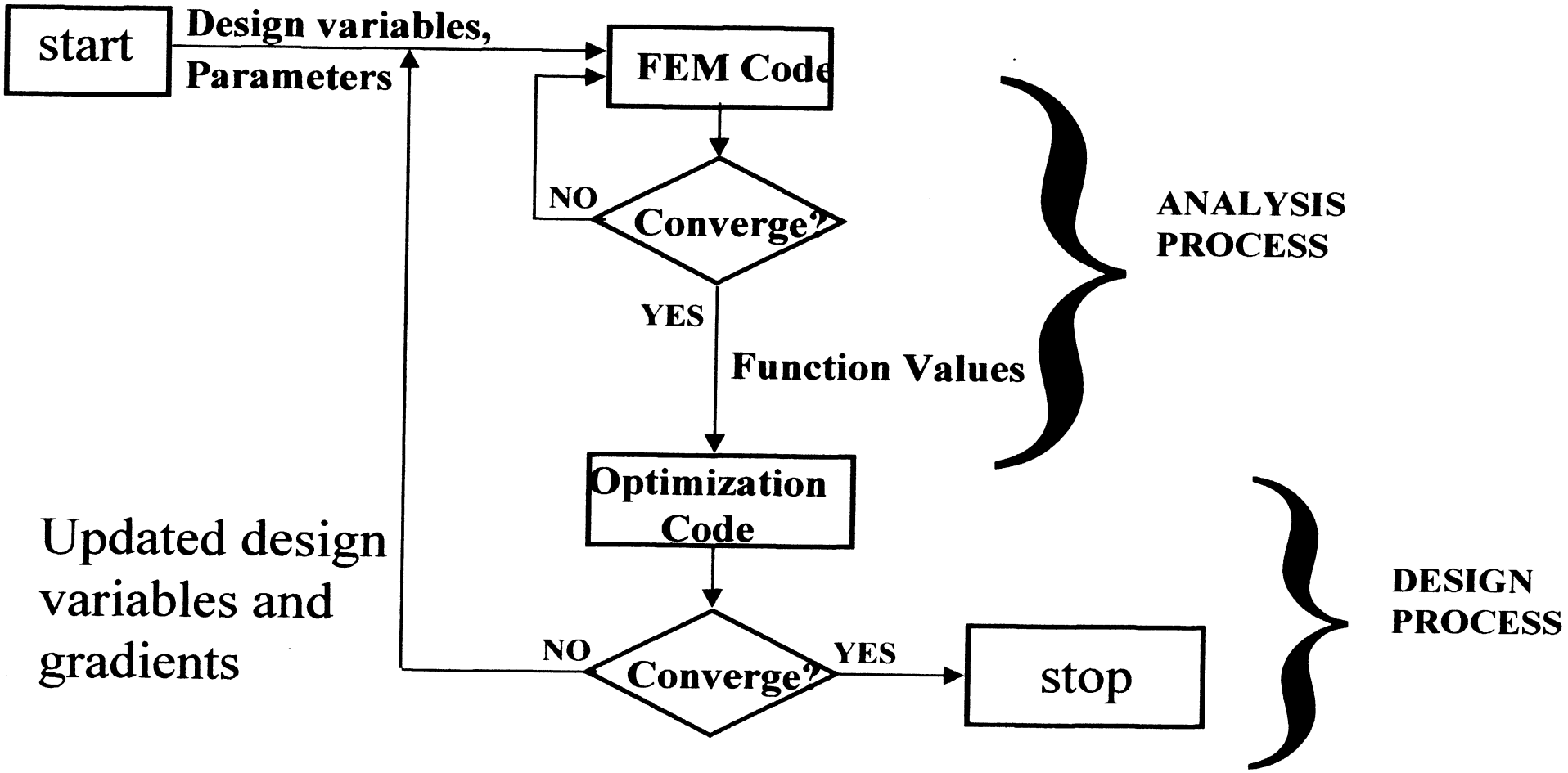

Slot Fed Dual Patch Antenna: Design for a Specified Bandwidth and Frequ.Using SQP: Varying 3 Parameters

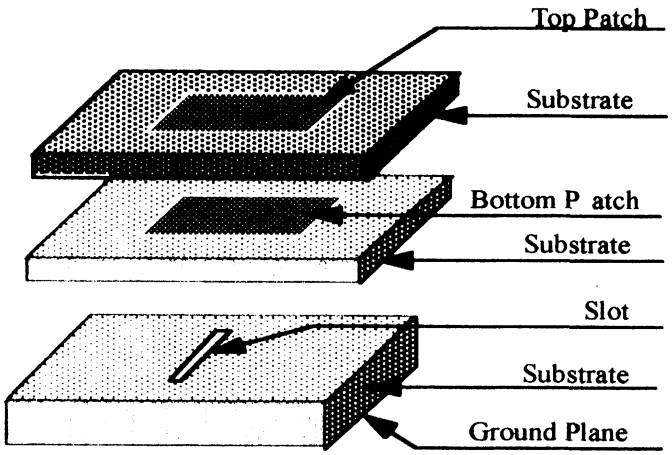

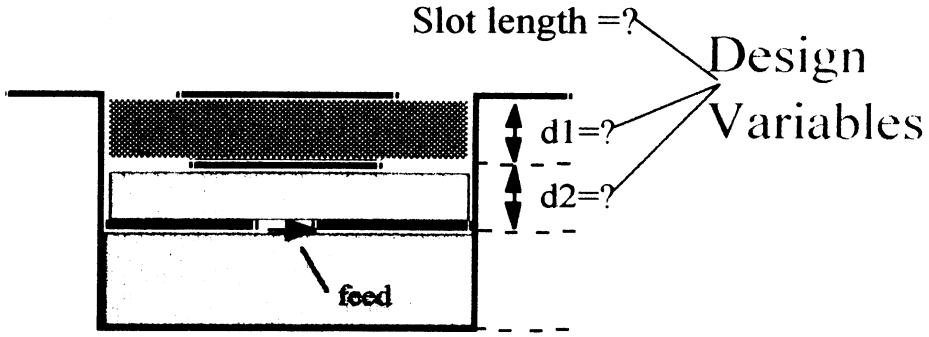

Performance at d1=0.85 mm, d2=0.55mm, slot length=4.0 mm

FINAL DESIGN:

VSWR = 1.414
BW = 18%

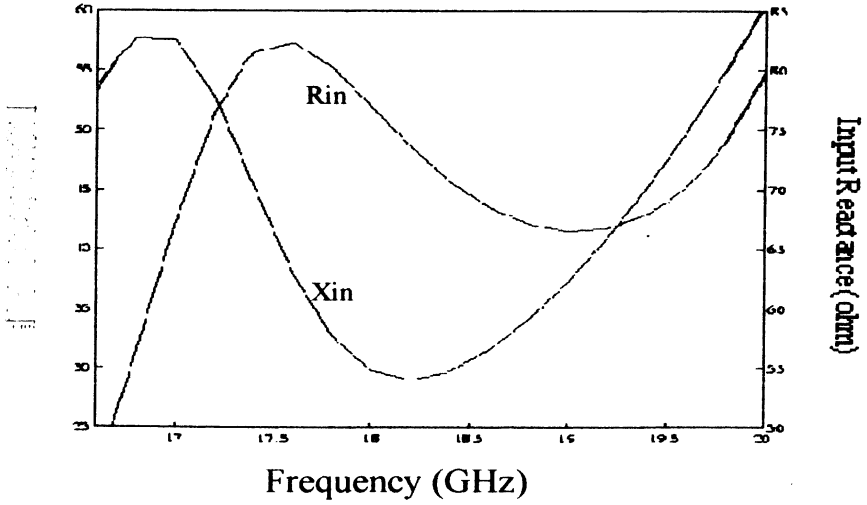

FE-BI Solutions with Fast Integral Methods

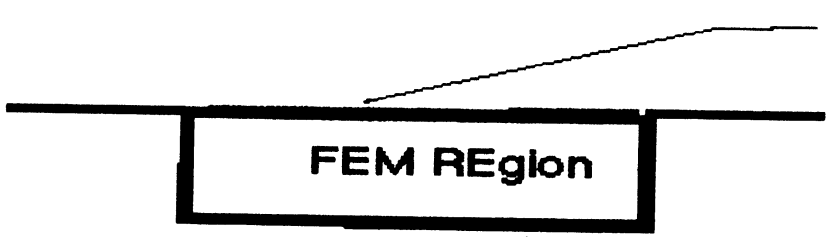

Boundary Integral

FE-BI

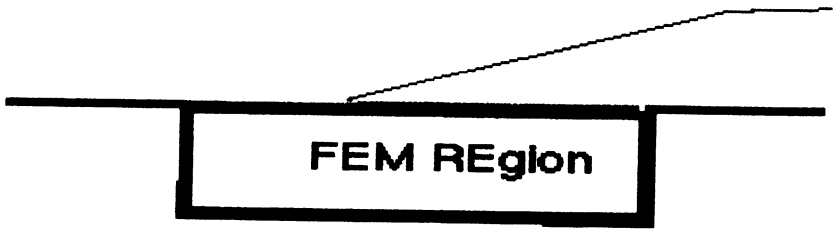

Boundary Integral Using
FFT for Matrix Products

FE-BI(CGFFT)

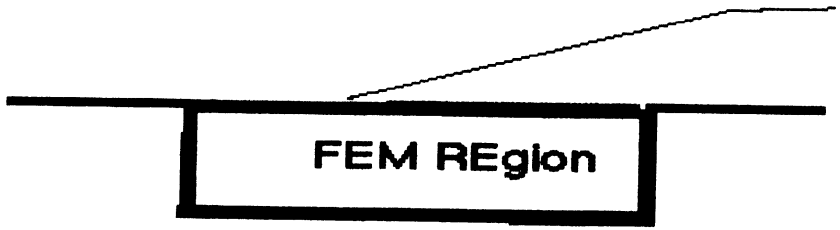

Boundary Integral with
Fast Multipole Method
for Matrix Products

FE-BI(FMM)

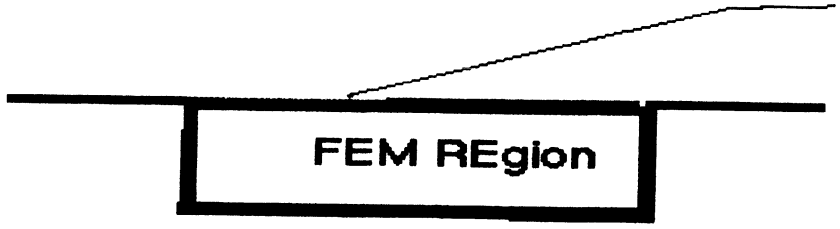

Boundary Integral with
Adaptive Integral Method
for Matrix Products

FE+BI(AIM)

Radiation from a cavity-backed slot array computed with FE-AIM

(ϕ = 90 plane)

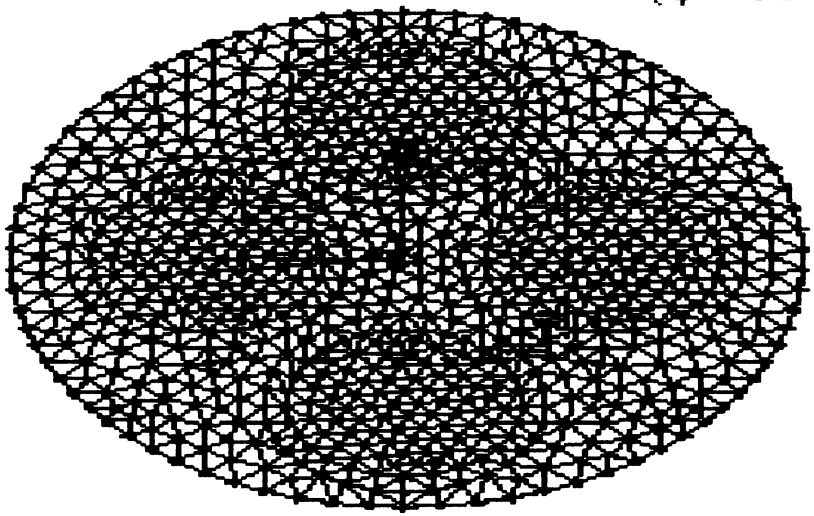

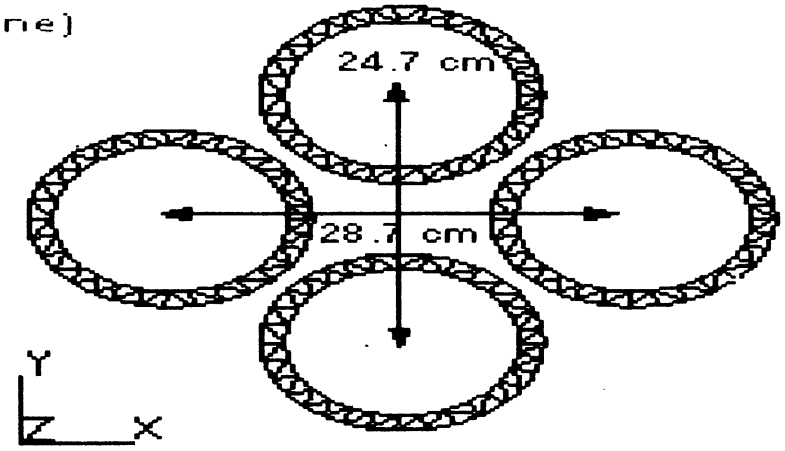

Total Edges: 5529 Non-PEC: 983
Surface Edges: 2110 (PEC)
496 (Slot) 248 (Non-Pec)

Inner radius of each slot = 7.325 cm
Cavity diameter = 49.4 cm
Cavity depth = 1.5 cm
Cavity filling $\varepsilon_r = 2$
Slot width = 1.5 cm
Frequency = 1 GHz (Lambda = 30cm)

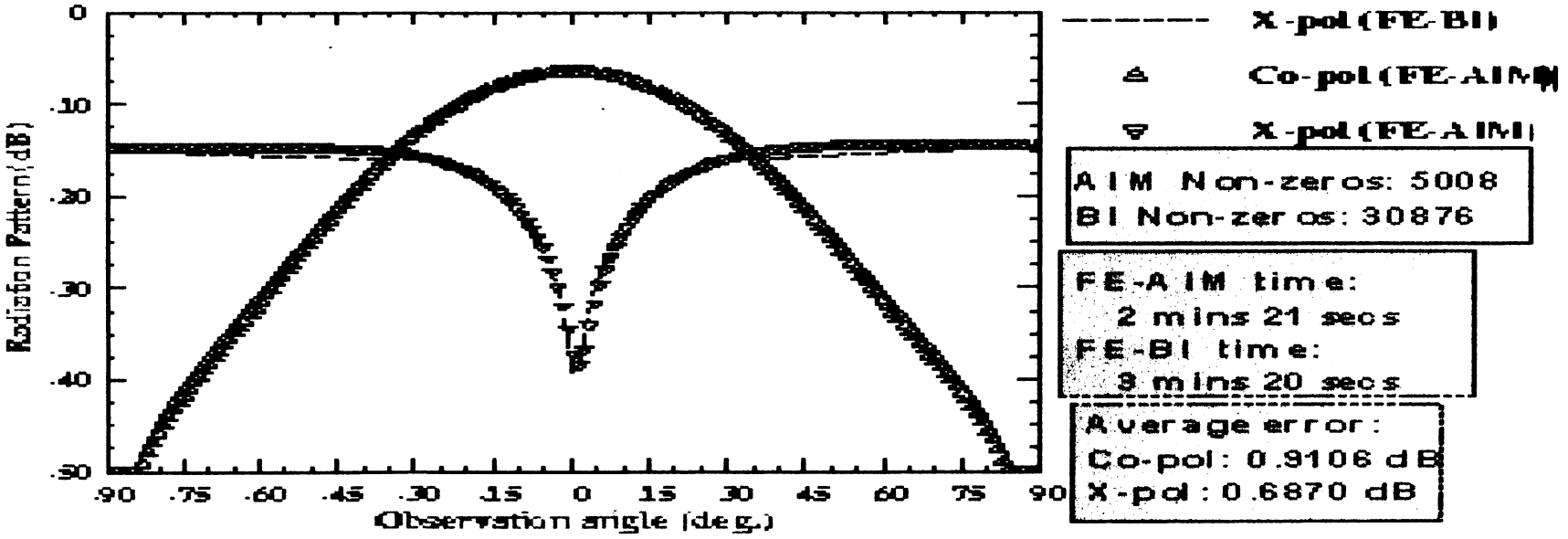

Input impedance of a very narrow annular slot computed with the FE-BI and FE-AIM

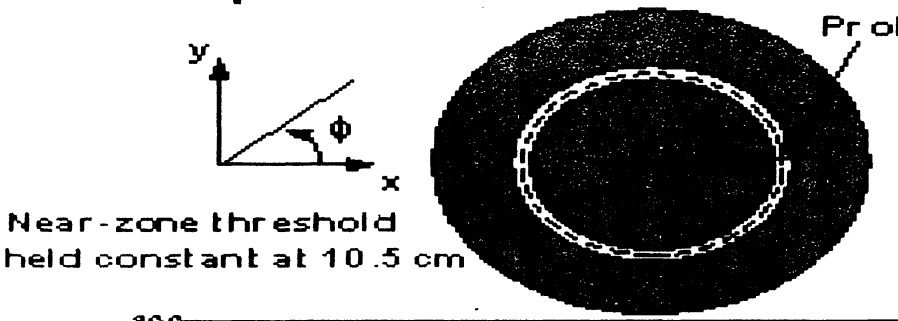

Near-zone threshold held constant at 10.5 cm

a = 12.35 cm
b = 0.75 cm
ρ_0 = 7.7 cm

Near Z non-zeros
BI : 4656
AIM : 2245

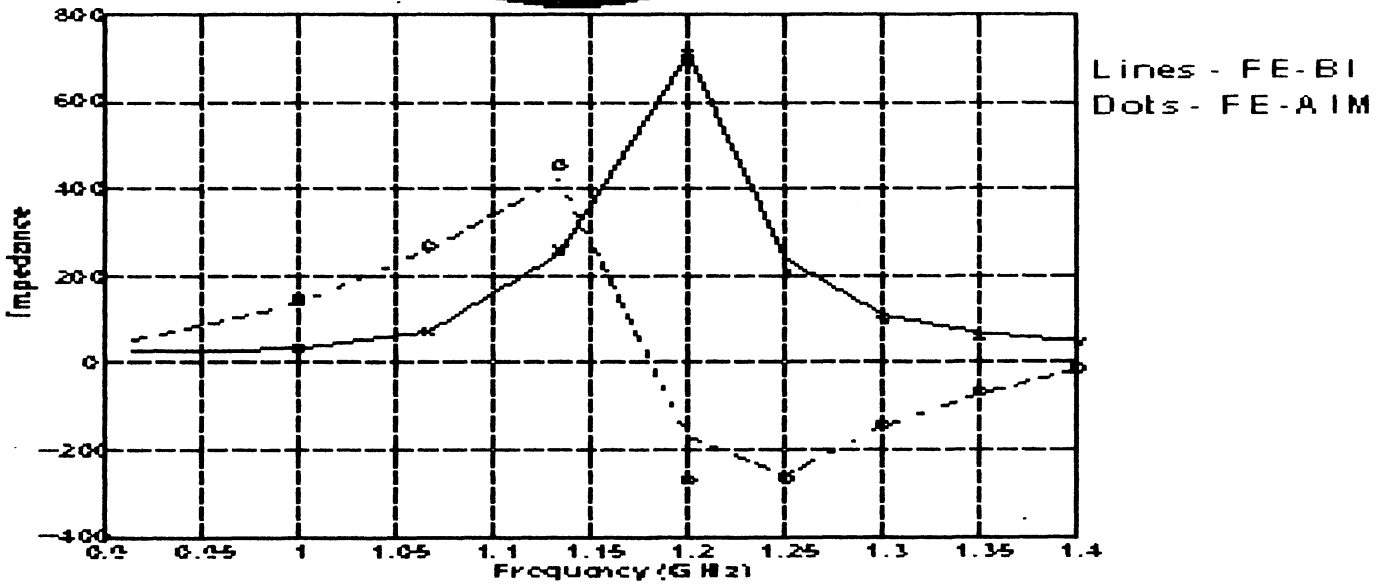

Frequency (GHz)	FE-BI	FE-AIM
1.0667	71.74 + j259.04	71.46 + j268.51
1.1333	248.51+j422.88	258.03 + j453.73
1.2	708.59-j170.31	710.39 - j269.71
1.25	238.47-j259.27	206.96 - j266.05
1.3	109.77-j146.96	95.48 - j142.82
1.35	67.63 - j71.61	59.84 - j 67.16
1.4	49.7 - j16.48	44.42-j12.95

AIM for Boundary Integral Computation

MoM Average Sample size ~ 0.02λ
Edges ~1957
Unknowns ~ 1157
MOM Memory ~ 10.21 M
Solution time ~ 2 mins 45 secs

AIM Memory ~ 1.37 M
Solution time ~ 18 secs
(For 0.05λ grid spacing)
RMS Error ~ 0.0469 dB
(for both polarizations)

SMALL DETAILS
IN GEOMETRY

Note CPU
& Memory
Reduction

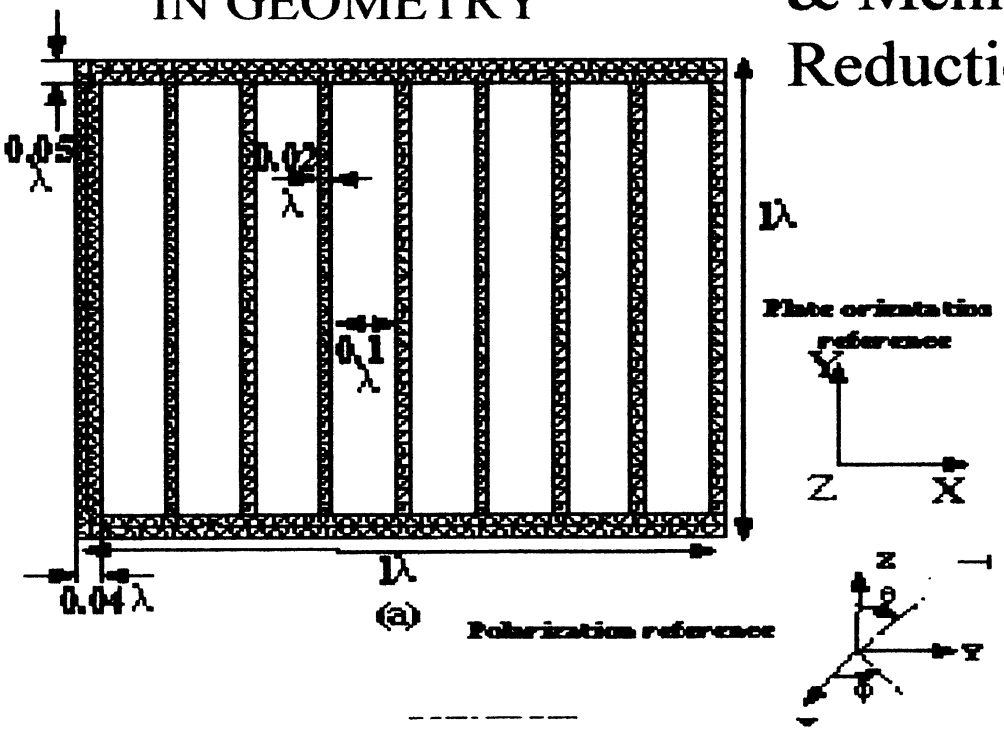

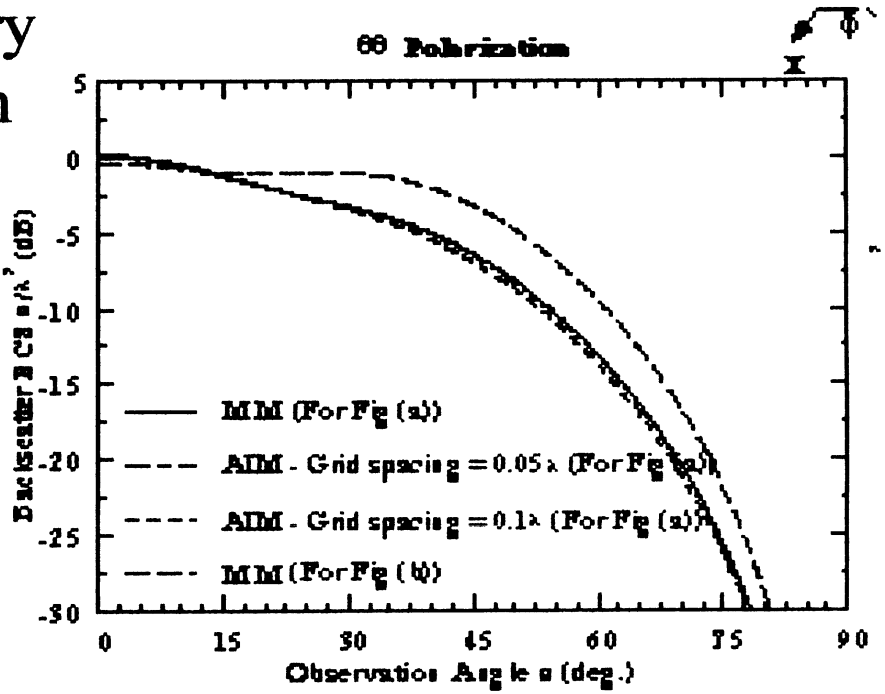

Demonstration Frequency Extrapolation

Performance of AWE for Shielded Structures

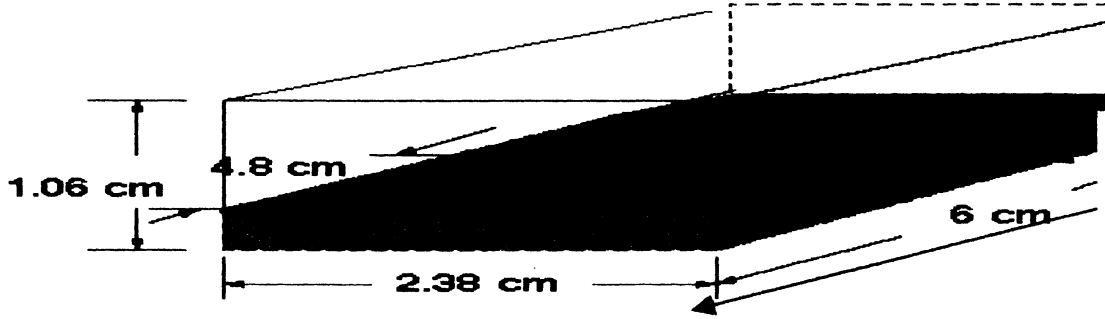

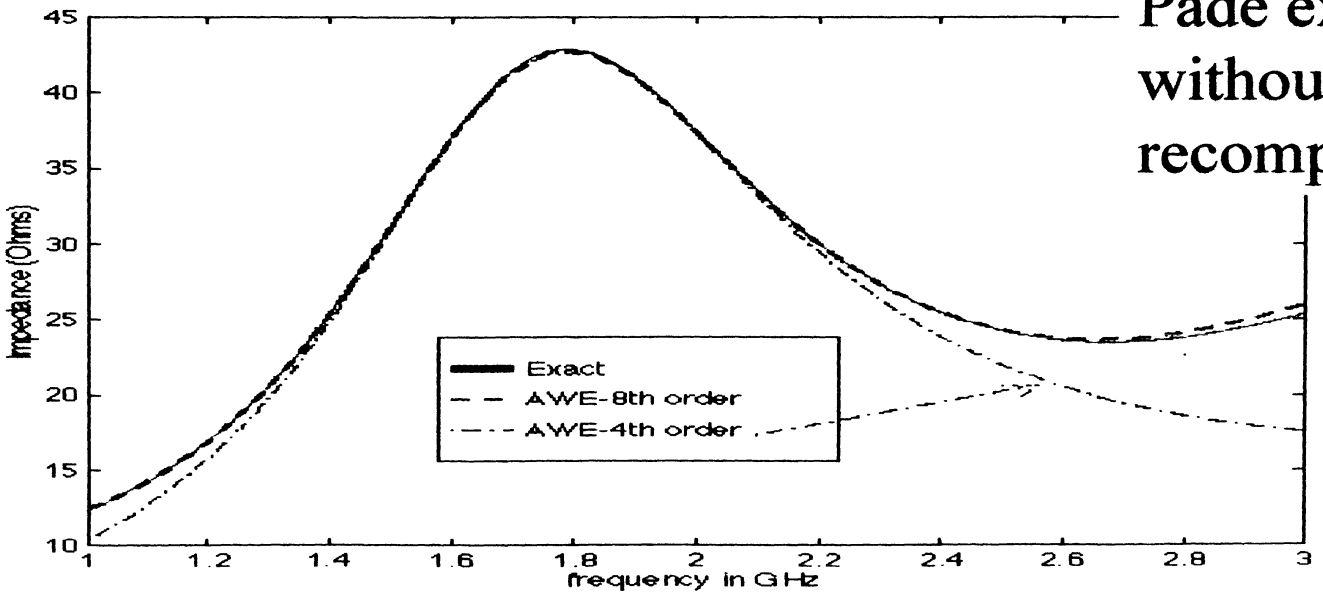

Computation done at 1.85 GHz and then extrapolated using Pade expansion without matrix recomputation

A PLANAR SLOT SPIRAL FOR MULTI-FUNCTION COMMUNICATIONS APERTURES

M.W. Nurnberger and J.L. Volakis

Radiation Laboratory
Dept. of Elect. Engin. & Comp. Sci.
University of Michigan, Ann Arbor, MI 48109-2122

ABSTRACT

A slot spiral antenna and its associated feed are presented for conformal mounting on a variety of land, air, and sea vehicles. By exploiting the inherent broadband behavior, good pattern coverage and polarization diversity of the spiral antenna, a conformal antenna which can be concurrently used for cellular, digital personal communications (PCS), global positioning (GPS) and intelligent vehicle highway systems (IVHS) as well as wireless LAN networks has been developed. A key requirement for achieving such broadband behavior (800-3000MHz) is the availability of a broadband planar feed and balun. Such a feed was proposed last year by the authors. However, additional design improvements were found to be necessary to achieve satisfactory pattern and gain performance. Among them were a broadband termination for the spiral arms and the suppression of cavity and waveguide modes. Both of these improvements played a critical role in achieving acceptable performance over the 800-3000 MHz bandwidth. After a general description of the slot spiral antenna and the above modifications, this paper presents a comparison of the performance before and after the modifications.

Keywords: Spiral Antennas, Planar, Conformal, Automotive, Antenna Measurements, Broadband, Circular Polarization

1.0 INTRODUCTION

Spiral antennas are particularly known for their ability to produce very wide-band, almost perfect circularly-polarized radiation over their full coverage region. Because of this polarization diversity and their inherent broad spatial and frequency coverage, a wide range of applications exist. These range from military surveillance, ECM, and ECCM to numerous commercial and private uses, including the consolidation of multiple low gain communications antennas on moving vehicles.

For the typical wire or microstrip spiral antenna, the performance advantages mentioned above come at the price of size and complexity. While the radiating elements of a wire spiral may be planar, the feed network and balun structures generally are not, and combine to add weight, depth, and significant complexity to the system. Furthermore, because the spiral antenna radiates bi-directionally, a broadband absorbing cavity is generally used to eliminate the radiation in one direction, adding even more depth to the antenna. While some designs exist [1] that integrate the feed and balun into the cavity and reduce the complexity somewhat, the absorbing cavity is still at least a quarter-wavelength deep at the lowest frequency of operation, adding significant thickness to the antenna [2].

A slot spiral is not burdened with most of these difficulties. As was demonstrated previously [3], the balun and feed structure may be integrated into the planar radiating structure. This greatly simplifies the construction and increases the accuracy of the antenna by allowing standard printed circuit techniques to be used throughout the entire fabrication process. Also, while the slot spiral also radiates bi-directionally, a deep, absorbing cavity is not necessary to force uni-directional radiation. In fact, for conformal mounting, a very shallow reflecting cavity is sufficient, and also serves to increase the gain somewhat.

Of particular interest in this paper is the design of a slot spiral antenna which occupies minimum real estate (small thickness and diameter) and operates at least up to 3 GHz. More specifically, we are interested in integrating the transmit/receive functions of the following systems

into a single aperture:

- Analog and Digital Cellular Telephone (825-950, 1700-1900 MHz)
- Global Positioning System (GPS) (1227.6 and 1575.42 MHz)
- Personal Communications System (PCS) (1850-2000 MHz)
- Intelligent Vehicle Highway System (IVHS)
- IEEE 802.11 Wireless LAN (2400-2500 MHz)

Hence, a minimum bandwidth of 3:1 is required to successfully integrate these functions. Although the earlier design could easily handle this bandwidth, to maintain a small antenna diameter (less than 6 inches), we found it necessary to develop both better spiral arm terminations and new cavity mode suppression techniques. In the following, we first present a description of the overall antenna and then proceed to discuss its performance after the aforementioned improvements.

2.0 SLOT SPIRAL DESIGN

The design procedure for the slot spiral antenna assembly is somewhat long and involved, and requires the careful choice of many inter-related design parameters. In this section we summarize the concerns in the design of the slot spiral, and discuss the more important design parameters. The design parameters are: spiral growth rate, α; number of turns, N; microstrip line characteristic impedance(s), Z_{M_*}; slot line characteristic impedance(s), Z_{S_*}; substrate characteristics: ϵ_r, $\tan\delta$, and metalization technique; thickness of the substrate, t; length and impedance of the tuning stub, l_{Stub} & Z_{Stub}; cavity depth, h; cavity wall material; slot line termination material and technique; and the specific geometry of the microstrip-slot line transition.

As with most antennas, the design procedure of the slot spiral is an iterative one. However, because the individual parameters are highly dependent on each other, the design procedure is particularly involved. It is perhaps easiest initially to choose the growth rate, and then to carefully inspect the initial design for inconsistencies. For the following discussion, the reader is referred to Figures 1 – 4 for clarification.

Physically, the crucial section of the antenna is a single printed circular substrate whose top and bottom views are displayed in Figures 1 and 2. On one side of the 20 mil substrate (see Figure 1) is etched the slot spiral radiating element. The other side (see Figure 2) of the substrate incorporates the infinite balun microstrip feed. This conductor operates as a microstrip transmission line using the other side as a ground plane, i.e. the planar conductor forming the slot spiral. As seen, the microstrip line spirals without interfering with the slot radiation to the center of the antenna. At the center, the microstrip is allowed to cross the slot spiral and is either extended approximately a quarter wavelength beyond the feed point or is brought through the substrate with a via, where it is shorted to the opposite side of the slot. When no ground plane is employed, the antenna radiates bi-directionally, with symmetric patterns on both sides. A ground plane is necessary in practice for conformal mounting on vehicles (airframe skin, car roof, boat skin etc.) to serve both as a shield and, more importantly, to eliminate the need for absorber backing. The cavity can also be used to improve the gain by as much as 3 dB.

Because of the slot operation, the slot spiral radiation can be interpreted in terms of equivalent magnetic currents whose radiation is enhanced with the presence of a ground plane in the immediate proximity of the slot. Thus, a ground plane or cavity (see Figure 3) in conjunction with a slot spiral allows for very thin antenna designs. In addition, it provides shielding and nearly doubles the gain over a very wide bandwidth (larger than that of the antenna). We should remark that the side or vertical walls of such cavities are typically terminated with some absorbing material to suppress cavity resonances, but as found in our investigation, additional cavity treatment may be necessary to realize the broadband antenna characteristics. Moreover, as noted above, the slot arms should be terminated properly to suppress the traveling wave reflections which interfere both with the polarization purity of the antenna and its bandwidth. Without any loading, it would be necessary to resort to a much larger antenna size which is, of course, highly undesirable for the intended commercial uses of the antenna.

Having discussed the overall antenna geometry and its crucial parameters, we now proceed with the specifics of the design. In the past [3] we presented a design of the slot spiral and the infinite balun microstrip feed. However, it was later found that additional modifications were necessary, including a new slot arm termination and cavity and waveguide mode suppression. Simulation and measured results displaying the characteristics of the antenna after the implementation of the tapered resistive slot termination are shown later. Also, we discuss the importance of the cavity design for proper antenna operation over the entire bandwidth.

Let us first review the basic slot spiral and feed de-

sign. In the 500 MHz to 4 GHz region, we found that a growth rate of 110.9 mils/rad to be a good initial choice. The initial characteristic impedance of the microstrip line was chosen to be 50Ω. As can be realized from the above antenna description, the actual feed is contrived through the use of a microstrip to slot line transition. Here, the microstrip line views the slotline as a pair of shunt branches. Thus, for the transition to operate most effectively, the characteristic impedance of the microstrip line is chosen to be half that of the slot line, yielding a perfect match at the feed. Based on the dielectric constant and thickness of the substrate, and on fabrication concerns, a certain range of slot line impedances will be available. For a dielectric constant of 3.38 and a thickness of 20 mils, a 110Ω slot line, which has a width of approximately 35 mils, was used. This required a microstrip characteristic impedance of 55Ω at the transition, and yielded a microstrip ground plane width of approximately 313 mils.

As the microstrip feed spirals to the slot spiral center, of concern is the coupling between the microstrip feed line and the slotline, the latter being the primary radiator. Any coupling from the microstrip feed to the slotline will have adverse effects on the pattern shape and polarization purity of the antenna. To minimize coupling, it is best to maximize the ratio of microstrip line to ground plane width. Many design issues can be traded off in this case – the most important being the growth rate, substrate thickness and dielectric constant, slotline impedance and the microstrip line characteristics. In our design approach, we first chose to modify just the microstrip line width, and adjust the others if necessary later. To increase the width ratio mentioned above, the impedance of the intermediate microstrip line was increased until the width ratio was approximately doubled. We also employed Klopfenstein tapers [4] in both cases to transition from the 50Ω outer feed impedance to the 70Ω intermediate microstrip impedance, and then back to the 55Ω microstrip line impedance at the center of the spiral. In this manner, the impedance changes do not hinder the broadband behavior of the antenna and feed, thus maintaining the slot spiral's broadband behavior.

3.0 SLOT SPIRAL RESISTIVE TERMINATION

Several measurements of the original 6 inch diameter and 0.2 inch thick (with ground plane) spiral antenna were collected at the NASA Langley facilities. The antenna was tested in isolation, and a 1/4-scale version was also tested on the roof of a 1/4-scale minivan, with the goal of assessing its bandwidth, pattern coverage, CP purity, gain and efficiency. Specifically, measurements were performed from 500 MHz to 5 GHz, with a representative pattern given in Figure 5. We show the pattern of the antenna in the middle of the roof of the minivan at the full scale frequency of 1350 MHz, obtained with a spinning linear source. Thus, the rapid oscillations observed in the pattern are a measure of the axial ratio of the antenna at this frequency. In this case, zero degrees refers to radiation normal to the spiral, and 90 degrees corresponds to radiation in the plane of the antenna. As expected, the antenna gain is maximum along the broadside and drops somewhat in the plane of the antenna. At 70 degrees, the gain is down approximately 5 dB, and at 80 degrees, about 10 dB. The axial ratio is also expected to worsen (higher oscillations are associated with worse axial ratio) at large angles from normal but for this frequency, the axial ratio needs improvement even at broadside (zero degrees). This is true for the patterns of the isolated antenna (not shown) and for the antenna mounted in the middle of the minivan's roof. Actually, towards the lower frequencies, the antenna's overall performance deteriorates substantially. This deterioration was traced to traveling wave reflections from the slot spiral arm termination. To maintain the same antenna size while minimizing these reflections and improving its low-frequency performance, it was necessary to apply some type of tapered absorber termination over the ends of the spiral.

Initially, tapered applications of foam and ferrite-loaded rubber absorbers were used, but these techniques, although they demonstrated the importance of the termination, did not lead to a repeatable design for manufacturing purposes. Instead, we developed a technique using resistive paint applied in a tapered fashion over the slots. The compactness of the resistive paint was found to be very attractive, and the overall shape and thickness of the termination was also consistently reproducible in manufacturing. To verify the design of the resistive paint termination, the commercial simulation package IE3D was employed, permitting the modeling of the substrate, cavity and the entire spiral configuration, including the resistive paint in the slots, via the moment method. A display of the geometry used by IE3D is shown in Figure 4 and includes the microstrip feed, the conductors forming the slot spiral, and the resistive termination of the slots. As is the case with most moment method codes, the conductors are broken into triangular elements and a current expansion is introduced over all elements. The latter are found by enforcing the integral equation with the multi-layer substrate Green's function on all conductor segments to form a linear system of equations.

Samples of the simulation results for the antenna using the resistive taper are shown in Figures 6 and 7, and correspond to frequencies of 800 MHz and 3 GHz. Calculations

were also performed at many intermediate frequencies, but aren't shown here. In Figures 6 and 7 we display the left and right circularly polarized patterns for two orthogonal cuts of the antenna ($\phi = 0$ and $\phi = 90$). As usual, the elevation angle is θ, and $\theta = 0$ refers to broadside radiation. Three patterns are included in each figure: the first refers to operation of the isolated antenna with no cavity and without the resistive termination; the second pattern refers to the antenna after the resistive taper has been applied, but still with no cavity. The third pattern is for the final antenna configuration, which includes both the resistive termination as well as the cavity.

It is clear from the patterns in Figures 6 and 7 that at cellular frequencies, the antenna is nearly useless without the use of the resistive termination (bad axial ratio, non-uniform radiation, etc.). However, when the termination is applied, the expected performance of the slot spiral is recovered with a gain of nearly 5 dB_{ic} at broadside and nearly 20 dB of polarization isolation. The calculated antenna efficiency in this case is slightly larger than 70%. When the cavity is introduced, the pattern shape in general is maintained, but the effects on the polarization purity are dependent on frequency, as might be expected. The efficiency also drops substantially. These difficulties are due to cavity and waveguide mode excitations which can in part be suppressed by introducing absorber at the cavity walls. However, these absorbers create other problems of their own, not to mention a certain loss of efficiency. Alternatively, other approaches can be employed to suppress the cavity modes while minimizing losses in efficiency. Because of space limitations, these remedies will be discussed at the conference. As seen from the patterns in Figure 7, at higher frequencies, while the axial ratio performance is quite good, pattern symmetry and coverage still are negatively effected by the cavity, as is the efficiency.

4.0 CONCLUSIONS

In this paper we presented a design for a slot spiral antenna which has the bandwidth and pattern coverage necessary to integrate cellular, GPS, PCS, and wireless lan system functionality into a single aperture. The key features of this antenna are its small thickness (less than 0.2 inches) and small diameter (less than 6 inches), thus permitting conformal and inconspicuous mounting on mobile platforms. At the same time it integrates several communication and navigation systems into a single platform, thus reducing the overall cost of the integrated system while maintaining versatility.

The proposed antenna achieves its small thickness by using an innovative design which incorporates a planar infinite balun whose bandwidth is maintained over the entire antenna operation. It also incorporates novel tapered resistive arm terminations and cavity mode suppression schemes to allow the realization of the full potential of the antenna. The effectiveness of the resistive taper and the overall operation of the antenna was verified with a CAD simulator based on the method of moments, and measurements were collected at specific frequencies. Some measurements were also collected with a 1/4-scale antenna mounted on the roof of a 1/4-scale minivan. In all cases, the resistive arm termination proved essential to the proper operation of the antenna, particularly at lower frequencies. Cavity mode suppression was also viewed as essential. Together, these remedies should permit the effective use of slot spiral antennas which, in spite of their attractiveness, have so far been of limited usefulness.

ACKNOWLEDGMENTS

The authors would like to thank Fred Beck and Dion Fralick for their support on the project, Mr. Robert Holt, Mr. Carl A. Lipp, and Mr. Hunter Walden for performing the measurements on the slot spiral antenna, and deeply appreciate the donation of the RO4003 substrate by the Rogers Corp.

REFERENCES

1. R. Bawer, J. J. Wolfe, "A Printed Circuit Balun for Use with Spiral Antennas," *IEEE Trans. Microwave Theory Tech.*, Vol. MTT-8, May 1960, pp. 319-325.

2. R.G. Corzine, J.A. Mosko,"Four-Arm Spiral Antennas," Artech House, 1990 .

3. M.W. Nurnberger, J.L. Volakis, "A New Planar Feed for Slot Spiral Antennas," *IEEE Trans. Antennas Propagat.*, Vol. AP-44, Jan 1996, pp. 130-131.

4. R.W. Klopfenstein, "A Transmission Line Taper of Improved Design," *Proc. IEEE*, Jan 1956, pp. 31-35.

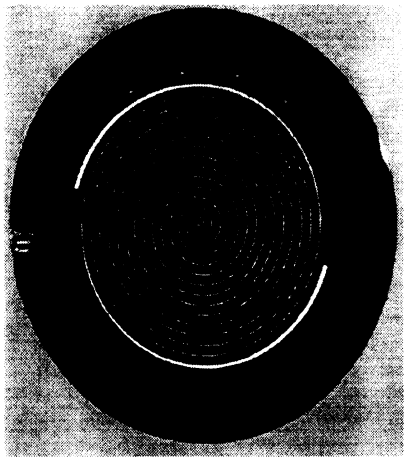

Figure 1: Underside of Slot Spiral Antenna, showing slot radiator.

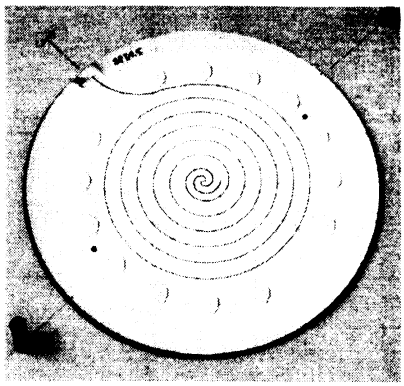

Figure 2: Top view of Slot Spiral Antenna, showing infinite balun microstrip feed.

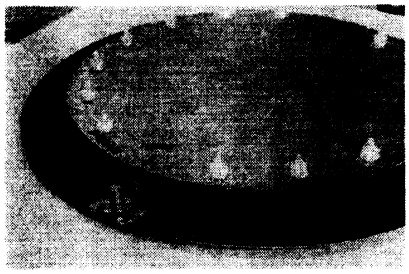

Figure 3: Bottom view of Slot Spiral Antenna, showing absorber walls and reflecting cavity bottom.

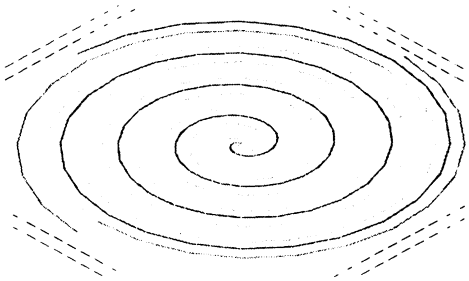

Figure 4: Geometrical model of antenna for numerical analysis.

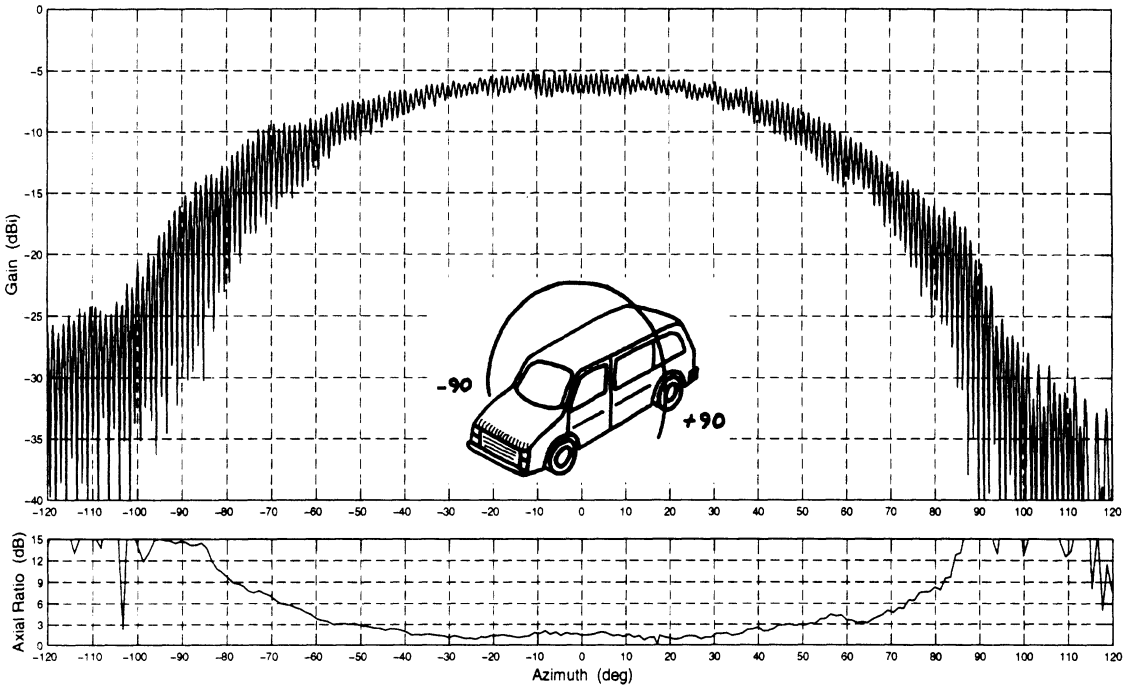

Figure 5: Spinning linear plot of spiral antenna on the roof of a minivan, showing poor axial ratio.

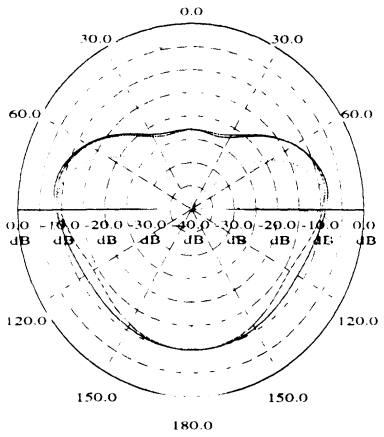

(a) Pattern w/o termination or cavity.

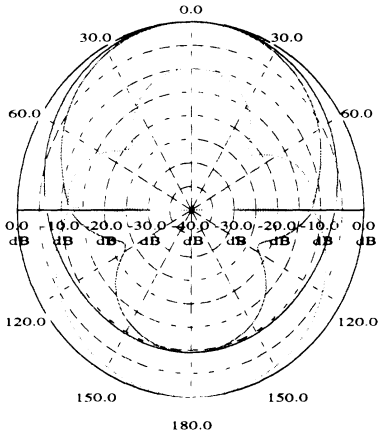

(b) Pattern with resistive termination.

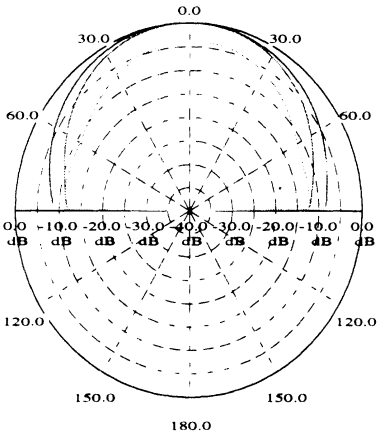

(c) Pattern with resistive termination and cavity.

E-right, phi=0. (deg)
E-left, phi=0. (deg)

Figure 6: Calculated antenna patterns at 800 MHz.

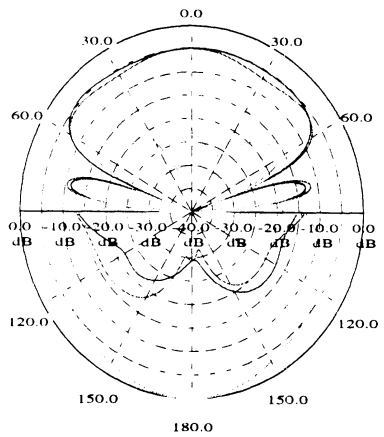

(a) Pattern w/o termination or cavity.

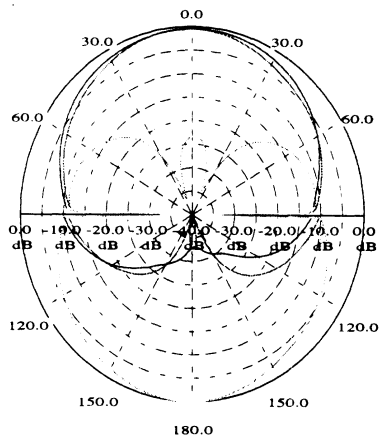

(b) Pattern with resistive termination.

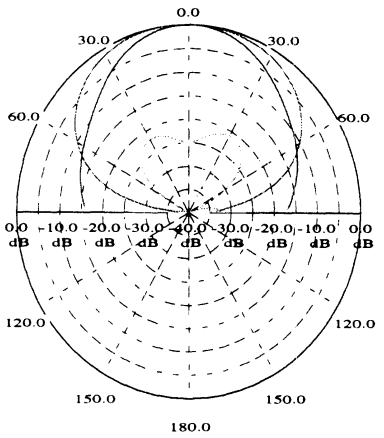

(c) Pattern with resistive termination and cavity.

E-right, phi=90. (deg)
E-left, phi=90. (deg)

Figure 7: Calculated antenna patterns at 3000 MHz.

A THIN CAVITY-BACKED ARCHIMEDEAN SLOT SPIRAL FOR 800-3000 MHZ BAND COVERAGE

Tayfun Özdemir*, Michael W. Nurnberger and John L. Volakis
Radiation Laboratory, Department of Electrical Engineering and Computer Science, University of Michigan, Ann Arbor, Michigan 48109-2122
tayfun@umich.edu, mwnurnbe@umich.edu, volakis@umich.edu

Introduction

Wide band properties and circular polarization characteristics of spiral antennas make them quite attractive for mobile and modern telecommunication systems. However, their deployment on conformal metallic platforms has been impeded by adverse effects from the ground plane or the cavity. Many studies have been carried out to investigate ways of successfully incorporating ground planes into the spiral design. Nakano et. al. [1] and Wang, et. al. [2], to name a few, showed that metal backing is compatible with the spiral modes through their studies of mostly wire and printed spirals.

In this study, we show that cavity-backed slot spirals (rather than printed) are particularly attractive for conformal applications. Since slot radiation is enhanced by the presence of a shallow metal-backed cavity, very thin (less than a $\frac{1}{4}$" thick) antennas can be constructed without compromising the spiral's broadband performance.

A specific design proposed in [3] is considered below for analysis and improvement.

Design

Figure 1 shows the geometry of the cavity-backed spiral. The spiral is desired to have a gain of at least 3dB with less than 2dB axial ratio from 800 to 3000 MHz [3]. Slot radiating elements have been chosen because they tolerate very thin reflecting cavities, which produce a unidirectional pattern and a 3dB increase in gain. The cavity depth was set at 0.635cm thus varying from $\lambda/59$ to $\lambda/16$ over the operational band. This thickness is, of course, much thinner than typical absorbing cavities. The antenna is fed with a microstrip feed with an integrated balun [4], which is planar and easy to build. The slot termination is important in achieving circular polarization (low axial ratio) and a resistive thin-film termination was developed to allow arbitrary taper functions for optimum matching. The size of the antenna determines the low frequency performance and the number of turns is chosen such that the outer circumference is larger than the largest operational wavelength.

Finite element analysis with mixed-elements

To analyze the complex spiral geometry and its cavity, the field is formulated via the Finite Element Method (FEM) in conjunction with edge-based elements [5]. The Boundary Integral (BI) technique has been used to terminate the mesh at the cavity aperture. The implementation for the BI follow closely that in [6]. The uniqueness of our analysis approach lies more with the meshing than the implementation of the field solution. A mix of hexahedra and prisms [5] were used to model the volume resulting in a combination of quadrilaterals and triangles on the aperture. This permitted an accurate and physical modeling of the aperture (which is perforated with the thin slot spiral) without resorting to oversampling. The particular mesh shown in Figure 2(a) results in a total of 1307 unknowns, a rather small size. One drawback is the elongated elements in the slot which worsen the condition number of the system matrix. Nevertheless, no difficulty was encountered in achieving tolerances of less than one percent using a biconjugate gradient solver.

In the simulations given next, the antenna was excited by placing a current source across the slot at the center of the antenna. The input impedance was then obtained by dividing the computed voltage (across the slot) at the feed location by the amplitude of the excitation current. Also, the resistive film taper was modeled with equally spaced equivalent lumped resistors whose values were chosen to dissipate an equal amount of energy.

Antenna performance

First, we comment on the fundamental operations of the slot spiral. Figure 2(b) shows the computed variation of the voltage (magnetic current) along the spiral arms. The real and imaginary parts are 90 degrees out of phase indicating a traveling wave (also implying that the resistive termination eliminates reflections from the spiral ends and this is necessary for low axial ratio). Further, the separation of the wave crests is one free-space wavelength indicating a pure TEM wave. Basically the fields tightly couple to the narrow slot and the propagation constant is not altered by the presence of the ground plane. However, the ground plane is responsible for the voltage lobes toward the spiral ends, a feature also present with printed spirals [1]. Note that, at 1900MHz, the voltage distribution is approximately the same as that of a center-fed 1λ linear dipole.

Next, let us look at the broadband behavior of the antenna. The results in Figure 3 show that the bandwidth increases as more turns are added or the expansion ratio is increased. The low frequency gain improves while the axial ratio remains at acceptable levels. Results also show that increasing the expansion ratio a is slightly better than adding more turns (same expansion of the antenna size) in terms of gain performance. The decrease in gain toward the low end of the frequency band is due to the resistive termination of the spiral. As the frequency drops, the radiating slots move toward the rim of the spiral and thus more of the energy is dissipated in resistive termination. Since

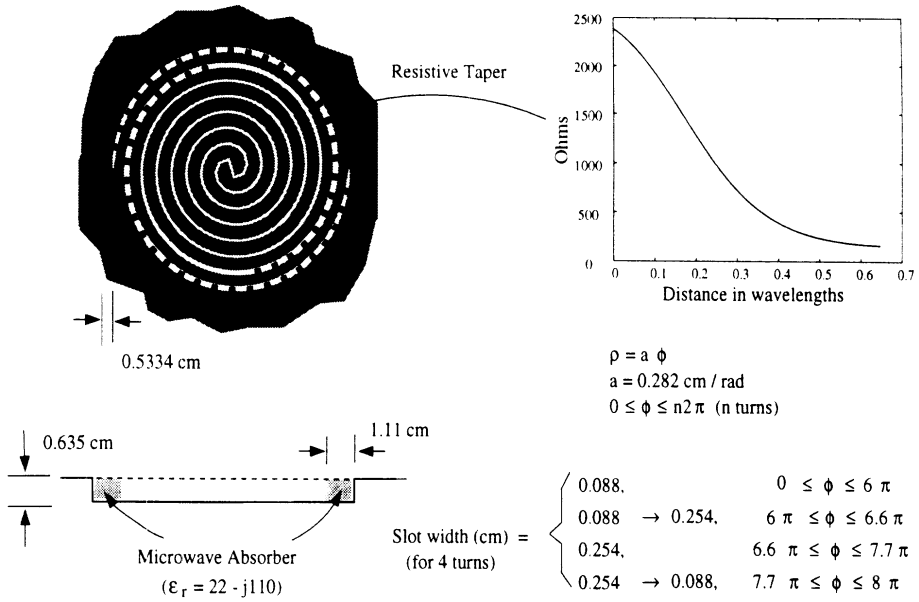

Figure 1: (a) Cavity-backed Archimedean slot spiral.

the resistive termination is essential for low axial ratio, this calls for a compromise between the gain and the pattern. Figure 3(b) shows that the axial ratio can be maintained less than 2dB using the resistive termination but achieving gain above zero dB requires increase in diameter to about 20cm. Note that in all simulations, the cavity thickness was not altered and the microwave absorbing ring was placed at a radial distance of 1.2cm from the slot radiator. Bringing it closer increased the overall gain but deteriorated the axial ratio.

References

[1] H. Nakano, K. Nogami, S. Arai, H. Mimaki, and J. Yamauchi, "A spiral antenna backed by a conducting plane reflector," *IEEE Trans. Antenna Propagat.*, vol. 34, no. 6, pp. 791-796, June 1986.

[2] J. J. H. Wang and V. K. Tripp, "Design of multioctave spiral-mode microstrip antennas," *IEEE Trans. Antenna Propagat.*, Vol. 39, No. 3, pp. 332-335, March 1991.

[3] M. W. Nurnberger and J. L. Volakis, "A planar slot spiral for mobile communications," *19th Meeting and Symposium of Antenna Measurement Techniques Association*, Boston, Massachusetts, November 17-21, 1997.

[4] M. W. Nurnberger and J. L. Volakis, "A new planar feed for slot spiral antennas," *IEEE Trans. Antenna Propagat.*, vol.44, no.1, pp. 130-131, Jan. 1996.

[5] T. Özdemir and J. L. Volakis, "Triangular prisms for edge-based vector finite element analysis of conformal antennas," *IEEE Trans. Antenna Propagat.*, vol. 45, no. 5, pp.788-797, May 1997.

[6] J. L. Volakis, T. Özdemir and J. Gong, "Hybrid finite-element methodologies for antennas and scattering," *IEEE Trans. Antenna Propagat.*, vol.45, no.3, pp. 493-507, March 1997.

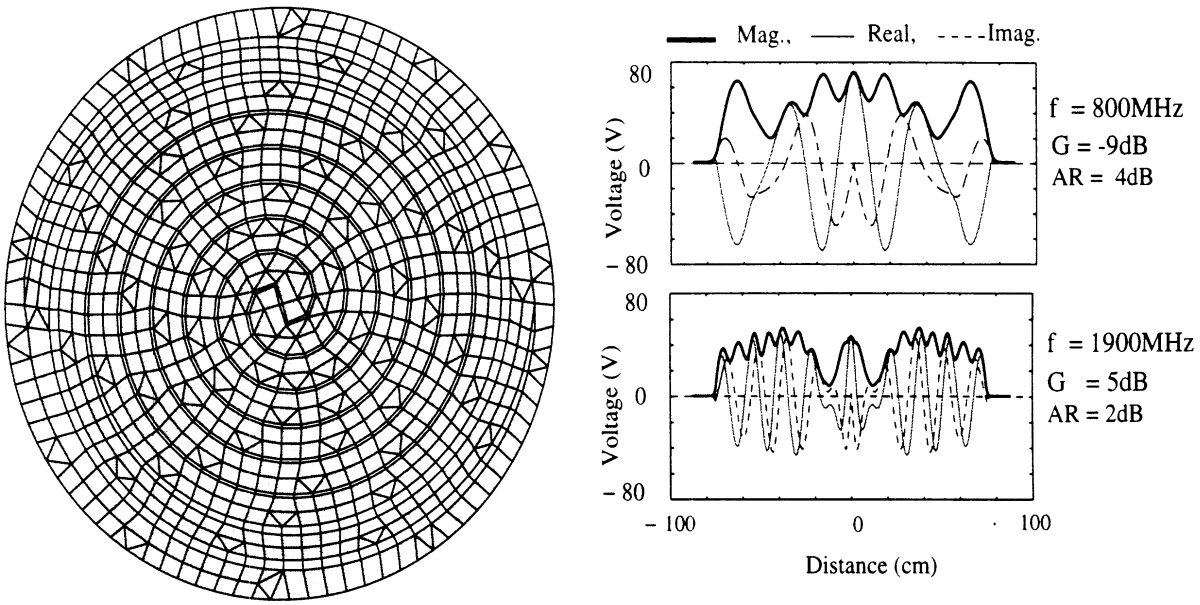

(a) (b)

Figure 2: (a) Surface mesh comprised of quadrilateral and triangular patches, (b) Voltage along the spiral arms for 800 and 1900 MHz.

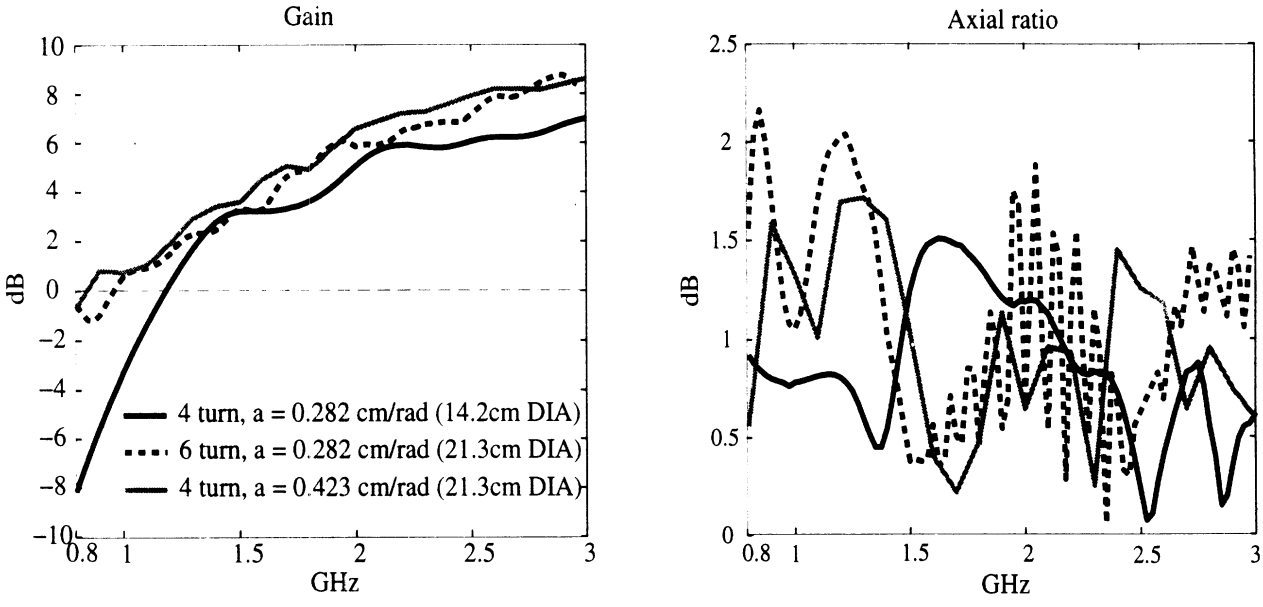

(a) (b)

Figure 3: Slot spiral performance as a function of expansion ratio a and number of turns: (a) Gain, (b) axial ratio.

Hybrid Finite Element Methodologies for Antennas and Scattering

J. L. Volakis, T. Özdemir and J. Gong

Radiation Laboratory
Department of Electrical Engineering and Computer Science
University of Michigan
Ann Arbor, Michigan 48109-2122

Abstract

This paper is an overview of the finite element method (FEM) as applied to electromagnetic scattering and radiation problems. A brief review of the methodology is given with particular emphasis on new developments over the past five years relating to feed modeling, parallelization and mesh truncation. New applications which illustrate the method's capabilities, versatility and utility for general purpose application are discussed.

1 Introduction

Over the past 10 years we have witnessed an increasing reliance on computational methods for the characterization of electromagnetic problems. Although traditional integral equation methods continue to be used for many applications, one can safely state that in recent years the greatest progress in computational electromagnetics has been in the development and application of partial differential equation(PDE) methods such as the finite difference-time domain and finite element (FEM) methods, including hybridizations of these with integral equation and high frequency techniques. The major reasons for the increasing reliance on PDE methods stem from their inherent geometrical adaptability, low O(N) memory demand and their capability to model heterogeneous (isotropic or anisotropic) geometries. These attributes are essential in developing general-purpose analysis/design codes for electromagnetic scattering, antennas, microwave circuits and biomedical applications. For example, modern aircraft geometries contain large nonmetallic or composite material sections and antenna geometries may involve many layers of materials, including complex microwave circuit feeding networks. Although, the moment method continues to remain the most accurate and efficient approach for subwavelength size bodies of simple geometries, PDE methods and hybrid versions of these

have shown a much greater promise for large scale simulations without placing restrictions on the geometry and material composition of the structure.

This paper is a selected review of hybrid finite element methods and their applications to scattering and antenna analysis. We begin by first introducing the mathematical basics of the method without reference to a specific applications and in a manner that identifies the method's inherent advantages in handling arbitrary geometrical configurations which may incorporate impedance boundary conditions and anisotropic materials. In this section we also identify the key challenges associated with the implementation of the method such as mesh truncation and feed modeling for antenna applications. Section 3 of the paper reviews the various mesh truncation schemes to be employed on the outer mesh surface for the unique solution of the vector wave equation. Absorbing boundary conditions, integral equations and artificial absorbers are discussed, all leading to different versions of hybrid FEM methodologies, and we comment on their accuracy and ease of implementation. Section 4 presents several approaches for antenna feed modeling in the context of the FEM, including coaxial as well as aperture coupled feeds. The next section is devoted to parallelization issues specific to finite element codes. We give performances of typical FEM codes and provide storage and implementation guidelines for maximizing code performance on parallel computing platforms. The final section of the paper gives some representative applications of the method to scattering and antenna problems.

2 Theory

2.1 FEM Formulation

Consider the antenna and scattering configurations shown in Figure 1. In the case of a scatterer, the entire computational domain is enclosed by a fictitious surface S_o that may encompass a variety of composite/dielectric volumes as well as metallic, impedance and resistive surfaces. The antenna geometry is assumed to be recessed in some doubly curved surface. In this case, the bounding surface S_o may either be located as shown or can be coincident with the antenna aperture. As usual, the recessed cavity is intended to house the radiating elements and their feeding structure such as coaxial cables, striplines, microstrip lines or aperture coupled feeds. The cavity may encompass any inhomogeneous or anisotropic material including resistive cards, lumped or distributed loads and so on.

The goal with any finite element formulation is to obtain the solution of the vector wave equation

$$\nabla \times \left[\overline{\overline{\mu}}_r \cdot (\nabla \times \mathbf{E})\right] - k_o^2 \overline{\overline{\epsilon}}_r \cdot \mathbf{E} = -jk_o Z_o \mathbf{J}_i - \nabla \times (\overline{\overline{\mu}}_r^{-1} \cdot \mathbf{M}_i) \qquad (1)$$

in which $\mathbf{E}$ represents the total electric field, $(\overline{\overline{\epsilon}}_r, \overline{\overline{\mu}}_r)$ denote the relative permittivity and permeability tensors of the computational domain, k_0 is the free space wavenumber and Z_0 is the free space intrinsic impedance. In addition, $\mathbf{J}_i$ and $\mathbf{M}_i$ denote the impressed electric and magnetic sources, respectively, and represent the excitation for the antenna problem. As is well known, the standard finite element (FE) solution scheme is to

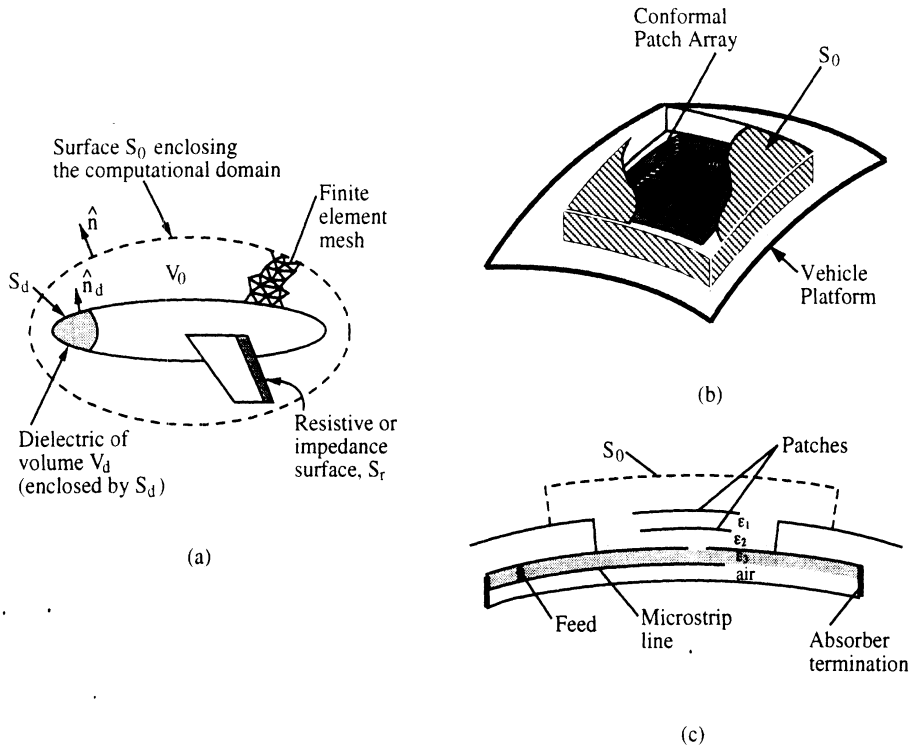

Figure 1: Computational domains for FEM analysis, (a) the various regions enclosed by S_0, (b) typical tetrahedral mesh, (c) computational regions for antenna analysis

consider the weak form of (1), instead of solving it directly. This can be achieved by extremizing the pertinent functional [1]

$$\begin{aligned} F(\mathbf{E}) &= \frac{1}{2}\iiint_{V_0}\left\{(\nabla\times\mathbf{E})\cdot[\bar{\bar{\mu}}_r^{-1}\cdot(\nabla\times\mathbf{E})]-k_0^2(\bar{\bar{\epsilon}}_r\cdot\mathbf{E})\cdot\mathbf{E}\right\}dv \\ &+ \iiint_{V_s}\mathbf{E}\cdot\left[jk_0Z_0\mathbf{J}_i+\nabla\times\left(\bar{\bar{\mu}}_r^{-1}\cdot\mathbf{M}_i\right)\right]dv \\ &+ jk_0Z_0\iint_{S_0+S_f}\mathbf{E}\cdot(\mathbf{H}\times\hat{n})\,ds \\ &+ \frac{1}{2}jk_0Z_0\left\{\iint_{S_r}\frac{1}{R}(\hat{n}\times\mathbf{E})\cdot(\hat{n}\times\mathbf{E})\,ds+\frac{d}{Z_Ls}\iiint_{V_l}\mathbf{E}\cdot\mathbf{E}\,dV\right\} \end{aligned} \tag{2}$$

where R denotes the resistivity or impedance of the surface S_r, S_f stands for the junction opening to possible guided feeding structures and $\mathbf{H}$ is the corresponding magnetic field on S_0 and S_f whose outer normal is given by $\hat{n}$. Also, V_s is the source volume and V_l is the volume occupied by the load Z_L, whose length and cross section are given by d and s, respectively. It is noted that S_r must be closed when it satisfies an opaque impedance boundary condition but can be open (i.e. a finite plate) if it satisfies the penetrable resistive sheet condition [2]

$$\hat{n}\times\hat{n}\times\mathbf{E}=-R\hat{n}\times(\mathbf{H}^+-\mathbf{H}^-)$$

where $\mathbf{H}^{\pm}$ denote the fields on the two sides of the surface S_r. As seen from (2), in spite of the discontinuity in the magnetic field, no special care is required for the evaluation of

the integral over S_r. The explicit knowledge of $\mathbf{H}$ is, however, required over the surface S_0 and S_f (referred to as mesh truncation surfaces) for the unique solution of $\mathbf{E}$.

As an alternative to (2), we can instead begin with (1) by weighting it with a testing function $\mathbf{T}$. Subsequently, application of the divergence theorem yields the residual

$$\begin{aligned} <\mathbf{R},\mathbf{T}> &= \iiint_{V_o} \left\{(\nabla\times\mathbf{T})\cdot\left[\bar{\bar{\mu}}_r^{-1}\cdot(\nabla\times\mathbf{E})\right] - k_o^2\bar{\bar{\epsilon}}_r\cdot\mathbf{E}\cdot\mathbf{T}\right\} dV \\ &+ \iiint_{V_s} \mathbf{T}\cdot\left\{jk_oZ_o\mathbf{J}_i + \nabla\times(\bar{\bar{\mu}}_r^{-1}\cdot\mathbf{M}_i)\right\} dV \\ &+ jk_oZ_o\iint_{S_o+S_f}\mathbf{T}\cdot(\mathbf{H}\times\hat{n})dS \\ &+ jk_oZ_o\left\{\iint_{S_r}\frac{1}{R}(\hat{n}\times\mathbf{T})\cdot(\hat{n}\times\mathbf{E})dS + \frac{d}{Z_LS}\iiint_{V_l}\mathbf{T}\cdot\mathbf{E}dV\right\} \end{aligned} \quad (3)$$

This is typically referred to as the weak form of the wave equation, whereas (2) is referred to as the variational form. It will be seen later that when set equal to zero,(3) yields the same system of equations as those deduced from the functional (2). Therefore both methods are equivalent.

When dealing with large computational domains as is often the case in scattering applications, it is instructive to work with the scattered rather than the total field, and also distinguish the air and dielectric regions. This approach results in reduced errors within the computational domain and to proceed we introduce the definitions

$$\mathbf{E} = \mathbf{E}^{inc} + \mathbf{E}^{scat}, \mathbf{H} = \mathbf{H}^{inc} + \mathbf{H}^{scat} \quad (4)$$

where $\mathbf{E}^{inc}$ denotes the excitation field impinging from the exterior of S_o and $\mathbf{E}^{scat}$ is the scattered field. With these substitutions, the functional F takes the form

$$\begin{aligned} F(\mathbf{E}^{scat}) &= \frac{1}{2}\iiint_{V_o-V_d}\left\{(\nabla\times\mathbf{E}^{scat})\cdot(\nabla\times\mathbf{E}^{scat}) - k_0^2\mathbf{E}^{scat}\cdot\mathbf{E}^{scat}\right\} dV \\ &+ \iiint_{V_s}\mathbf{E}^{scat}\cdot\left[jk_0Z_0\mathbf{J}_i + \nabla\times\left(\bar{\bar{\mu}}_r^{-1}\cdot\mathbf{M}_i\right)\right] dV \\ &+ jk_0Z_0\iint_{S_0+S_f}\mathbf{E}^{scat}\cdot(\mathbf{H}\times\hat{n})\,dS \\ &+ \frac{1}{2}jk_0Z_0\left\{\iint_{S_r}\frac{1}{R}(\hat{n}\times\mathbf{E}^{scat})\cdot(\hat{n}\times\mathbf{E}^{scat})\,dS + \frac{d}{Z_LS}\iiint_{V_l}\mathbf{E}^{scat}\cdot\mathbf{E}^{scat}\,dV\right\} \\ &+ jk_0Z_0\left\{\iint_{S_r}\frac{1}{R}(\hat{n}\times\mathbf{E}^{scat})\cdot(\hat{n}\times\mathbf{E}^{inc})\,dS + \frac{d}{Z_LS}\iiint_{V_l}\mathbf{E}^{scat}\cdot\mathbf{E}^{inc}\,dV\right\} \\ &+ \frac{1}{2}\iiint_{V_d}\left\{\nabla\times\mathbf{E}^{scat}\cdot\left(\bar{\bar{\mu}}_r^{-1}\cdot\nabla\times\mathbf{E}^{inc}\right) - k_0^2\bar{\bar{\epsilon}}_r\cdot\mathbf{E}^{inc}\cdot\mathbf{E}^{scat}\right\} dV \quad (5) \\ &+ \frac{1}{2}\iiint_{V_d}\left\{\nabla\times\mathbf{E}^{inc}\cdot\left(\bar{\bar{\mu}}_r^{-1}\cdot\nabla\times\mathbf{E}^{scat}\right) - k_0^2\bar{\bar{\epsilon}}_r\cdot\mathbf{E}^{scat}\cdot\mathbf{E}^{inc}\right\} dV + f(\mathbf{E}^{inc}) \end{aligned}$$

in which $f(\mathbf{E}^{inc})$ is a collection of terms involving only the incident field $\mathbf{E}^{inc}$. Its specific form is of no consequence since it will be eliminated in the subsequent minimization of

F. Most importantly, we observe in (6) the presence of integrals over the volume V_d occupied by the dielectrics and over the surface S_r. The introduction of these integrals is required when working with the scattered field because $\mathbf{E}^{scat}$ is discontinuous at boundaries separating media with different permeabilities [4]. Also note that the presence of the last two integrals is necessitated because $\mathbf{E}^{inc}$ satisfies the wave equation only in free space, and that these two volume integrals become equal when the dielectric anisotropy reduces to isotropy.

The functionals (2) and (6) or the weighted residual (3) can be cast into a discrete system of equations for the solution of $\mathbf{E}$. To accomplish this, it is first necessary to subdivide the volume as a collection of small elements such as those shown in Figure 2 [3]. Within each volume element, the field can then be expanded as

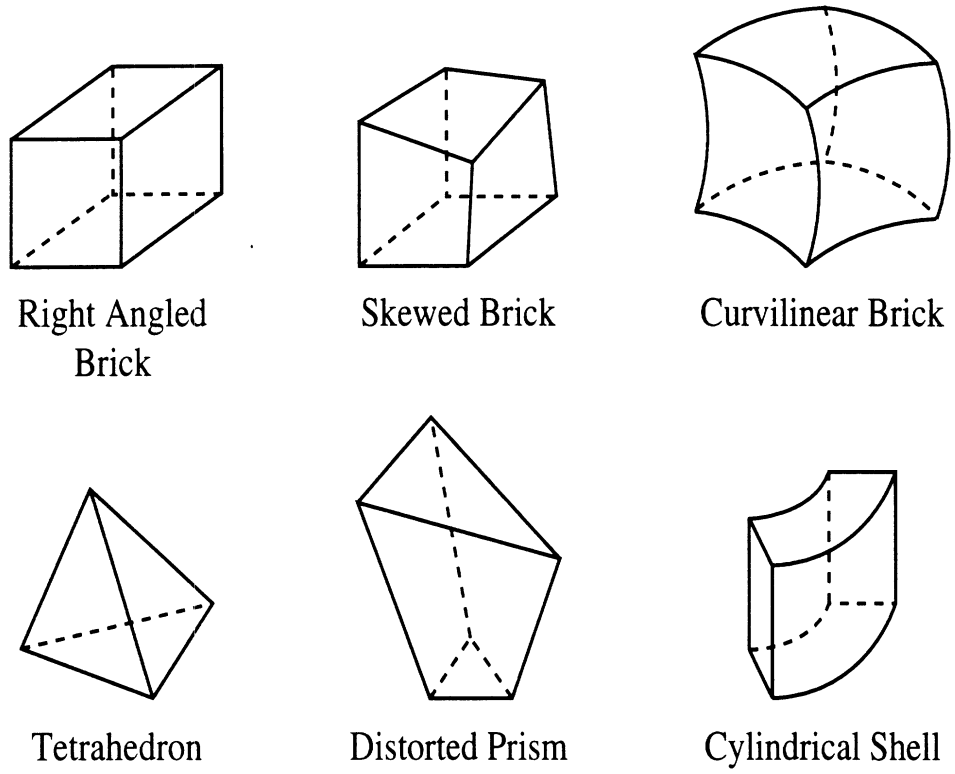

Figure 2: Illustration of the various elements for tessellating three dimensional volumes

$$\mathbf{E}^e = \sum_{k=1}^{M=\#of edges} E_k^e \mathbf{W}_k^e = [W^e]^T \{E^e\} \tag{6}$$

in which $\mathbf{W}_k^e$ are referred to as the edge-based shape or basis functions of the eth element in the computational domain. In contrast to the traditional node-based shape functions, the edge-based shape functions are better suited [5] for simulating three dimensional electromagnetic fields at corners and edges. Moreover, edge-based shape functions overcome difficulties associated with spurious resonances [6]. They were proposed by Whitney [7] over 35 years ago and were revived in the 1980s [8],[9]. Their representation is different for each element but have the common properties [10] of being divergence free (i.e.,

$\nabla \cdot \mathbf{W}_k = 0$ within the element) and normalized in such a manner so that the expansion coefficients E_k^e represent the average field value across the kth edge of the eth element. One disadvantage of the edge-based elements is that they increase the unknown count. However, this is balanced by the increased sparsity of the resulting stiffness matrix. A detailed mathematical presentation of the edge-based shape functions for various two and three dimensional elements (bricks, hexahedra and tetrahedra) [11]-[14] is given by Graglia *et. al.* [15] in this issue of the Transactions. Linear as well as higher order (curvilinear) elements are discussed [16]-[19].

2.2 Discretization and System Assembly

Once the computational domain has been tessellated using appropriate elements and shape functions, the discretization of (2), (3) or (6) proceeds by introducing the expansion $\mathbf{E}$ or $\mathbf{E}^{scat} = \sum_{e=1}^{N_e} \mathbf{E}^e$, with $\mathbf{E}^e$ as given by (6) and N_e denoting the number of elements comprising the computational domain. For the functional (2), the system of equations is constructed by setting (Rayleigh-Ritz procedure)

$$\frac{\partial F(\mathbf{E})}{\partial E_k^e} = 0, \qquad e = 1, 2, ..., N_e; \quad k = 1, 2, ..., M \tag{7}$$

whereas in the case of (3) Galerkin's approach is used by setting $\mathbf{T} = \mathbf{W}_k^e$. Regardless of the procedure, the resulting system will be of the form

$$\sum_{e=1}^{N_e} [A^e]\{E^e\} + \sum_{s=1}^{N_s} [B^s]\{E^s\} + \sum_{e=1}^{N_e} \{K^e\} + \sum_{p=1}^{N_p} \{C^p\} = 0 \tag{8}$$

in which the brackets denote square matrices and the curly braces refer to columns. Among the various new parameters, $[A^e]$ is referred to as the element matrix and results from the discretization of the first volume integral in (2),(3) or (6); N_s is equal to the aggregate of the surface elements (quadrilaterals for hexahedra or triangles for tetrahedra and prisms) used for the tessellation of S_o, S_f and S_r; the column $\{K^e\}$ results from the discretization of the source integral over V_s; and $[B^s]$ is the matrix associated with the third and fourth surface integrals in (2),(3) or (6). Finally, N_p denotes the aggregate of the surface and volume elements over S_r, V_ℓ and V_d and the column $\{C^p\}$ results from the discretization of the integrals in (6) involving the external incident field $\mathbf{E}^i$. Basically, $\{C^p\}$ provides the external excitations (scattering problem) whereas $\{K^e\}$ is the corresponding excitation column for internal sources as is the case with antenna problems.

The entries of the element matrix $[A^e]$ are specific to the choice of the shape functions and are compactly given by

$$[A^e] = \iiint_{V_e} \left\{ [DW^e][\overline{\overline{\mu}}_r]^{-1}[DW^e]^T - k_o^2 [W^e][\overline{\overline{\epsilon}}_r][W^e]^T \right\} dV \tag{9}$$

with

$$[DW^e]^T = \begin{bmatrix} \frac{\partial}{\partial y}\{W_z^e\}^T - \frac{\partial}{\partial z}\{W_y^e\}^T \\ \frac{\partial}{\partial z}\{W_x^e\}^T - \frac{\partial}{\partial x}\{W_z^e\}^T \\ \frac{\partial}{\partial x}\{W_y^e\}^T - \frac{\partial}{\partial y}\{W_x^e\}^T \end{bmatrix} \tag{10}$$

and V_e denotes the volume of the discrete element while the subscripts (x, y, z) in (10) imply the (x, y, z) components of the shape function $\mathbf{W}^e$. If lumped loads are present (i.e., in the presence of a volume integral over V_ℓ), the diagonal entries of $[A^e]$ are simply modified with the addition of the term $jk_oZ_od^2/Z_L$. Perfectly conducting posts located at the k^{th} edge are handled by setting the corresponding total fields equal to zero and rearranging the final matrix as discussed later.

The internal source excitation column is simply given by

$$\{K^e\} = \iiint_{V_e} [W^e] \left\{ jk_oZ_o \begin{Bmatrix} J_{ix} \\ J_{iy} \\ J_{iz} \end{Bmatrix} + \nabla \times \left([\overline{\overline{\mu}}_r]^{-1} \begin{Bmatrix} M_{ix} \\ M_{iy} \\ M_{iz} \end{Bmatrix} \right) \right\} dV \tag{11}$$

and the entries of the corresponding excitation column due to the incident field with the presence of dielectric materials are

$$\begin{aligned} \{C^p\} &= jk_oZ_o \iint_{S_r} \frac{1}{R}[W^p] \begin{Bmatrix} E_x \\ E_y \\ E_z \end{Bmatrix}^{inc} dS \\ &+ \frac{1}{2} \iiint_{V_d^p} \left\{ \left(\nabla \times \begin{Bmatrix} E_x \\ E_y \\ E_z \end{Bmatrix}^{inc} \right)^T [\overline{\overline{\mu}}_r]^{-1}[DW^p]^T - k_0^2[W^p][\overline{\overline{\epsilon}}_r] \begin{Bmatrix} E_x \\ E_y \\ E_z \end{Bmatrix}^{inc} \right\} dV \\ &+ \frac{1}{2} \iiint_{V_d^p} \left\{ [DW^p][\overline{\overline{\mu}}_r]^{-1} \left(\nabla \times \begin{Bmatrix} E_x \\ E_y \\ E_z \end{Bmatrix}^{inc} \right) - k_0^2 \left(\begin{Bmatrix} E_x \\ E_y \\ E_z \end{Bmatrix}^{inc} \right)^T [\overline{\overline{\epsilon}}_r][W^p]^T \right\} dV \end{aligned}$$

in which $\mathbf{W}^p$ implies the representation of the shape function over the required p^{th} surface or volume element.

The specification of the matrix $[B^s]$ can not be completed without first introducing some *a priori* relationship between the **E** and **H** fields on S_o. This relationship (or boundary condition on S_o) is referred to as the mesh termination condition and its form depends on the physics of the problem. For example, in the case of problems where the entire computational domain is enclosed by a perfect electric or magnetic conductor, the unknown column $\{E^s\}$ is eliminated from $\{E\}$. For scattering and radiation problems, the mesh termination condition should be such that the artificial boundary S_o appears transparent to all waves incident from the interior of the computational domain. Clearly, if S_o is placed far enough from the scatterer or radiator, the simple Sommerfeld radiation condition provides the appropriate relationship between **E** and **H**. However, this is not practical since it will yield large computational domains. To bring S_o as close as possible

to the scattering or radiating surface, more sophisticated boundary conditions must be introduced on S_o. These mesh termination conditions are critical to the accuracy and efficiency of the formulation and are some of the major bottlenecks in the implementation of the FEM. Regardless of the employed mesh termination approach, after carrying out the sums in (8), a process referred to as matrix assembly, the resulting matrix system will be of the general form

$$[\mathcal{A}] \begin{Bmatrix} \{E^V\} \\ \{E^B\} \end{Bmatrix} + \begin{bmatrix} [0] & [0] \\ [0] & [\mathcal{G}] \end{bmatrix} \begin{Bmatrix} \{E^V\} \\ \{E^B\} \end{Bmatrix} = \begin{Bmatrix} \{b^V\} \\ \{b^B\} \end{Bmatrix} \tag{12}$$

In this, $\{E^V\}$ denotes the field unknowns within the volume enclosed by $S_o + S_f$ whereas $\{E^B\}$ represents the corresponding unknowns on the boundaries S_o and/or S_f. The excitation column $\{b^V\}$ results from the assembly of $\{K^e\}$ and similarly $\{b^B\}$ is associated with $\{C^p\}$. The matrix $[\mathcal{A}]$ is very sparse (9 to 30 non-zero entries per row) and this is a major characteristic and advantage of FEM. By using special storage schemes and solvers suitable for sparse systems, the CPU and memory requirements are maintained at O(N) and scalability can be attained on multiprocessor platforms.

The boundary matrix $[\mathcal{G}]$ in (12) is associated with the boundary fields $\{E^B\}$ and its specific form is determined by the employed mesh termination condition on S_o. Over the past five years, much research on FEM has concentrated on the development of mesh truncation schemes which minimize the computational burden without compromising accuracy. As will be seen later, this compromise is difficult to attain and is subject to the computational problem being considered. For the purpose of our discussion, we will subdivide the various mesh termination schemes into three categories: (1) exact boundary conditions, (2) absorbing boundary conditions (or ABCs), and (3) artificial absorbers. Exact boundary conditions provide an integral relation between the electric and magnetic fields, and because they are exact, they permit the placement of S_o very near or exactly on the surface of the scatterer or radiator. The resulting formulation is referred to as the finite element-boundary integral (FE-BI) method and combines the adaptability of the FEM and the rigor of the boundary integral methods. However, it yields a fully populated matrix $[\mathcal{G}]$ and as a result, the FE-BI method is associated with higher computational demands even though only a small part of the overall system is full (see Figure 3a). To alleviate the higher computational demands of the rigorous FE-BI method, ABCs or artificial absorbers (AAs) can instead be used to terminate the mesh. Both of these are approximate mesh termination methods, but lead to completely sparse and scalable systems of equations. Basically, the sub-matrix $[\mathcal{G}]$ is eliminated with the application of ABCs or AAs (see Figure 3b). In the case of ABCs, a local boundary condition in the form of a differential equation is applied on S_o to relate $\mathbf{E}$ and $\mathbf{H}$ so that S_o appears as transparent as possible to the incident fields from the interior. The resulting method will be referred to as the finite element-ABC (FE-ABC) method and has so far been the primary method for general-purpose scattering computations. Finally, the use of artificial absorbers (including perfectly matched layers or PMLs) [20] have recently gained major attention because of their potential for greater accuracy and inherent implementation simplicity. In the context of the finite element-artificial absorber (FE-AA) method, the mesh is terminated by using a material absorber (typically non-realizable

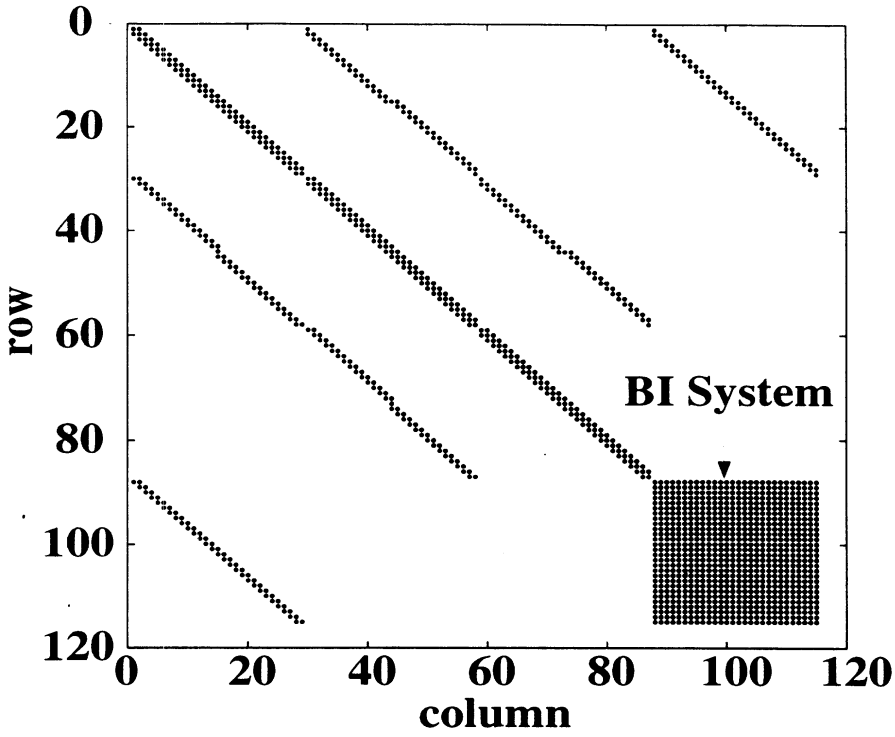

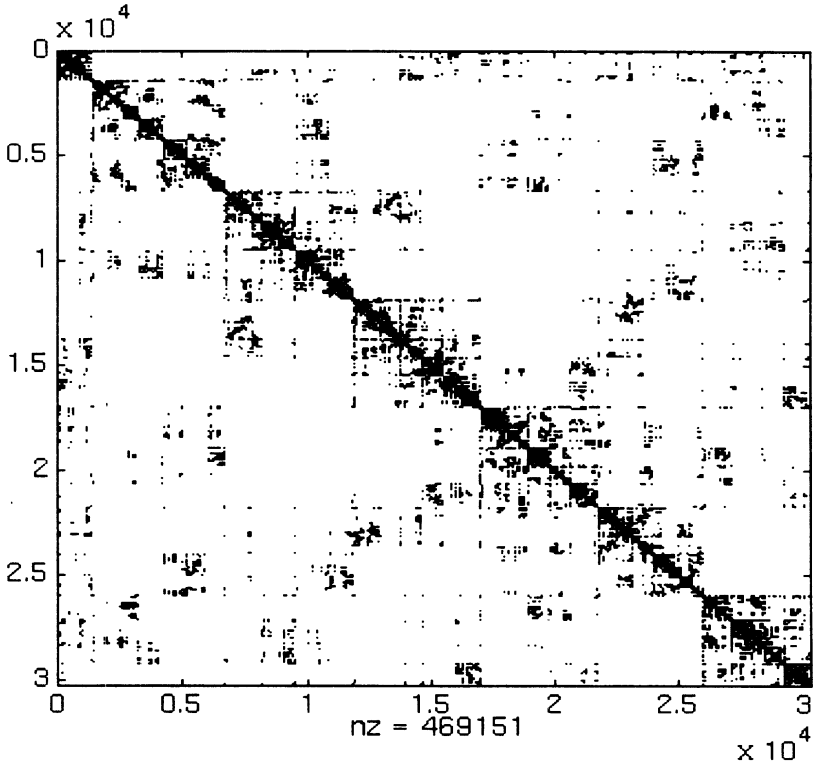

Figure 3: Examples of matrix systems generated by the finite element-boundary integral (top figure) and finite element-ABC methods (lower figure)

in practice) to absorb the outgoing waves and suppress backward reflections. Below, we briefly discuss the specifics for each of the three mesh termination schemes.

3 Mesh Termination Schemes

3.1 Finite Element-Boundary Integral Method

The FE-BI method was introduced in the early seventies [21],[22] as a natural extension of the FEM for modeling unbounded problems. However, because of its larger computational requirements, the method did not enjoy a widespread application to electromagnetics until the late eighties [23, 24]. In accordance with the FE-BI method, the relation between $\mathbf{E}$ and $\mathbf{H}$ on S_o is provided by the Stratton–Chu integral equation (or its dual)

$$\begin{aligned} \hat{n} \times \mathbf{H}(\mathbf{r}) &= \hat{n} \times \mathbf{H}^{inc}(\mathbf{r}) \\ &+ \hat{n} \times \iint_{S_o} \{[\hat{n}' \times \mathbf{H}(\mathbf{r})] \times \nabla' G_o(\mathbf{r}, \mathbf{r}') + jk_o Y_o [\hat{n}' \times \mathbf{E}(\mathbf{r})] G_o(\mathbf{r}, \mathbf{r}') \\ &+ j\frac{Y_o}{k_o} \nabla' \cdot [\hat{n}' \times \mathbf{E}(\mathbf{r}')] \nabla G_o(\mathbf{r}, \mathbf{r}') \Big\} \, dS' \end{aligned} \tag{13}$$

where $\mathbf{r}$ and $\mathbf{r}'$ denote the observation and integration points, respectively, and $G_o(\mathbf{r}, \mathbf{r}') = exp(-jk_o|\mathbf{r} - \mathbf{r}'|/(4\pi|\mathbf{r} - \mathbf{r}'|)$ is the free-space Green's function. The above is the most general form of the boundary integral and places no restrictions on the shape of S_o with the exception that it must be closed as shown in Figure 1(a). Provided S_o is placed just above the outer boundary of the scatterer or radiator, any material composition which is interior to S_o can be handled with ease using the FEM without relation to the boundary integral. This form of the FE-BI was used by Yuan [25] and later by Angélini *et. al.* [26], Antilla and Alexopoulos [27], and Soudais [28] to model three dimensional scatterers with anisotropic treatments. The method has also been successfully used for biomedical simulations [29],[30].

The discretization of (14) follows by introducing the expansion (over the s^{th} surface element)

$$\mathbf{E}(\mathbf{r}) = \sum_{k=1}^{n=\#\ of\ edges} E_k^s \mathbf{S}_k^s(\mathbf{R}) = [S^s]^T \{E^s\} \tag{14}$$

with a similar expansion for the $\mathbf{H}$ field (if necessary). The surface shape functions $\mathbf{S}^s(\mathbf{r})$ can be set equal to $\mathbf{W}^e(\mathbf{r})$ when the latter are evaluated on the surface of the volume element. For the tetrahedron, $\hat{n} \times \mathbf{S}_k$ are simply equal to the traditional basis functions given by Rao *et. al.* [31]. However, as pointed out in [32], $\mathbf{S}^s$ can be chosen independently of $\mathbf{W}^e$ provided care is exercised when (14) is substituted/combined with (2)-(6). Regardless, when (14) is substituted into (3) or (6) after discretization we will get the partly sparse, partly full system [33] given in (12) and illustrated in Figure 3(a). Finally, we point out that since S_o is a closed surface, the final system is not immune to

false interior resonances due to the boundary integral. In this case, the combined field formulation [34] or the simpler complexification scheme [35] may be employed.

When S_o coincides with an aperture in a ground plane (see Figure 1(b)), the integral equation (14) can be simplified substantially [36]. Specifically the integral relation between $\mathbf{E}$ and $\mathbf{H}$ on the aperture reduces to

$$\hat{n} \times \mathbf{H} = \hat{n} \times \mathbf{H}^{go} + \iint_{S_0} \hat{n} \times \bar{\mathbf{G}}(\mathbf{r}, \mathbf{r}') \left[\mathbf{E}(\mathbf{r}) \times \hat{n}\right] dS \tag{15}$$

where $\bar{\mathbf{G}}$ is the dyadic Green's function of the second kind, with $\hat{n} \times \nabla \times \bar{\mathbf{G}} = 0$ on S_o and for planar platforms it reduces to ,

$$\bar{\mathbf{G}} = -j\frac{2k_o}{Z_o}\left(\bar{\mathbf{I}} + \frac{1}{k_o^2}\nabla\nabla\right)\frac{e^{-jk_o|\mathbf{r}-\mathbf{r}'|}}{4\pi|\mathbf{r}-\mathbf{r}'|} \tag{16}$$

In this, $\bar{\mathbf{I}}$ is the unit dyad and the factor of 2 is due to image theory. Also, $\mathbf{H}^{go}$ is equal to the sum of the incident and reflected fields (in the absence of the aperture) for scattering or zero for antenna parameter computations. For non-planar S_o, $\mathbf{H}^{go}$ is equal to the field scattered by an otherwise smooth surface again with the aperture removed. In this case, the Green's function should also be modified accordingly with respect to the non-planar platform. One of the first implementations of the FE-BI for radiation and scattering from rectangular apertures/antenna recessed in a ground plane was given by Jin and Volakis [14],[33],[36] and was later extended to antenna analysis on planar [37], [38], [39] and cylindrical [40] platforms.

The FE-BI method is particularly attractive in terms of CPU and memory requirements when the $[\mathcal{G}]$ matrix is Toeplitz and can therefore be cast in circulant form [41],[42], [43], [44]. In this case, the entire system can be solved using an iterative solver [45] in conjunction with the FFT to reduce the CPU requirements down to $O(N_{se} log\ N_{se})$ for the boundary integral sub-matrix. The FFT is simply used to carry out the matrix-vector product $[\mathcal{G}]\{E^B\}$ within the iterative solver. For example, if the symmetric biconjugate gradient (BCG) method [45] is employed to solve (12) and rectangular elements are used, the storage requirement is only $4N_{ee} + 8N_{se}$, where N_{ee} and N_{se} denote the number of edges within the computational volume and on S_o, respectively. For triangular surface elements, the storage requirement is about 4.5 times larger due to the presence of the diagonal edges across the quadrilaterals. Whether the full matrix $[\mathcal{G}]$ is Toeplitz or not depends on the shape of the surface S_o and on the uniformity of the mesh. It can be shown that $[\mathcal{G}]$ will be Toeplitz for planar and cylindrical surfaces provided the surface grid is uniform. The Toeplitz form of $[\mathcal{G}]$ has been exploited with great success and systems with more than 0.5 million unknowns spanning apertures of $15\lambda \times 15\lambda$ have been solved accurately on a desktop workstation. Convergence of the iterative solver is also quite impressive for these systems and as demonstrated by Ozdemir and Volakis [46] (see Figure 4) the FE-BI method is the method of choice for these applications. For example, we observed that a 180,000 unknowns system converged in 57 iterations and for another system of 25,000 unknowns convergence was achieved after 66 iterations with an average CPU time of 2 sec/iteration on an HP9000/750 rated at 24.7 MFlops. Because of these impressive performances, it is advantageous to transform $[\mathcal{G}]$ to a Toeplitz matrix even

when the surface grid is not uniform. To do so, a uniform grid can be superimposed onto the non-uniform mesh (see Figure 5) and the edge fields on the two grids can be related via a connectivity matrix [39]. In this manner, non-rectangular antenna elements and apertures can be modeled with the full geometrical adaptability of the finite element method and without compromise in accuracy. It is important to note that similar transformation matrices can be exploited for decomposing computational domains as done, for example, in [47].

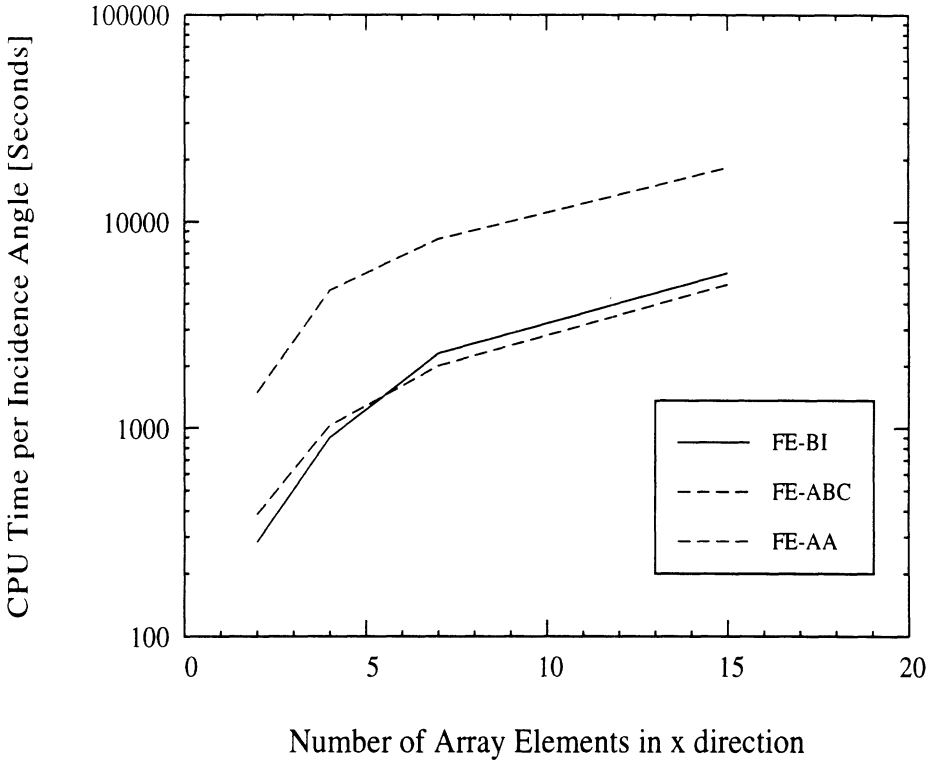

Figure 4: Comparison of the convergence behavior/CPU requirements among the FE-BI, FE-ABC and FE-AA methods

When S_0 is not planar, the boundary integral matrix will inevitably cause large CPU and storage requirements for large N_{se} to the point where FE-ABC or FE-AA methods become more attractive at the expense of accuracy. Recently, though, techniques have been proposed which show promise in reducing the computational requirements of the matrix-vector product $[\mathcal{G}]\{E^B\}$. Among them, the fast multipole method [48], [49] can reduce the operation count in carrying out the matrix-vector product from $O(N_{se}^2)$ down to $O(N_{se}^{1.5})$ and reductions down to $O(N_{se}^{1.33})$ have also been proposed. The main idea of the FMM [49] is to subdivide the surface S_o into groups, each containing approximately $M_{se} \approx \sqrt{N_{se}}$ unknowns. By rewriting the free space Green's function as an expansion [50] or by introducing its far field approximation [51], it can be shown that the interactions between the unknowns within the groups can be carried out in $O(N_{se}M_{se})$ operations whereas the interactions between groups can be carried out in $O(N_{se}^2/M_{se})$ operations. The sum of these two operation counts yields a total operation count of $O(N_{se}^{1.5})$ for the boundary integral matrix when $M_{se} \approx \sqrt{N_{se}}$, and this must be added to the $O(N_{ee})$ operation count associated with the sparse matrix $[\mathcal{A}]$. Details for the implementation

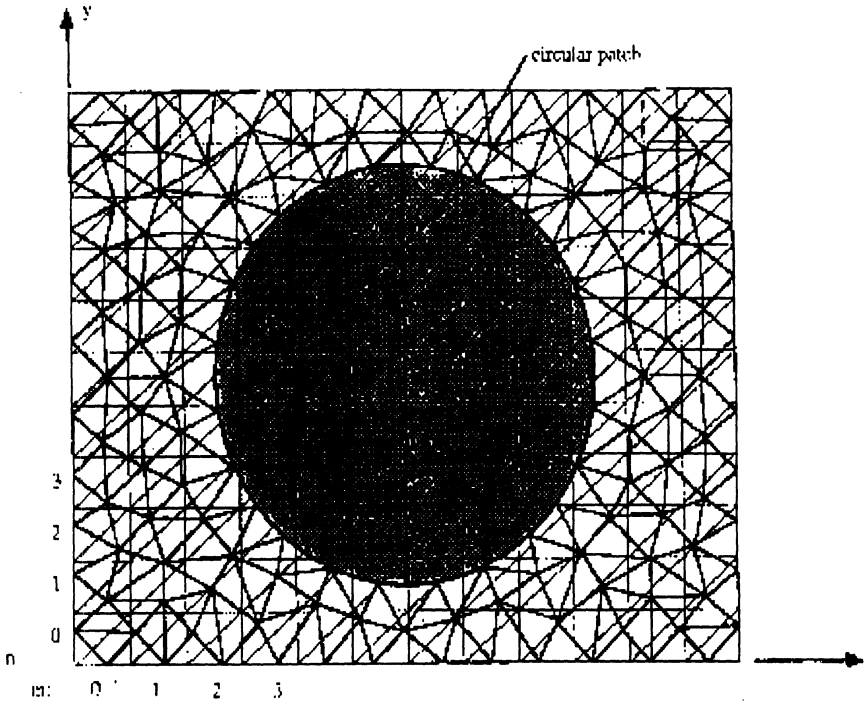

Figure 5: Overlay of a uniform grid on an unstructured mesh for implementation of the FFT to perform the matrix-vector products.

of the FMM are given in [48], [49] and when combined with the FEM, we can refer to it as the FE-FMM method [52]. A comparison of the FE-BI (with LU and conjugate gradient–FFT solvers) and the FE-FMM methods for the calculation of the scattering by a large groove in a ground plane is tabulated in Table 1. The groove was 50λ long and 0.35λ deep (all metallic) and filled with a dielectric having $\epsilon_r = 4$ and $\mu_r = 1$. By using a sampling rate of about 15 edges per wavelength, the system unknowns were $N_{ee} = 5256$ and $N_{se} = 750$. From the data in Table 1, it is clear that the FE-FMM is more than 3 times faster and requires 3–5 times less memory than the FE-BI when LU decomposition is used for solving the FE-BI system. Because of the grouping/averaging of the surface elements, the FE-FMM exhibits certain errors which are functions of many parameters [53] and these errors must be kept in mind as the system size is increased. It is expected that the FMM will exhibit greater speed-ups as the system size is increased. Nevertheless, the special implementation of the FE-BI using the FFT is still by far the most accurate approach.

We close this section by noting that another approach for treating the boundary integral matrix-vector products is via the adaptive integral method (AIM) [54]. This approach relies on the introduction of multipole expansions (similar to Taylor series expansions) to replace the sources on S_o by equivalent point sources placed on rectangular grids. In this manner the CPU requirements can be reduced by making use of three dimensional FFT routines. It can again be shown that AIM reduces the boundary matrix CPU requirements down to $O(N_{se}^{1.5})$ or even down to $O(N_{se}^{1.33})$.

Groove Width	Total Unknowns	BI Unknowns	*CPU Time for BI (Minutes,seconds)*		
			FE-BI (CG)	FE-FMM	FE-BI (CGFFT)
25λ	2631	375	(8,48)	(3,26)	(1,41)
35λ	3681	525	(16,34)	(5,55)	(3,24)
50λ	5256	750	(45,1)	(14,31)	(5,40)

	Storage of BI (KB)	
Groove Width	FE-BI (CG)	FE-FMM
25λ	1072	277
35λ	2102	458
50λ	4291	784

	RMS error (dB)
Groove Width	FE-FMM
25λ	1.12
35λ	1.2
50λ	1.36

Table 1: CPU Times, storage requirement and error

3.2 Finite Element–Absorbing Boundary Condition Method

The goal with any ABC is to eliminate backward reflections from S_o, and a variety of these boundary conditions have been proposed over the years beginning with those of Bayliss and Turkel [55], and Engquist and Majda [56]. More recently, other ABCs such as those by Webb and Kanellopoulos [57], and Chatterjee and Volakis [4] (see also Senior and Volakis [2]) have been proposed. All ABCs provide an approximate relation between the **E** and **H** fields on the surface S_0 which in most cases is derived by assuming a field expansion in inverse powers of r, where r is the radial distance from the center of S_0. If the ABC annihilates the first $(2m+1)$ inverse powers of r, it is then referred to as an mth order ABC. The second order ABC derived by Chatterjee and Volakis [4] is given by

$$jk_0Z_0(\mathbf{H}^{scat}\times\hat{n}) = \bar{\bar{\alpha}}\cdot\mathbf{E}_t^{scat} + \bar{\bar{\beta}}\cdot[\nabla\times\hat{n}(\nabla\times\mathbf{E}^{scat})_n] + \bar{\bar{\gamma}}\cdot\nabla_t(\nabla\cdot\mathbf{E}_t^{scat}), \qquad (17)$$

where

$$\begin{aligned}
\bar{\bar{\alpha}} &= \alpha_1\hat{t}_1\hat{t}_1 + \alpha_2\hat{t}_2\hat{t}_2\\
\bar{\bar{\beta}} &= \eta(\hat{t}_1\hat{t}_1 + \hat{t}_2\hat{t}_2)\\
\bar{\bar{\gamma}} &= \frac{\eta}{jk_0}(jk_0+3\kappa_m-\frac{\kappa_g}{\kappa_m}-2\kappa_1)\hat{t}_1\hat{t}_1 + \frac{\eta}{jk_0}(jk_0+3\kappa_m-\frac{\kappa_g}{\kappa_m}-2\kappa_2)\hat{t}_2\hat{t}_2\\
\alpha_1 &= \eta[4\kappa_m^2-\kappa_g+D(jk_0-\kappa_1)+\kappa_1^2+\kappa_m\Delta\kappa]\\
\alpha_2 &= \eta[4\kappa_m^2-\kappa_g+D(jk_0-\kappa_2)+\kappa_2^2-\kappa_m\Delta\kappa]\\
\eta &= \frac{1}{D-2\kappa_m}\\
\Delta\kappa &= \kappa_1-\kappa_2\\
D &= 2jk_0+5\kappa_m-\frac{\kappa_g}{\kappa_m}.
\end{aligned}$$

In the above equation, the subscripts n and t denote surface normal and tangential components of the field, $\hat{t}_1, \hat{t}_2$ are the principal surface directions and κ_1, κ_2 are the corresponding curvatures, $\kappa_m = (\kappa_1+\kappa_2)/2$ is the mean curvature and $\kappa_g = \kappa_1\kappa_2$ is the

Gaussian curvature. For $\kappa_1 = \kappa_2$ (spherical termination boundary), (17) reduces to the ABC derived by Webb and Kanellopoulos [57]. The latter authors have recently proposed a correction [58] for the implementation of these ABCs which should be incorporated in existing codes.

Upon substituting (17) into the surface integral of (6) and making use of vector differential and integral identities [59], we have

$$\begin{aligned} jk_o Z_o \iint_{S_o} \mathbf{E}^{scat} \cdot (\mathbf{H} \times \hat{n})\, dS &= \iint_{S_o} [\alpha_1 (E_{t_1}^{scat})^2 + \alpha_2 (E_{t_1}^{scat})^2] dS \\ &+ \iint_{S_o} \eta (\nabla \times \mathbf{E}^{scat})_n^2 dS \\ &- \iint_{S_o} (\nabla \cdot \mathbf{E}_t^{scat})[\nabla \cdot (\bar{\bar{\gamma}} \cdot \mathbf{E}^{scat})_t] dS. \end{aligned} \tag{18}$$

Next, expansion (6) or (14) is introduced and (18) is differentiated as in (7) to obtain the finite element equations (8) . Since the ABC is a local condition, the sparsity of the finite element matrix is preserved and the resulting system is again given by (12) with $[\mathcal{G}]$ removed. However, in the case of arbitrarily curved boundaries, the matrix will not be symmetric except for planar and spherical boundaries. The system will be also symmetric for cylindrical boundaries only if linear edge-based expansion functions are used. These ABCs have been extensively validated for a number of antenna and scattering configurations[59], [60]. Higher order ABCs have been proposed for a more effective suppression of the outgoing waves. These are often difficult to implement but as demonstrated by Senior *et. al.* [61], they provide greater accuracy and effort being placed so much closer to the scatterer or radiator.

3.3 Finite Element–Isotropic Absorber Method

In accordance with this method, the outgoing waves are suppressed by an absorbing dielectric layer placed at some distance from the antenna as shown in Figure 6. Typically, the layer is backed by metal and the finite element region extends all the way to the metal at which point the mesh is terminated by setting the tangential component of the total electric field to zero. This is equivalent to removing the integral over S_o in (2)-(6). Obviously, the accuracy of the technique depends on how well the metal-backed absorber suppresses the incoming waves without introducing backward reflections. The plane wave reflection coefficient of the absorber shown in Figure 6 has been minimized over the entire visible angular range [46]. The fact that the dielectric has the same relative permittivity and permeability ensures that there is no reflection from the air-dielectric interface at normal incidence (perfect impedance match), but the performance degrades away from normal with the reflection coefficient reaching unity at grazing. This limitation led researchers to consider perfectly matched interfaces as discussed next. Nevertheless, even though the isotropic absorbers are not perfect, they are still useful in modeling antennas on doubly curved platforms. Figure 7(a) displays a sectoral microstrip patch printed on a conical surface and Figure 7(b) shows the antenna resonance behavior for different cone angles. We clearly observe that the resonance frequency drops with the cone angle for the same patch dimensions. It should be also

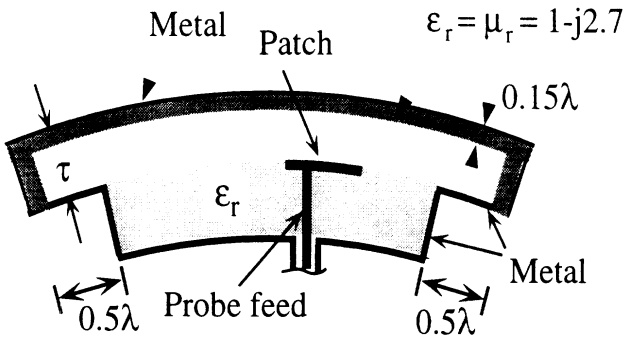

Figure 6: Illustration of an antenna terminated by an isotropic absorbing material

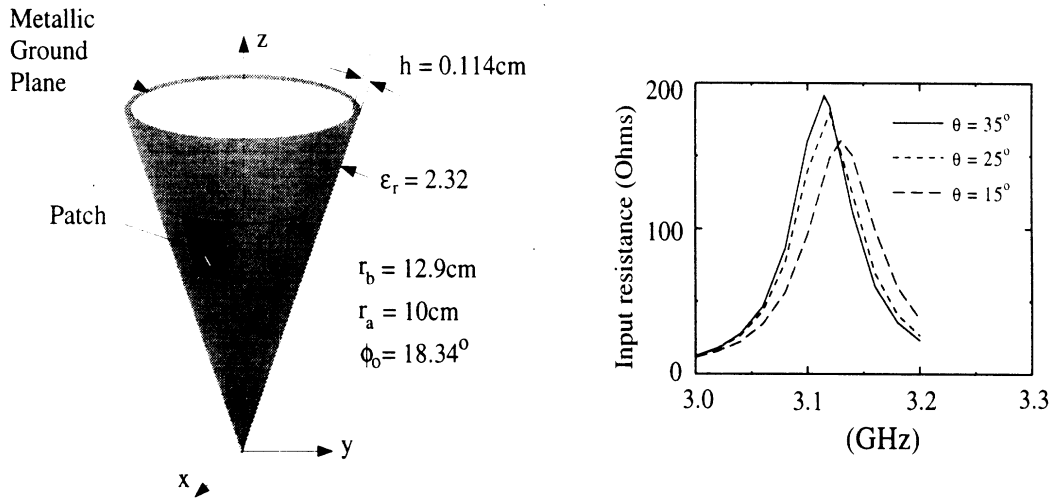

(a) (b)

Figure 7: Sectoral microstrip patch on cone

remarked that the computed resonance frequency is within 3.2 percent of that predicted by the approximate cavity model, and this is reasonable.

In generating the results given in Figure 7, the computational domain was discretized using 2,358 prisms resulting in 3,790 degrees of freedom. One frequency run took 5.5 minutes on an HP9000 (Model 715/64) workstation rated at 22 MFlops.

3.4 Finite Element–Anisotropic Absorber Method

This mesh termination method is similar to that described in the previous section except that the layer is comprised of an anisotropic lossy dielectric which has zero reflection coefficient at the air-dielectric interface over all incident angles and can therefore be considered as a perfectly matched interface (PMI) [20]. The intrinsic parameters of the PMI layer are

$$\frac{\bar{\bar{\mu}}_r}{a} = \bar{\bar{\epsilon}}_r = \begin{bmatrix} \alpha - j\beta & 0 & 0 \\ 0 & \alpha - j\beta & 0 \\ 0 & 0 & \frac{1}{\alpha - j\beta} \end{bmatrix}$$

where $a = (Z/Z_0)^2$, Z is the intrinsic impedance of the medium being terminated by the absorber, whereas α, β and the thickness of the layer are parameters which can be optimized for maximum absorption.

The advantage of the anisotropic (over the isotropic) artificial absorber in terminating finite element meshes is illustrated in Figure 8 [62] where it is shown that the anisotropic absorber retains its low reflectivity at oblique incidences except near grazing ($\phi = 0°$). The performance shown in Figure 8 is based on a purely theoretical analysis but as shown in Figure 9, this performance can be realized in numerical simulations with careful choices of βt and the sampling rate N within the absorber. It has been found [63] that the reflectivity curve shown in Figure 9 is typical to most situations and the location of the minimum reflection coefficient can be predicted *a priori*. An extensive numerical study based on a two dimensional planar absorber model demonstrated that $\beta t/\lambda_x$ ($\lambda_x = \lambda_0/\cos\phi$) is a scalable parameter and that given the desired reflection coefficient $|R|$, the formulas [62]

$$\frac{\beta t}{\lambda_x} = -0.0106|R| + 0.0433 \tag{19}$$

$$N = 0.147exp[7.353\frac{\beta t}{\lambda_x}] \tag{20}$$

can be used to choose $\beta t/\lambda_x$ and the minimum number of discrete samples to achieve the desired absorption. In these, $|R|$ is specified in dB and λ_o denotes the free space wavelength. These formulas are in agreement with the actual numerical results in Figure 9 but it has yet to be determined how well they apply for curved perfectly matched layers which are placed conformal to scattering and radiating surfaces. Improvements to their absorptivity though can be attained by considering tapered layers and formulas similar to (19)-(20) are given by Legault [62] for one such tapered anisotropic absorber.

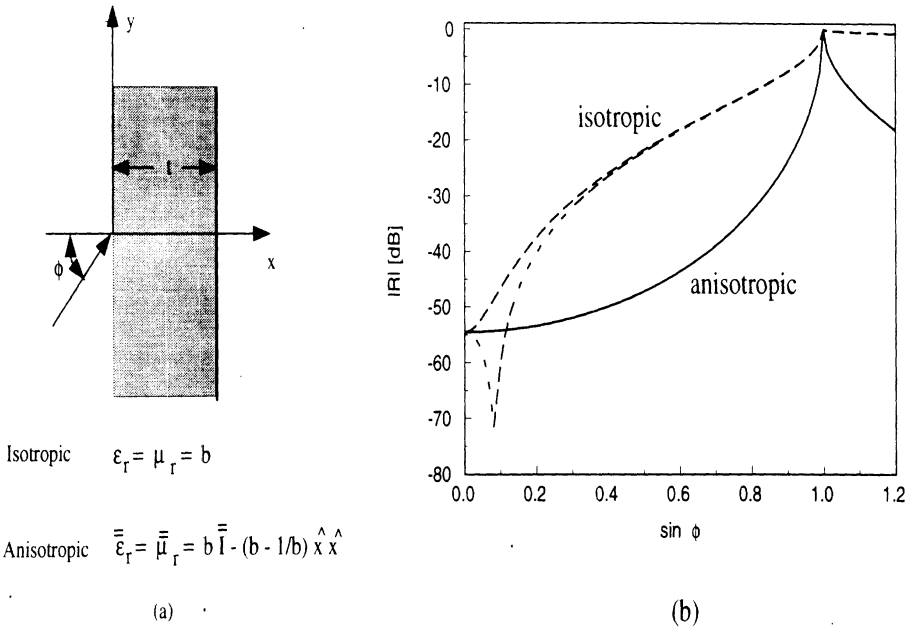

Figure 8: Reflectivity of a $\lambda/4$ thick planar metal-backed perfectly matched absorber ($\beta = 1 - j2$) as a function of incidence angle. (a) Geometry, (b) plane wave reflection coefficient vs. angle

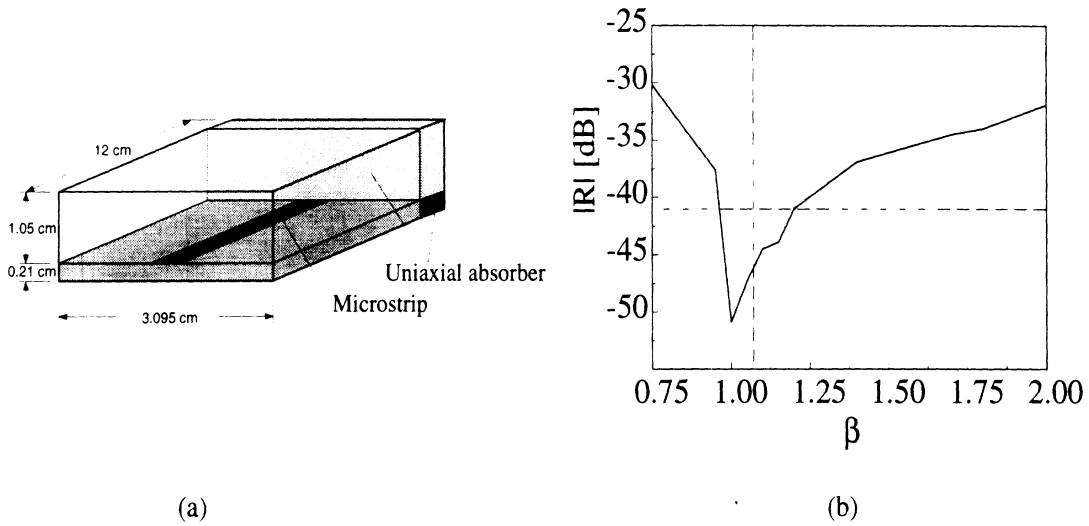

Figure 9: Reflection coefficient of the PMI for terminating a microstrip line as extracted from a numerical implementation

4 Feed Modeling

For scattering problems where the plane wave incidence is usually the 'source', the right-hand-side excitation has been explicitly given in (12) and will not be discussed further. However, for antenna parameter computations, the explicit form of $\{K^e\}$ in (11) will depend on the type of feeding scheme being employed. Below we discuss specific forms of $\{K^e\}$ corresponding to different feeding choices.

Simple Probe Feed: For thin substrates the coaxial cable feed may be simplified as a thin current filament of length l carrying an electric current $I\hat{l}$. Since this filament is located inside the cavity, the first term of the integral in (2) or (3) needs to be considered for this model. Specifically, the ith (global) entry of the excitation vector K_i becomes

$$K_i = jk_0 Z_0 I\, \hat{l} \cdot \mathbf{W}_i(\mathbf{r}), \qquad i = j_1, j_2, ..., j_m \tag{21}$$

where $\mathbf{r}$ is the location of the filament, m is the number of (non-metallic) element edges and j_m is the global edge numbering index. In general, m such entries are associated with m element edges, and thus the index i goes from j_1 up to j_m. This expression can be further reduced to $K_i = jk_0 Z_0 I\, l$, provided that the ith edge is coincident with the current filament.

Voltage Gap Feed: This excitation is also referred to as a *gap generator* and amounts to specifying *a priori* the electric voltage V across the opening of the coax cable or any other gap. Since $V = \mathbf{E} \cdot \bar{d}$, where $\bar{d}$ is a vector whose magnitude is the gap width, and $\mathbf{E}$ the electric field across the gap, we have that $E_i = \dfrac{V}{d cos\theta_i}$, where $cos\theta_i$ is equal to 1 if the ith edge is parallel to $\bar{d}$. Numerically, this gap voltage model can be realized by first setting the diagonal term A_{ii} of the $[\mathcal{A}]$ matrix equal to unity and the off-diagonal terms A_{ij} $(i \neq j)$ to zero. For the right-hand-side vector, only the entry corresponding to the ith (global) edge across the gap is specified and set equal to the value E_i whereas all other entries associated with edges not in the gap are set to zero.

Coaxial Cable Feed Model: The simple probe feed of the coaxial cable is accurate only if the substrate is very thin. For thicker substrates, an improved feed model is necessary and this can be achieved by evaluating the functional

$$F_C = -jk_0 Z_0 \iint_{S_f} (\mathbf{E} \times \mathbf{H}) \cdot \hat{z}\, dS \tag{22}$$

over the aperture S_f of the coax cable. Assuming a TEM mode across S_f, the fields within the cable may be expressed as (see Figure 10) [64]

$$\mathbf{E} = \frac{e_0}{r}\hat{r}, \qquad \mathbf{H} = \frac{h_0}{r}\hat{\phi}, \tag{23}$$

with

$$h_0 = -\frac{\sqrt{\epsilon_{rc}}}{Z_0} e_0 + \frac{I_0}{\pi}. \tag{24}$$

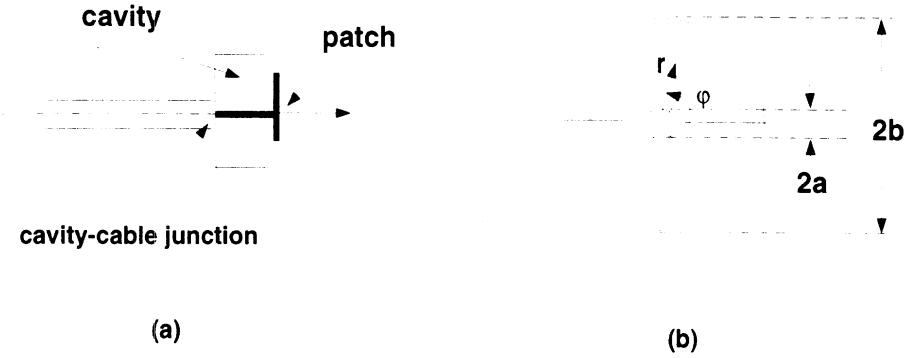

Figure 10: (a) Side view of a cavity-backed antenna with a coax cable feed; (b) Illustration of the FEM mesh at the cavity-cable junction (the field is set to zero at the center conductor surface).

In these expressions, ϵ_{rc} is the relative permittivity inside the cable, $\mathbf{E}$ and $\mathbf{H}$ are the electric and magnetic fields, respectively, measured at $z = 0$ and I_0 is the center conductor current. Also, (r, ϕ, z) are the polar coordinates of a point in the cable with the center at $r = 0$. We observe that (24) is the desired constraint at the cable junction in terms of the new quantities h_0 and e_0 which can be used as new unknowns in place of the fields $\mathbf{E}$ and $\mathbf{H}$.

However, before introducing F_C into the system, it is necessary to relate e_0 and h_0 to the constant edge fields associated with the elements in the cavity region which border the cable aperture. Since the actual field has a $1/r$ behavior in the cable, we find that

$$\Delta V = E_i(b-a) = e_0 ln\frac{b}{a}, \qquad i = N_p(p = 1, 2, ..., N_C) \tag{25}$$

where ΔV denotes the potential difference between the inner and outer surface of the cable and N_p denotes the global number for the edge across the coax cable. When this condition is used in the functional F_C, it introduces the excitation into the finite element system without a need to extend the mesh inside the cable or to employ a fictitious current probe. The derivation of $\frac{\partial F_C}{\partial E_i}$ and its incorporation into the system is then a straightforward task [64]. As can be expected, the above feed model assumes the presence of only the dominant(TEM) mode at the cavity-cable junction, an assumption which may not be suitable for certain applications. Of course, the model can be improved by extending the mesh (say, a distance d) into the cable. The equi-potential condition will then be applied at z=-d, where all higher order modes vanish.

Aperture-Coupled Microstrip Line Model: As shown in Figure 11, when the microstrip antenna is fed with a microstrip line network underneath the ground plane (cavity's base) via a coupling aperture, special treatment of the feed structure must be considered in the FEM formulation. This is because the microstrip line is usually designed to have different size and shape as compared to the cavity's geometries. Hence, the conventional simulation of treating the entire 3-D domain using a single type of element is not efficient or appropriate for this feed.

Referring to Figure 11, it is appropriate to separate the computational domains because of the small element size required in modeling the guided feed structure. As an example, let us consider a rectangular aperture which has been extensively employed in practice. The cavity fields may be discretized using tetrahedral elements, whereas in the microstrip line region rectangular bricks are the best candidate since the feed structure is rectangular in shape and the substrate is of constant thickness. Although both types

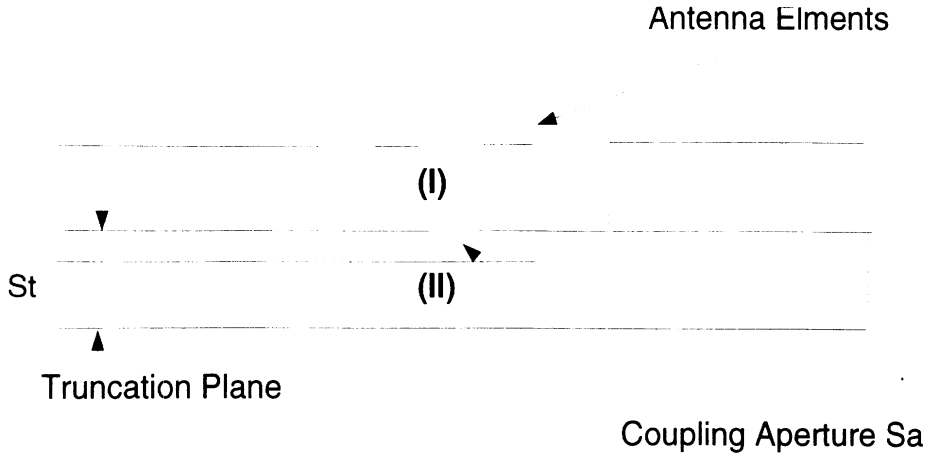

Figure 11: Cross-section of an aperture coupled patch antenna, showing the cavity region I and the microstrip line region II for two different FEM computation domains.

of elements employ edge-based field expansions, the meshes across the common area (coupling aperture) are different, and consequently some connectivity matrix must be introduced to relate the mesh edges across the aperture. However, since the aperture is very narrow, a 'static' field distribution may be assumed at any given frequency. Therefore, the *potential* concept may be again applied to relate the fields below and above the aperture. Specifically, the 'equi-potential' continuity condition is enforced, and to demonstrate its implementation, let us first classify the slot edges as follows

Tetrahedral Mesh (Cavity Mesh):

- E_j^{b1} $j = 1, 2, 3, ...$ *vertical edges*
- E_j^{b2} $j = 1, 2, 3, ...$ *diagonal edges*

Brick Mesh (Feed Mesh):

- E_j^c $j = 1, 2, 3, ...$ *vertical edges only*

Then the 'equi-potential' continuity condition requires that

$$E_j^{b1} = \epsilon_j E_j^c$$
$$E_j^{b2} = \frac{t}{2d}(\epsilon_j E_j^c + \epsilon_{j+1} E_{j+1}^c)$$

in which

$$\epsilon_j = \begin{cases} +1 \\ -1 \end{cases},$$

whereas t and d are the lengths of the vertical and diagonal edges, respectively. That is, t is simply the width of the narrow rectangular aperture. The coefficient ϵ_j is equal to ± 1 depending on the sign conventions associated with the meshes above and below the coupling aperture.

This connectivity scheme can be extended to entirely different computational domains. Also, it is apparent that the approach makes the FEM implementation straightforward for different geometry/size domains that would be significantly inefficient if only one type of elements were used for modeling the structure. In addition, the technique ensures a good system condition since the number of distorted elements in the mesh is minimized.

5 Parallelization

When considering 3D problems of practical interest, the unknown count of the computational domain can easily reach several million degrees of freedom. The sparsity of the FEM system (particularly for the FE-ABC and FE-AA methods) makes possible the storage of such large scale problems but even at O(N) computational demands, their practical solution requires efficient use of parallel and vector platforms. Modern computing platforms can now deliver sustained speeds of several GFlops and CPU speeds in the Tflops range are within our reach. The inherent sparse matrices of PDE methods are particularly suited for execution on multiprocessor and vector platforms but the exploitation of these processors requires special storage schemes and techniques to perform the matrix-vector product required in the iterative algorithms at the Flop rates sustained on these multiprocessors.

To parallelize and vectorize the FEM codes, it is essential to first optimize the execution of the iterative solvers which typically take-up 90% of the CPU time. Among them, the conjugate gradient algorithms (CG, BCG, CGS and QMR) have been found very attractive and a brief comparison of the pros and cons for these is given in [45]. The Generalized Minimal Residual Method (GMRES) is another iterative solver which can exhibit faster convergence rates. However, it stores the direction vectors and as a result it requires much higher storage. For the discussion below we will primarily concentrate on the BCG and QMR algorithms and we note that the symmetric form of BCG requires minimal number of arithmetic operations (see Table 2). A disadvantage of the BCG is its erratic convergence pattern whereas the QMR has smooth and monotonic convergence. However, neither BCG nor QMR can guarantee convergence and typically they both converge or not for the same problem. When considering the parallelization of a completely sparse system such as that resulting from the FE-ABC method, the following issues must be addressed:

Storage of Sparse System: The performance of the code is strongly dependent on the employed storage scheme. Since a typical FEM matrix has about 8.5 N_{ee} or so non-zero entries, it is essential that the non-zero elements be stored in a manner that keeps the storage requirements nearly equal to the non-zero entries and minimizes inter-processor communications. The ITPACK [65] and the compressed row storage (CRS) schemes are most appropriate for parallel computing. The ITPACK storage format is most efficient

	Complex	
Operation	$\star$	+
Matrix-vector Products	nze	nze-N
Vector Updates	4N	3N
Dot Products	3N	3N
Total # of Operations	29N	3N

N = # of unknowns
nze = # of nonzero matrix elements

Table 2: Floating Point Operations of BCG Per Iteration

for retrieving the matrix elements and certainly the choice method when the number of non- zero elements are nearly equal for every matrix row. Basically, the ITPACK format casts the FEM matrix in a smaller rectangular matrix having the same rows as the original matrix and can be unpacked by referring to a pointer integer matrix of the same size. However, this rectangular matrix can contain as much as 50% zeros which results in space wastage. By using a modified ITPACK scheme, space wastage can be reduced down to 30%. Even with less wastage, the CRS format may be the most efficient storage scheme with some compromise in CPU speed. It amounts to storing $[\mathcal{A}]$ as a single long row which can be uncompressed using two integer pointer arrays. For the symmetric BCG algorithm, the CRS format results in only 8.5 N complex numbers and N integers. However, it should be pointed out that the CRS format is not appropriate for vector processors such as the C-90. For vectorization, it is best to organize the storage in sections of long vectors and to achieve this for our type of matrices the jagged diagonal format [66] appears to work best. Using this format the rows are reordered so that the row with the maximum number of non- zeros is placed at the top of the matrix and rows with the least non-zero entries are shuffled to the bottom. This reordering greatly enhances vectorization because it allows tiling of the shorter rows to yield very long vector lengths in the matrix-vector multiplication phase. Specifically, for some problem the jagged diagonal storage format allowed the matrix-vector multiplication routine to run at about 275 MFlops on a Cray C-90 whereas the same routine ran at 60 MFlops using the CRS format. The dot product speeds and the vector updates reached 550 MFlops and 600 MFlops for the same problem. Table 3 provides a relative comparison of CPU estimates on various computers.

Interprocessor Communications: For distributed memory platforms, the method of partitioning the stiffness matrix $[\mathcal{A}]$ among the processors, the chosen storage scheme and the inherent unstructured sparsity of $[\mathcal{A}]$ are all crucial to the overall speed of the code. An approach that has worked well on massively parallel processors (such as the SP-2, Intel Paragon, Convex Exemplar) is that of assigning each processor a section of the matrix and by dividing the vectors among the P processors. Thus, each processor is responsible for carrying out the matrix-vector product for the block of the matrix it owns. However, the iterate vector is subdivided among all processors, and therefore narrow-band or structured sparse matrices have an advantage because they reduce in-

Processors	# of Processors, P	Tiem (μ-secs/iteration/unknown)
Cray C-90	1 (275 MFlops)	0.55
KSR 1	28	1.28
	58	0.57
Intel Paragon	8	3.42
	16	1.99
	32	1.38
IBM SP-1	4	1.47

Table 3: CPU Time Per Unknown for Solving Typical FE–ABC Systems

terprocessor communication. Since typical FEM matrices are unstructured, algorithms such as the Recursive Spectral Bisection (RSB) have been found very effective in reducing inter-processor communication. However, the standard Gibbs-Pool-Stockmeyer profile reduction algorithm has been found even more effective in reducing the initial FE-ABC matrix (see Figure 3) to banded form as illustrated in Figure 12. This type of matrix reordering can deliver speed-ups as close to linear as possible.

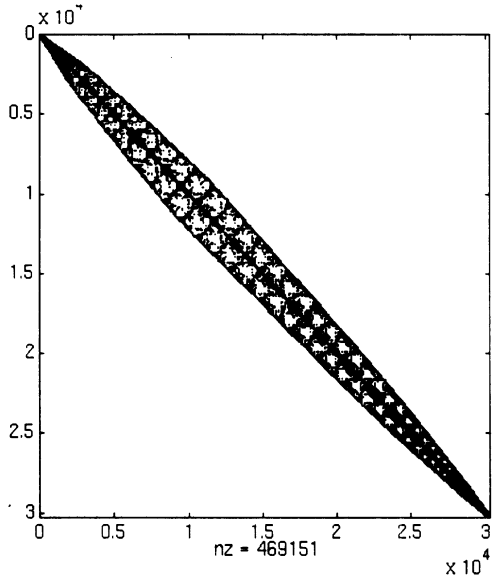

Figure 12: Reduced bandwidth of the FE-ABC system after application of the Gibbs-Pool-Stockmeyer profile reduction algorithm

Matrix Preconditioning: Preconditioned iterative solvers are intended to improve the convergence rate of the algorithm. At times, preconditioners are necessary as may be the case with some dielectrically loaded structures. However, for relatively small systems (less than 100,000 unknowns) it has been found that diagonal preconditioning is typically most effective and should always be applied. This preconditioning amounts to normalizing each row by the largest element, but even this simple operation can lead to substantial convergence speed-ups. Block and incomplete LU preconditioners are more effective in improving the convergence of the solver but are more costly to implement

and one must judge on the overall CPU requirements rather than on the improved convergence alone. For example, the incomplete LU preconditioner given in [67] reduced the iterations to 1/3 of those needed with diagonal preconditioning. However, each iteration was 3 times more expensive due to the triangular solver bottleneck.

6 Additional Applications

We choose three more examples to demonstrate the capability of the hybrid finite element methods.

Scattering by a Large Cone–Sphere: A cone-sphere is basically a hemisphere attached to a cone. This is a difficult geometry to mesh since a surface singularity exists at the tip of the cone. The singularity can be removed in two ways: i) by creating a small region near the tip and detaching it from the surface or ii) by chopping off a small part near the tip of the cone. The second option inevitably leads to small inaccuracies for backscatter from the conical tip; however, we chose this option since the conical angle in our tested geometry was extremely small (around 7°) and the mesh generator failed to mesh the first case on numerous occasions. In Figure 13, we plot the backscatter patterns of a 4.5λ long cone-sphere having a radius of 0.5λ for $\theta\theta$ polarization. The mesh truncation surface is a rectangular box placed 0.4λ from the surface of the cone-sphere. As seen, the far-field results compare extremely well with computations from a body of revolution code [68].

Frequency Selective Surfaces (FSS): FSS structures [69] are arrays of tightly packed periodic elements which are typically sandwiched between dielectric layers. The periodic elements may be of printed form or slot configurations designed to resonate at specific frequencies. As such, they are penetrable around the element resonances and become completely reflecting at other frequencies. To meet bandwidth design specifications, stacked element arrays may be used in conjunction with dielectric layer loading. Here we consider the analysis of FSS structures via the FE–BI method. Because of the fine geometrical detail associated with the FSS surface, the finite element method has yet to be applied for the characterization of FSS structures, but use of prismatic elements makes this a much easier task. Of particular interest in FSS design is the determination of the transmission coefficient as a function of frequency, and since the array is periodic, it suffices to consider a single cell of the FSS. For computing the transmission coefficient T, the periodic cell is placed in a cavity as shown in Figure 14 and the structure is excited by a plane wave impinging at normal incidence. Assuming that near resonance the wave transmitted through the FSS screen will retain its TEM character, the transmission coefficient of the FSS panel can be approximated as

$$T_{dB}^{(0)} = 10 \log \left| \frac{E^s}{\alpha} \right|$$

where α is the reflection coefficient of the absorber placed at the bottom of the cavity and should be kept small (< 0.1) to suppress higher order interactions. By adding the next higher order interaction, a more accurate expression for the transmission coefficient

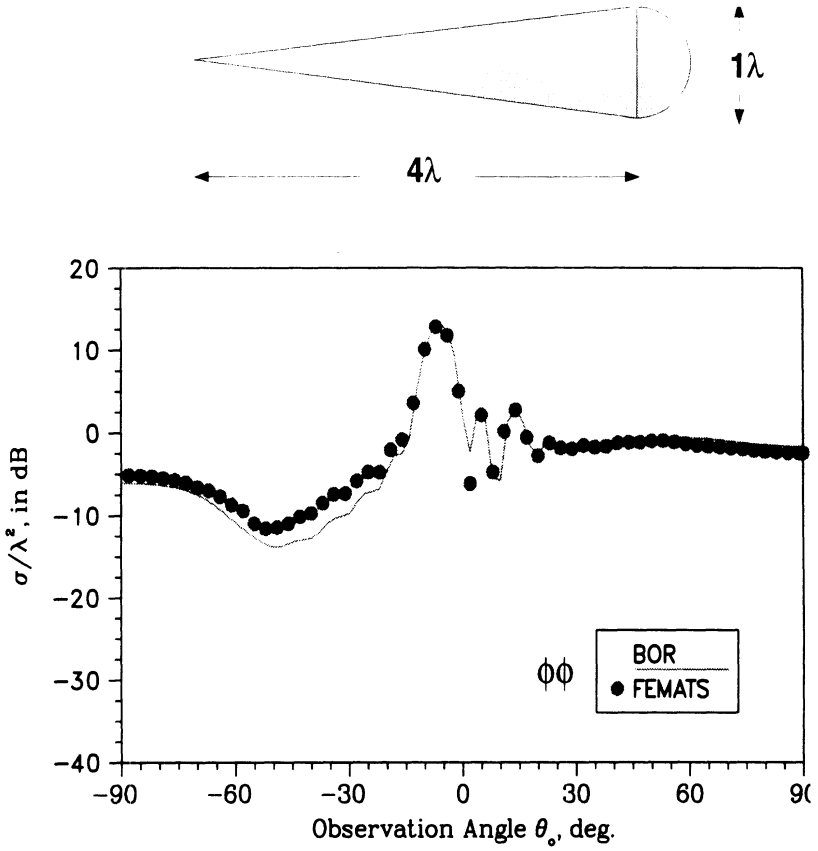

Figure 13: Backscatter pattern of a perfectly conducting conesphere for $\phi\phi$ and $\theta\theta$ polarizations. Black dots indicate computed values using the FE-ABC code (referred to as FEMATS) and the solid line represents data from a body of revolution code [68]. Mesh termination surface is a rectangular box.

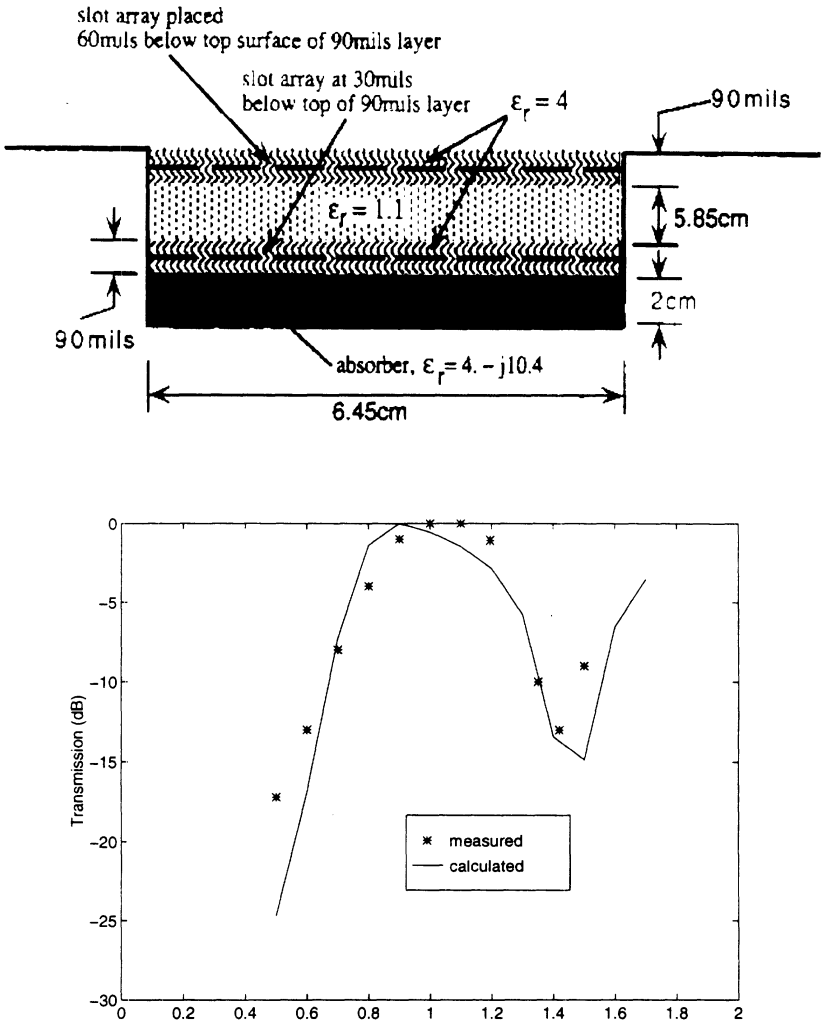

Figure 14: Upper figure: geometry of the multilayer frequency selective surface (FSS) used for modeling; lower figure: measured and calculated transmission coefficient through the FSS structure

is

$$T_{dB} \approx T_{dB}^{(0)} + 10 \log \left[1 - \alpha(1 - T^{(0)})\right].$$

The above FSS modeling approach was applied for a characterization of multi–layered slot FSS structures. The geometry of the multilayer radome is given in Fig. 14. The total thickness of the FSS was 6.3072cm and is comprised of two slot arrays (of the same geometry) sandwiched within the dielectric layers. For modeling purpose, a 1.54cm thick absorber is placed below the FSS as shown in Fig 14. It is seen that the results generated by the FE–BI method are in good agreement with the measurements [70].

Scattering by Jet Engine Inlets:

This example demonstrates a hybridization of the finite element and high frequency methods for scattering by jet engine structures[71]. In this hybridization, the jet engine itself is modeled by the FEM taking advantage of the geometrical adaptability of

finite methods. The fields generated by the FEM are then propagated to the mouth of the jet engine using a ray technique such as the geometrical theory of diffraction or the shooting and bouncing ray methods. To analyze the scattering by the jet engine, the blade structure is placed in a computational domain which is truncated by a perfectly matched absorbers at about 0.5 wavelengths from the engine face. By exciting the engine on a mode by mode basis, the appropriate modal scattering matrix is generated using the procedure described in [71]. However, in this case the computational domain is confined to a single blade lobe (cylindrical periodic cell) using appropriate phase boundary conditions at the boundaries of the periodic cells. This reduces the computational requirements to very low orders and permits the simulation of practical jet engine geometries. Given the modal scattering matrix of the jet engine, high frequency techniques can be readily used for propagating the fields to the inlet opening as described by Karty et.al.[72]. A demonstration on the accuracy of this hybrid technique is given in Figure 15 where we show the computed scattered field due to a single mode excitation. The specific engine-blade geometry was placed in a cylindrical metal-backed cavity as shown in Figure 15. It consisted of 20 straight blades mounted radiallly on a cylindrical hub 9.25" in radius with the blades extending all the way to the outer wall of the cavity which was 14.375" in radius. The blades were 2 degrees thick and $2.75"long, whereastheentireinletdepthwas19.685"$ and we remark that this configuration is similar to an F4 fighter engine. The shown computation was carried out at 4.348GHz and involved the solution of an FEM system with only 87,000 edges (64,000 elements) since a single periodic lobe was descretized but the overall structure spans about 4.5 wavelengths in diameter. As seen the agreement between the FEM computations and those of the reference modal solution are in excellent agreement, nearly overlaying each other.

7 Conclusion

In this paper we reviewed hybrid finite element methods as applied to electromagnetic scattering and radiation problems. Much of the emphasis dealt with the various mesh truncations schemes and we presented an up-to-date account of these schemes. The usual finite element-boundary integral method was presented and new developments for reducing the CPU requirements of this technique using the fast integral methods were discussed. Antenna feed modeling in the context of the finite element method had not been discussed before and for the first time we presented an overview of the modeling approaches for the most popular antenna feeds, including aperture coupled feeds. Parallelization will continue to play an increasingly greater role and a section was included discussing our experiences for better implementation of finite element codes on distributed and vector architectures. A number of examples illustrating the successful application of the finite element method were included throughout the paper and these were intended to demonstrate the method's geometrical adaptability and inherent capability to treat highly heterogeneous structures.

As can be expected, issues relating to mesh truncation, mixing of elements [73], domain decomposition[74, 75], robustness, adaptive refinement[76], accuracy, error control,

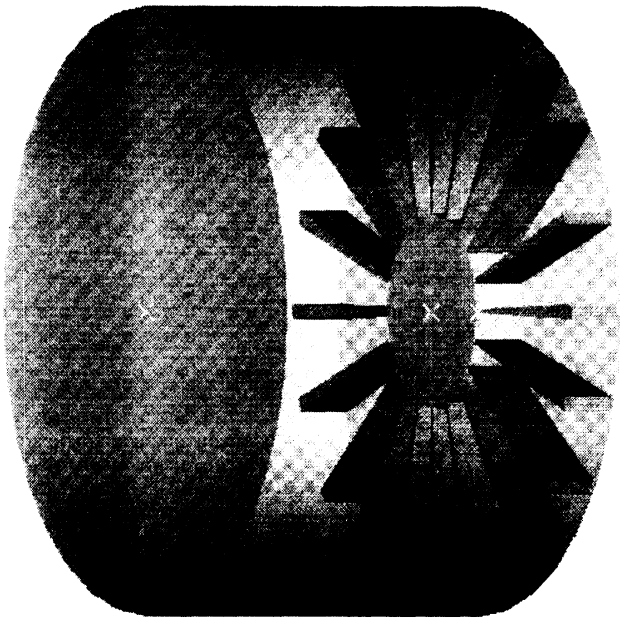

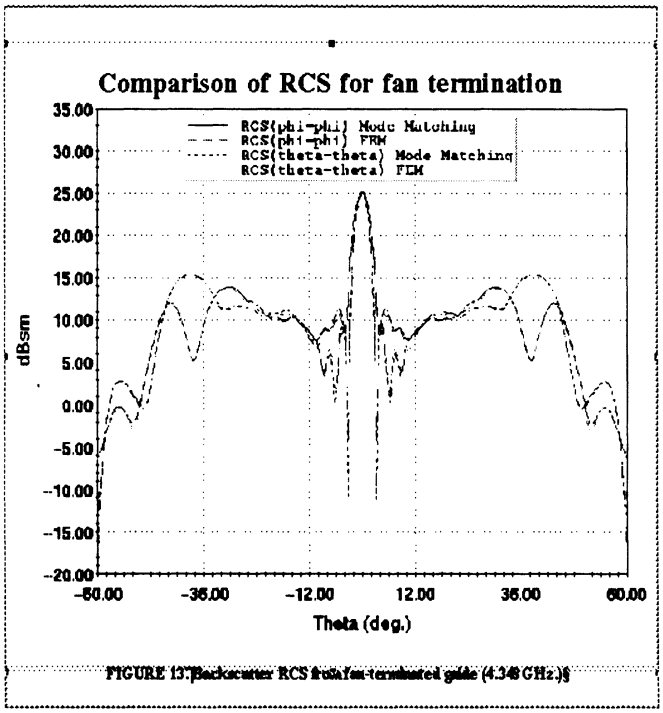

Figure 15: Scattering by a cylindrical guide terminated with a straight bladed engine configuration.

feed modeling and parallelization for large scale simulations will continue to dominate future research and developments relating to partial differential equation methods. An apparent advantage of the finite element method is its potential hybridization with all other frequency domain methods. Future applications of the finite element method are likely to make greater use of hybridization techniques aimed at increasing the method's accuracy and efficiency while retaining its inherent geometrical adaptability and ease in handling materials.

References

[1] J. L. Volakis, A. Chatterjee, and L. C. Kempel, 'A review of the finite element method for three dimensional scattering', *J. Opt. Soc. of America*, A, pp. 1422-1433, 1994.

[2] T. B. A. Senior and J. L. Volakis, *Approximate Boundary Conditions in Electromagnetics*, London, IEE Press, 1995.

[3] O. C. Zienkiewicz, *The finite element method*, McGraw Hill, New York, 3rd edition, 1979.

[4] A. Chatterjee, J. M. Jin and J. L. Volakis, 'A finite element formulation with absorbing boundary conditions for three dimensional scattering', *IEEE Trans. Antennas Propagat.*, vol. 41, pp. 221-226, 1993.

[5] J. P. Webb, "Edge elements and what they can do for you," *IEEE Trans. Mag.*, vol. 29, pp. 1460-5, 1993.

[6] D. Sun, J.Manges, X. Yuan, and Z. Cendes, "Spurious modes in Finite–element mothods," *IEEE Antennas Propagat. Magaz.*, Vol.37, No.5, pp.12-24, Oct. 1995

[7] H. Whitney, *Geometric Integration Theory*, Princeton University Press, 1957.

[8] J. C. Nedelec, "Mixed finite elements in R^3", *Numer. Math.*, vol. 35, pp. 315-41, 1980.

[9] A. Bossavit and J. C. Verite, "A mixed FEM-BIEM method to solve 3D eddy current problems," *IEEE Trans. Mag.*, vol. 18, pp. 431-5, March 1982.

[10] A. Bossavit, "Whitney forms: a class of finite elements for three-dimensional computations in electromagnetism," *IEE Proc.*, vol. 135, pt. A, no. 8, Nov. 1988.

[11] M. L. Barton and Z. J. Cendes, "New vector finite elements for three-dimensional magnetic field computation," *J. Appl. Phys.*, vol. 61, no. 8, pp. 3919-21, Apr 1987.

[12] J. S. van Welij, "Calculation of eddy currents in terms of H on hexahedra," *IEEE Trans. Mag.*, vol. 21, pp. 2239-41, Nov. 1985.

[13] J. F. Lee, D. K. Sun, and Z. J. Cendes, "Full-wave analysis of dielectric waveguides using tangential vector finite elements," *IEEE Trans. Microwave Theory Tech.*, vol. 39, no. 8, pp. 1262-71, Aug 1991.

[14] J. M. Jin and J. L. Volakis, "Electromagnetic scattering by and transmission through a three-dimensional slot in a thick conducting plane," *IEEE Trans. Antennas Propagat.*, vol. 39, pp. 543-550, Apr 1991.

[15] R. D. Graglia, A. F. Peterson and D. R. Wilton, "Higher order conforming vector bases on curvilinear elements," This issue.

[16] J. F. Lee, D. K. Sun, and Z. J. Cendes, "Tangential vector finite elements for electromagnetic field computation," *IEEE Trans. Mag.*, vol. 27, no. 5, pp. 4032-5, Sep. 1991.

[17] G. Mur and A. T. deHoop, "A finite element method for computing three-dimensional electromagnetic fields in inhomogeneous media," *IEEE Trans. Mag.*, vol. 21, pp. 2188-91, Nov. 1985.

[18] J. S. Wang and N. Ida, "Curvilinear and higher order *edge* finite elements in electromagnetic field computation," *IEEE Trans. Mag.*, vol. 29, no. 2, pp. 1491-4, March 1993.

[19] J. P. Webb and B. Forghani, "Hierarchal scalar and vector tetrahedra," *IEEE Trans. Mag.*, vol. 29, no. 2, pp. 1495-8, March 1993.

[20] Z. S. Sacks, D. M. Kingsland, R. Lee, and J. F. Lee, "A perfectly matched anisotropic absorber for use as an absorbing boundary condition," *IEEE Trans. Antennas Propagat.*, vol. 43, no. 12, Dec. 1995.

[21] P. Silvester and M.S. Hsieh, "Finite element solution of 2-dimensional exterior field problems", *Proc. IEE*, vol. 118, pp. 1743-1747, Dec. 1971.

[22] B.H. McDonald and A. Wexler, "Finite element solution of unbounded field problems," *IEEE Trans. Microwave Theory Tech.*, vol. 20, pp. 841-847, Dec. 1972.

[23] J. M. Jin and J. L. Volakis, "TM scattering by an inhomogeneously filled aperture in a thick ground plane", *IEE Proc., Part H*, vol. 137, no. 3, pp. 153-159, June 1990.

[24] X. Yuan and D.R. Lynch and J.W. Strohbehn, "Coupling of finite element and moment methods for electromagnetic scattering from inhomogeneous objects," *IEEE Trans. Anetnnas Propagat.*, vol. 38, pp. 386-393, March 1990.

[25] X. Yuan, "Three dimensional electromagnetic scattering from inhomogeneous objects by the hybrid moment and finite element method," *IEEE Trans. Antennas Propagat.*, vol. 38, pp. 1053-1058, 1990.

[26] J. Angelini and C. Soize and P. Soudais, "Hybrid numerical method for harmonic 3D Maxwell equations: Scattering by a mixed conducting and inhomogeneous anisotropic dielectric medium," *IEEE Trans. Antennas Propagat.*, vol. 41, no. 1, pp. 66-76, January 1993.

[27] G.E Antilla and N.G. Alexopoulos, "Scattering from complex three-dimensional geometries by a curvilinear hybrid finite element-integral equation approach," *J. Opt. Soc. Am. A*, vol. 11, no. 4, pp. 1445-1457, April 1994.

[28] P. Soudais, "Computation of the electromagnetic scattering from complex 3D objects by a hybrid FEM/BEM method," *J. Elect. Waves Appl.*, vol. 9, no. 7-8, pp. 871-886, 1995.

[29] K. D. Paulsen, X. Jia and J. Sullivan, "Finite element computations of specific absorption rates in anotomically conforming full-body models for hyperthermia treatment analysis," IEEE Trans. Biomedical Engr., vol.40, no.9, pp. 933-45, Sept. 1993.

[30] T. Eibert and V. Hansen, "Calculation of unbounded field problems in free-space by a 3D FEM/BEM-hybrid approach,"*J. Elect. Waves Appl.*, vol 10, no. 1, pp.61-78, 1996.

[31] S. M. Rao, D. R. Wilton and A. W. Glisson, "Electromagnetic scattering by surfaces of arbitrary shape," *IEEE Trans. Antennas Propagat.* vol. 30, no. 3, pp. 409-418, May 1982.

[32] T. Cwik, "Coupling finite element and integral equation solutions using decoupled boundary meshes (electromagnetic scattering), *IEEE Trans. Antennas Propagat.*, vol. 40, no. 12, pp. 1496-1504, Dec. 1992.

[33] J.M. Jin and J.L. Volakis and J.D. Collins, "A finite element-boundary integral method for scattering and radiation by two- and three-dimensional structures," *IEEE Antennas and Propagat. Society magazine*, vol. 33, no. 3, pp. 22-32, June 1991.

[34] E. Arvas, A. Rahhal-Arabi, A. Sadigh and S. M. Rao, "Scattering from multiple conducting and dielectric bodies of arbitrary shape," *IEEE Trans. Antennas Propagat. Soc. Mag.*, vol. 33, no. 2, pp. 29-36, April 1991.

[35] J.D. Collins and J.M. Jin and J.L. Volakis, "Eliminating interior resonances in FE-BI methods for scattering," *IEEE Trans. Antennas Propagat.*, vol. 40, pp. 1583-1585", December 1992.

[36] J.M. Jin and J.L. Volakis, "A hybrid finite element method for scattering and radiation by microstrip patch antennas and arrays residing in a cavity," *IEEE Trans. Antennas Propagat.*, vol. 39, pp. 1598-1604, 1991.

[37] J.L. Volakis and J. Gong and A. Alexanian, "A finite element boundary integral method for antenna RCS analysis," *Electromagnetics*, vol. 14, no. 1, pp. 63-85, 1994.

[38] J.M. Jin and J.L. Volakis, "Scattering and radiation analysis of three-dimensional cavity arrays via a hybrid finite element method," *IEEE Trans. Antennas Propagat.*, vol. 41, pp. 1580-1586, Nov 1993.

[39] J. Gong, J. L. Volakis, A. Woo, and H. Wang, "A hybrid finite element boundary integral method for analysis of cavity-backed antennas of arbitrary shape", *IEEE Trans. Antennas Propagat.*, vol. 42, pp. 1233-1242, 1994.

[40] L. C. Kempel, J. L. Volakis and R. Sliva, "Radiation by cavity-backed antennas on a circular cylinder," *IEE Proceedings, Part H.* pp. 233-239, 1995.

[41] Y. Zhuang, K-L. Wu, C. Wu and J. Litva, "Acombined full-wave CG-FFT method for rigorous analysis of large microstrip antenna arrays," *IEEE Trans. Antennas Propagat.*, vol. 44, pp. 102-109, January 1996.

[42] J.D. Collins and J.M. Jin and J.L. Volakis, "A combined finite element-boundary element formulation for solution of two-dimensional problems via CGFFT," *Electromagnetics*, vol. 10, pp. 423–437, 1990.

[43] K. Barkeshli and J.L. Volakis, "On the implementation and accuracy of the conjugate gradient FFT method," *IEEE Trans. Antennas Propagat.*, vol. 32, pp. 20-26, 1990.

[44] J.M. Jin and J.L. Volakis, "Biconjugate gradient FFT solution for scattering by planar plates," *Electromagnetics*, vol. 12, pp. 105-119, 1992.

[45] J. L. Volakis, "Iterative Solvers," *IEEE Antenna Propagat. Soc. Mag.*, vol. 37, no. 6, pp. 94-96, December 1995.

[46] T. Özdemir and J. L. Volakis, "A comparative study of an absorbing boundary condition and an artificial absorber for terminating finite element meshes', *Radio Sci.*, vol 29, no. 5, pp. 1255-1263, Sept.-Oct. 1994

[47] C. Farhat and F-X. Roux, "An unconventional domain decomposition method for an efficient parallel solution of large-scale finite element systems," *SIAM J. Sci. Stat. Comput.*, vol. 13, pp. 379-396, January 1992.

[48] V. Rokhlin, "Rapid solution of integral equations of scattering theory in two dimensions," *Journal of Computational Physics*, vol. 86, no. 2, pp. 414-439, 1990.

[49] W. C. Chew, C. C. Lu, E. Michielssen and J. M. Song, "Fast solution methods in electromagnetics," This issue.

[50] R. Coifman, V. Rokhlin and S. Wandzura, "The fast multipole method for the wave equation: A pedestrian prescription," *IEEE Antennas and Propagat. Magazine*, June 1993.

[51] C.C. Lu and W.C. Chew, "Fast far field approximation for calculating the RCS of large objects," *Micro. Opt. Tech. Lett.*, vol.8, no.5, pp.238-241, April 1995.

[52] S. Bindiganavale and J. L. Volakis, "A hybrid FEM-FMM technique for electromagnetic scattering," *Proceedings of the 12th annual review of progress in applied computational electromagnetics (ACES)*, Naval Postgraduate School, Monterey CA, pp 563-570, March 1996.

[53] S.S. Bindiganavale and J.L. Volakis, "Guidelines for using the fast multipole method to calculate the RCS of large objects," *Micro. Opt. Tech. Lett.*, vol.11, no.4, March 1996.

[54] E. Bleszynski, M. Bleszynski and T. Jaroszerwicz, "A fast integral equation solver for Electromagnetic scattering problems," *IEEE Antennas Propagat. Symposium Processdings*, Seattle, WA, pp. 417–420, 1994

[55] A. Bayliss and E. Turkel, 'Radiation boundary conditions for wave-like equations', *Comm. Pure Appl. Math.*, vol. 33, pp. 707-725, 1980.

[56] B. Engquist and A. Majda, 'Absorbing boundary conditions for the numerical simulation of waves', *Math. Comp.*, vol. 31, pp. 629-651, 1977.

[57] J.P. Webb and V.N. Kanellopoulos, "Absorbing boundary conditions for finite element solution of the vector wave equation," *Microwave and Opt. Techn. Letters*, vol. 2, no. 10, pp. 370-372, October 1989.

[58] V. N. Kanellopoulos and J. P. Webb, "The importance of the surface divergence term in the finite element-vector absorbing boundary condition method," *IEEE Trans. Microw. Theory Tech.*, vol. 43, no. 9, pp. 2168-2170, Sept. 1995.

[59] A. Chatterjee and J. L. Volakis, "Conformal absorbing boundary conditions for 3D problems: Derivation and applications', *IEEE Trans. Antennas Propagat.*, vol. 43, no. 8, pp. 860-866, August 1995.

[60] L. C. Kempel and J. L. Volakis, "Scattering by cavity-backed antennas on circular cylinder," *IEEE Trans. Antennas Propagat.*, vol. 42, pp. 1268-1279, 1994.

[61] T. B. A. Senior, J. L. Volakis and S. R. Legault, "Higher order impedance boundary conditions," *IEEE Trans. Antennas Propagat.*, to appear.

[62] S. R. Legault, T. B. A. Senior and J. L. Volakis, "Design of planar absorbing layers for domain truncation in FEM applications," *Electromagnetics*, to appear.

[63] J. Gong and J. L. Volakis, "Optimal selection of uniaxial artificial absorber layer for truncating finite element meshes," *Electronics Letters*, vol. 31, no. 18, pp. 1559-1561, August 1995.

[64] J. Gong and J. L. Volakis, "An efficient and accurate model of the coax cable feeding structure for FEM simulations," *IEEE Trans. Antennas Propagat.*, vol. 43, no. 12, pp. 1474-1478, December 1995.

[65] D. R. Kincaid and T. K. Oppe, "ITPACK on supercomputers," *Int. J. on Num. Methods, Lecture Notes in Math.*, vol. 1005, pp. 151-161, 1982.

[66] E. Anderson and Y. Saad, "Solving sparse triangular linear systems on parallel computers," *Int. J. of High Speed Computing*, vol. 1, pp. 73-95, 1989.

[67] A. Chatterjee, J. L. Volakis and D. Windheiser, "Parallel computation of 3D electromagnetic scattering using finite elements," *Int. J. Num. Modeling.: Electr. Net. Dev. and Fields*, vol. 7, pp. 329-342, 1994.

[68] J.M. Putnam and L.N. Medgyesi-Mitschang, "Combined field integral equation formulation for axially inhomogeneous bodies of revolution," McDonnell Douglas Research Labs, MDC QA003, December 1987

[69] E.L. Pelton and B.A. Munk, "Scattering from periodic arrays of crossed dipoles," *IEEE Trans. Antennas Propagat.*, vol. AP-27, pp. 323–330.

[70] H. Wang, Personal communication, China Lake, CA, 1995

[71] D. C. Ross, J.L. Volakis and H. T. Anastassiu, A Hybrid finite element-modal analysis of jet engine scattering, *IEEE Trans. Antenna Propagat.*, AP-43, pp. 277-285, Feb. 1995

[72] J. Karty, J. Roedder and S. Alspach, CAVERN: A prediction code f or cavity electromagnetic analysis, *IEEE Ant. Propagat. Soc. Magaz.*, Vol. 37, No.3, pp. 68-72, June 1995.

[73] N.E. Boyse and A.A Seidl, "A hyrid finite element method for 3D scattering using nodal and edge elements," *IEEE Trans. Antennas Propagat.*, vol. 42, pp. 1436–1442, Oct. 1994

[74] T. Cwik,"Parallel decomposition methods for the solution of electromagnetic scattering problems," *Electromagnetics,* Vol. 42 pp. 343–357, 1992

[75] P. Le Tallec, E. Sallel and M. Vidrascu, "Solving large scale structural problems on parallel computers using domain decomposition techniques," Chapter in *Advances in Parallel and Vector Processing for Structural Mechanics*, (edited by B. Topping and M. Papadrakakis), CIVIL–COMP Ltd. Edinburgh, Scotland, 1994

[76] N. Golias, A. Papagiannakis and T. Tsiboukis, "Efficient mode analysis with edge elements and 3D adaptive refinement," *IEEE Trans. MTT,* Vol. 42 pp. 99–107, Jan. 1994